Cronfa - Swansea University Open Access Repository

_____

This is an author produced version of a paper published in:
Computer Methods in Applied Mechanics and Engineering

_____

Paper:

http://www.swansea.ac.uk/library/researchsupport/ris-support/

A mixed variational framework for the design of energy-momentum integration schemes based on convex multi-variable electro-elastodynamics

M. Franke[1], R. Ortigosa[2], A. Janz, A. J. Gil[3], P. Betsch

Abstract

In [34], the authors presented a new family of time integrators for large deformation electromechanics. In that paper, definition of appropriate algorithmic expressions for the discrete derivatives of the internal energy and consideration of multi-variable convexity of the internal energy was made. These two ingredients were essential for the definition of a new energy-momentum (EM) time integrator in the context of large deformation electromechanics relying on materially stable (ellipticity compliant) constitutive models. In [8], the authors introduced a family of EM time integrators making use of mixed variational principles for large strain mechanics. In addition to the displacement field, the right Cauchy-Green deformation tensor, its co-factor and its Jacobian were introduced as unknown fields in the formulation. An elegant cascade system of kinematic constraints was introduced in this paper, crucial for the satisfaction of the required conservation properties of the new family of EM time integrators. The objective of the present paper is the introduction of new mixed variational principles for EM time integrators in electromechanics, hence bridging the gap between the previous work presented by the authors in References [34] and [8], opening up the possibility to a variety of new Finite Element implementations. The following characteristics of the proposed EM time integrator make it very appealing: (i) the new family of time integrators can be shown to be thermodynamically consistent and second order accurate; (ii) piecewise discontinuous interpolation of the unknown fields (except displacements and electric potential) has been carried out, in order to yield a computational cost comparable to that of standard displacement-potential formulations. Finally, a series of numerical examples are included in order to demonstrate the robustness and conservation properties of the proposed scheme, specifically in the case of long-term simulations.

Keywords: Mixed variational framework, electroactive polymer, electro-elastodynamics, multi-variable convexity, energy-momentum scheme.

1. Introduction

Dielectric elastomers, [27, 39–41] represent an important family of Electro Active Polymers (EAPs) which are well-known for their outstanding actuation capabilities and low stiffness properties, which makes them ideal for their use as *soft robots* [28, 33]. Other important applications for dielectric elastomers include braille displays, deformable lenses, haptic devices and energy generators, to name but a few [12].

The finite element simulation of these materials [15, 26, 50–53] relies on the definition of a suitable constitutive model. It is customary to propose an invariant-based representation of the Helmholtz energy functional (depending upon the deformation and the electric field). Other

---

[1]Corresponding author: marlon.franke@kit.edu
[2]Corresponding author: r.ortigosa@swansea.ac.uk
[3]Corresponding author: a.j.gil@swansea.ac.uk

authors prefer to propose a constitutive model based on the invariant representation of the internal energy (depending upon the deformation and the electric displacement field). Motivated by the possible loss of ellipticity [5, 30, 46, 47] of the Helmholtz functional, Gil and Ortigosa [19, 35, 36] advocated for the use of the internal energy functional for the definition of constitutive models in nonlinear electro-mechanics. In essence, the authors postulated a definition of the internal energy convex with respect to an extended set of arguments, namely the deformation gradient tensor $\boldsymbol{F}$, its co-factor $\boldsymbol{H}$, its Jacobian J, the Lagrangian electric displacement field $\boldsymbol{D}_0$ and $\boldsymbol{d}$, defined as $\boldsymbol{d} = \boldsymbol{F}\boldsymbol{D}_0$ and proved that this definition satisfies the ellipticity condition unconditionally. In the absence of electric effects, where the two last arguments vanish, the proposed definition coincides with the well established concept of polyconvexity [2, 3].

Very recently, the authors in [34] proposed a new energy-momentum (EM in the sequel) preserving time integrator [6, 20, 48] for reversible electro-elastodynamics building upon the works [18, 22, 24, 25]. As shown in [34], the new EM time integrator proved to be very robust and accurate for the long-term simulation of EAPs. The consistent implicit EM time integration scheme developed inherits the conservation laws of total energy, linear momentum, angular momentum and electric charge.

In the purely mechanical case [22, 24], the thermodynamical consistency of these methods is ensured by virtue of replacing the (exact) derivative of the strain energy with respect to the right Cauchy-Green deformation tensor (i.e. the consistent second Piola-Kirchhoff stress tensor) with its algorithmic counterpart. The latter, denoted as discrete derivative [7, 18, 20, 43] must be defined in compliance with the so-called *directionality property*. Specially relevant for the work carried out in this manuscript is the recent work by Betsch et al. [8], where a new consistent EM time integration scheme has been developed in the context of polyconvex elasticity. Essentially, these authors proposed the consideration of three discrete derivatives of the strain energy. Each discrete derivative represents the algorithmic counterpart of the work conjugates of the right Cauchy-Green deformation tensor, its co-factor and its determinant. In comparison to previously proposed discrete derivative expressions (see e.g. [20, 23]), the new stress formula in [8, 18] assumes a remarkably simple form. A key factor for that simplification is the use of a tensor cross product pioneered by the Boer [13] and employed for the first time by Bonet et al. [9, 10] in the case of nonlinear electromechanics [19, 35–37].

Building upon the work presented in References [34] and [8], the objective of this paper is to develop a new EM time integrator in the context of electro-elastodynamics based on a mixed variational formulation where the right Cauchy-Green deformation tensor, its co-factor and its determinant are parts of the unknown fields. The resulting new formulation opens up several possibilities in terms of its spatial discretisation and subsequent computational finite element implementation.

The outline of this paper is as follows: in Section 2, some basic principles of kinematics are presented. The governing equations in nonlinear electro-elastodynamics are also presented in this section. The concept of multi-variable convexity and its importance from the material stability point of view is presented in Section 3. Section 4 starts with the three-field mixed formulation presented in [19] in the context of static electromechanics. Its extension to electro-elastodynamics is then carried out by defining the appropriate action integral. After derivation of the stationary conditions of the action integral, Section 5 introduces a new one-step implicit EM time integration scheme for electro-elastodynamics. Section 6 briefly describes the finite element implementation of the new time integration scheme and Section 7 presents eight numerical examples in order to validate the conservation properties and robustness of the new scheme. Finally, Section 8 provides some concluding remarks. For completeness, Appendix A outlines the definitions of the discrete derivatives featuring in the proposed time integrator in Section 5.

2. Nonlinear continuum electromechanics

A brief introduction into nonlinear continuum electromechanics and the relevant governing equations will be presented in this section.

2.1. Kinematics: motion and deformation

Let us consider the motion of an EAP with reference configuration $\mathcal{B}_0 \in \mathbb{R}^3$ and its boundary $\partial\mathcal{B}_0$ with unit outward normal $\boldsymbol{N}$ (refer to Fig. 1). During its motion, the EAP occupies a deformed configuration $\mathcal{B} \in \mathbb{R}^3$ with boundary $\partial\mathcal{B}$ and unit outward normal $\boldsymbol{n}$. The motion of the EAP is defined by the mapping $\boldsymbol{\phi}(\boldsymbol{X}, t)$, which links a material particle from the reference configuration $\boldsymbol{X} \in \mathcal{B}_0$ to the deformed configuration $\boldsymbol{x} \in \mathcal{B}$ according to $\boldsymbol{x} = \boldsymbol{\phi}(\boldsymbol{X}, t)$. Associated with $\boldsymbol{\phi}(\boldsymbol{X}, t)$ it is possible to define the deformation gradient tensor $\boldsymbol{F}_\phi$ [4, 11, 14, 21] as

$$\boldsymbol{F}_\phi = \boldsymbol{\nabla}_0 \boldsymbol{\phi}(\boldsymbol{X}, t); \qquad F_{\phi iI} = \frac{\partial \phi_i}{\partial X_I}. \tag{1}$$

The deformation gradient tensor $\boldsymbol{F}_\phi{}^4$ relates a fibre of differential length from the material configuration $d\boldsymbol{X}$ to the deformed configuration $d\boldsymbol{x} = \boldsymbol{F}_\phi d\boldsymbol{X}$. In addition, differential area vector and volume elements in the reference configuration, $d\boldsymbol{A}$ (colinear with $\boldsymbol{N}$) and dV respectively, are mapped to the deformed configuration $d\boldsymbol{a}$ (colinear with $\boldsymbol{n}$) and dv, respectively, by means of the co-factor or adjoint tensor $\boldsymbol{H}_\phi$ as $d\boldsymbol{a} = \boldsymbol{H}_\phi d\boldsymbol{A}$ and the Jacobian J_ϕ as $dv = J_\phi dV$, respectively. Both $\boldsymbol{H}_\phi$ and J_ϕ can be related to $\boldsymbol{F}_\phi$ as

$$\boldsymbol{H}_\phi = (\det \boldsymbol{F}_\phi) \, \boldsymbol{F}_\phi^{-T}; \qquad J_\phi = \det \boldsymbol{F}_\phi. \tag{2}$$
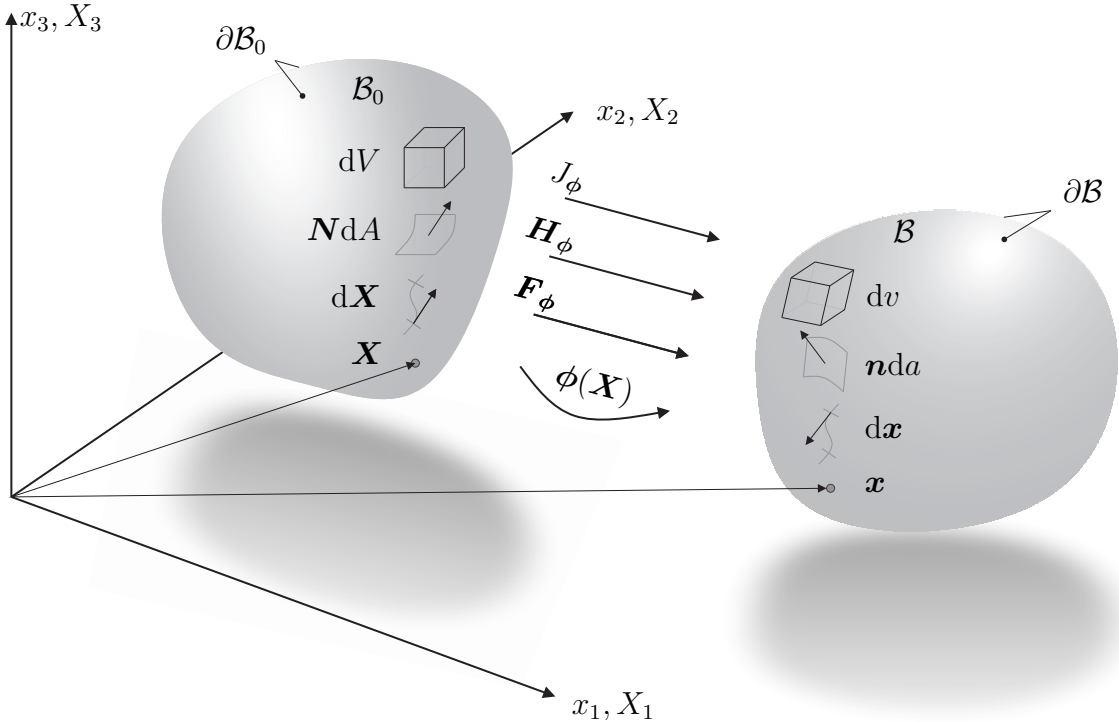
Figure 1: Deformation mapping $\boldsymbol{\phi}(\boldsymbol{X}, t)$ and kinematic variables $\{\boldsymbol{F}_\phi, \boldsymbol{H}_\phi, J_\phi\}$.

---

[4]Subscript ϕ is included throughout the paper in order to emphasise the geometrically exact deformation term.

Equivalent expressions to those in (2) can be obtained by making use of the tensor cross product operation introduced by de Boer [13] and defined as

$$\boldsymbol{H}_\phi = \frac{1}{2}\boldsymbol{F}_\phi \times \boldsymbol{F}_\phi; \qquad\qquad H_{\phi iI} = \frac{1}{2}\mathcal{E}_{ijk}\mathcal{E}_{IJK}F_{\phi jJ}F_{\phi kK}; \qquad\qquad (3a)$$

$$J_\phi = \frac{1}{3}\boldsymbol{H}_\phi : \boldsymbol{F}_\phi; \qquad\qquad J_\phi = \frac{1}{3}H_{\phi iI}F_{\phi iI}, \qquad\qquad (3b)$$

where $\mathcal{E}_{ijk}$ (or $\mathcal{E}_{IJK}$) symbolises the third order alternating tensor components[5] and the use of repeated indices implies summation, unless otherwise stated.

2.2. Governing equations in nonlinear electromechanics: conservation of linear momentum and angular momentum

The local form of the balance of linear momentum [21] can be written as

$$\begin{aligned}
\rho_0\dot{\boldsymbol{v}} - \mathrm{DIV}\,(\boldsymbol{F}_\phi\boldsymbol{S}) - \boldsymbol{f}_0 &= \boldsymbol{0}; & \text{in } \mathcal{B}_0; \\
(\boldsymbol{F}_\phi\boldsymbol{S})\,\boldsymbol{N} &= \boldsymbol{t}_0; & \text{on } \partial_{\boldsymbol{t}}\mathcal{B}_0; \\
\boldsymbol{\phi} &= \bar{\boldsymbol{\phi}}; & \text{on } \partial_{\boldsymbol{\phi}}\mathcal{B}_0; \\
\boldsymbol{\phi}(t=0) &= \boldsymbol{\phi}_0; & \text{in } \mathcal{B}_0; \\
\boldsymbol{v}(t=0) &= \boldsymbol{v}_0; & \text{in } \mathcal{B}_0,
\end{aligned} \qquad (4)$$

where $\rho_0 : \mathcal{B}_0 \to \mathbb{R}^+$ represents the mass density of the EAP in the reference configuration, $\boldsymbol{v}$ the velocity field and $(\dot{\bullet})$ denotes differentiation with respect to time. $\boldsymbol{f}_0$ represents a body force per unit undeformed volume $\mathcal{B}_0$ and $\boldsymbol{t}_0$, the traction force per unit undeformed area applied on $\partial_{\boldsymbol{t}}\mathcal{B}_0 \subset \partial\mathcal{B}_0$, where $\partial_{\boldsymbol{t}}\mathcal{B}_0 \cup \partial_{\boldsymbol{\phi}}\mathcal{B}_0 = \partial\mathcal{B}_0$ and $\partial_{\boldsymbol{t}}\mathcal{B}_0 \cap \partial_{\boldsymbol{\phi}}\mathcal{B}_0 = \emptyset$. Furthermore, $\boldsymbol{\phi}_0$ and $\boldsymbol{v}_0$ denote the initial configuration and velocity, respectively. Finally, $\boldsymbol{S}$ represents the second Piola-Kirchhoff stress tensor and the local balance of angular momentum leads to the well-known tensor condition $\boldsymbol{S} = \boldsymbol{S}^T$. Note that $\boldsymbol{S}$ depends on the displacement and the electrical field and is comprised of unsymmetrical mechanical and an electrical contributions.

2.3. Governing equations in non-linear electromechanics: Gauss's and Faraday's laws

In the absence of magnetic and time dependent effects, Maxwell equations reduce to Gauss's and Faraday's laws. The local form of the Gauss law [31, 32, 49] can be written in a Lagrangian setting as

$$\begin{aligned}
\mathrm{DIV}\boldsymbol{D}_0 - \rho_0^e &= 0; & \text{in } \mathcal{B}_0; \\
\boldsymbol{D}_0 \cdot \boldsymbol{N} &= -\omega_0^e; & \text{on } \partial_\omega\mathcal{B}_0,
\end{aligned} \qquad (5)$$

where $\boldsymbol{D}_0$ is the Lagrangian electric displacement vector, ρ_0^e represents an electric volume charge per unit of undeformed volume $\mathcal{B}_0$ and ω_0^e, an electric surface charge per unit of undeformed area $\partial_\omega\mathcal{B}_0 \subset \partial\mathcal{B}_0$. Alternatively, the spatial electric displacement vector $\boldsymbol{D}$ can be obtained through the area push forward relationship $\boldsymbol{D}_0 = \boldsymbol{H}_\phi^T\boldsymbol{D}$, [15, 16]. The local form of the static Faraday's law can be written in a Lagrangian setting as

$$\begin{aligned}
\boldsymbol{E}_0 &= -\boldsymbol{\nabla}_0\varphi; & \text{in } \mathcal{B}_0; \\
\varphi &= \bar{\varphi}; & \text{on } \partial_\varphi\mathcal{B}_0,
\end{aligned} \qquad (6)$$

where $\boldsymbol{E}_0$ is the Lagrangian electric field vector and φ, the scalar electric potential. In (6), $\partial_\varphi\mathcal{B}_0$ represents the part of the boundary $\partial\mathcal{B}_0$ where essential electric potential boundary conditions are applied, where $\partial_\omega\mathcal{B}_0 \cup \partial_\varphi\mathcal{B}_0 = \partial\mathcal{B}_0$ and $\partial_\omega\mathcal{B}_0 \cap \partial_\varphi\mathcal{B}_0 = \emptyset$. The spatial electric field vector $\boldsymbol{E}$ can be obtained through the standard fibre transformation $\boldsymbol{E}_0 = \boldsymbol{F}_\phi^T\boldsymbol{E}$ [15, 16].

---

[5]Lower case indices $\{i, j, k\}$ will be used to represent the spatial configuration whereas capital case indices $\{I, J, K\}$ will be used to represent the material description.

3. Constitutive equations in nonlinear electro-elasticity

The governing equations presented in Section 2 are coupled by means of a suitable constitutive law. The objective of the following section is to introduce some notions on constitutive laws in nonlinear electro-elasticity.

3.1. Multi-variable convexity

In the case of reversible electro-elasticity, the internal energy density e per unit of undeformed volume can be defined in terms of the deformation and the electric displacement field, namely $e = e(\boldsymbol{\nabla}_0\boldsymbol{\phi}, \boldsymbol{D}_0)$ [32]. Motivated solely by considerations of material stability, Gil and Ortigosa [19, 35, 36, 38] extended the concept of polyconvexity [1–3] to the context of electromechanics and defined new convexity restrictions on the internal energy, postulating a convex multi-variable definition as

$$e\left(\boldsymbol{\nabla}_0\boldsymbol{\phi}, \boldsymbol{D}_0\right) = W\left(\boldsymbol{F}_\phi, \boldsymbol{H}_\phi, J_\phi, \boldsymbol{D}_0, \boldsymbol{d}\right); \qquad \boldsymbol{d} = \boldsymbol{F}_\phi\boldsymbol{D}_0, \tag{7}$$

where W must be a convex function with respect to the extended set $\mathcal{V} = \{\boldsymbol{F}_\phi, \boldsymbol{H}_\phi, J_\phi, \boldsymbol{D}_0, \boldsymbol{d}\}$. Crucially, the above convex multi-variable representation in (7) satisfies the concept of ellipticity for the entire range of deformations and electric displacement fields. In addition, for the requirement of objectivity, the convex multi-variable energy W (7) can be re-expressed as

$$e\left(\boldsymbol{\nabla}_0\boldsymbol{\phi}, \boldsymbol{D}_0\right) = \widetilde{e}\left(\boldsymbol{C}_\phi, \boldsymbol{D}_0\right) = \widetilde{W}_{\text{obj}}\left(\boldsymbol{C}_\phi, \boldsymbol{G}_\phi, C_\phi, \boldsymbol{D}_0, \boldsymbol{C}_\phi\boldsymbol{D}_0\right) = \widetilde{W}\left(\boldsymbol{C}_\phi, \boldsymbol{G}_\phi, C_\phi, \boldsymbol{D}_0\right), \tag{8}$$

where $\widetilde{e}$ represents the internal energy in terms of the right Cauchy-Green strain tensor $\boldsymbol{C}_\phi$ and $\boldsymbol{D}_0$. Moreover, $\widetilde{W}$ denotes the internal energy expressed in terms of the extended symmetric mechanical kinematic set $\{\boldsymbol{C}_\phi, \boldsymbol{G}_\phi, C_\phi\}$, defined as

$$\boldsymbol{C}_\phi = \boldsymbol{F}_\phi^T\boldsymbol{F}_\phi; \qquad \boldsymbol{G}_\phi = \frac{1}{2}\boldsymbol{C}_\phi \times \boldsymbol{C}_\phi = \boldsymbol{H}_\phi^T\boldsymbol{H}_\phi; \qquad C_\phi = \frac{1}{3}\boldsymbol{G}_\phi : \boldsymbol{C}_\phi = J_\phi^2, \tag{9}$$

and $\boldsymbol{D}_0$.

3.2. The Helmholtz energy function

The convex multi-variable nature of the internal energy $e\left(\boldsymbol{\nabla}_0\boldsymbol{\phi}, \boldsymbol{D}_0\right)$ ensures convexity of $e\left(\boldsymbol{\nabla}_0\boldsymbol{\phi}, \boldsymbol{D}_0\right)$, $\widetilde{e}\left(\boldsymbol{C}_\phi, \boldsymbol{D}_0\right)$ and $\widetilde{W}\left(\boldsymbol{C}_\phi, \boldsymbol{G}_\phi, C_\phi, \boldsymbol{D}_0\right)$ with respect to $\boldsymbol{D}_0$. Consequently, a one-to-one and invertible relationship between variables $\boldsymbol{D}_0$ and $\boldsymbol{E}_0$ can always be established. Therefore, it is possible to make use of a partial Legendre transform of the internal energy which leads to the definition of the Helmholtz energy functional $\widetilde{W}_\Phi(\boldsymbol{C}_\phi, \boldsymbol{G}_\phi, C_\phi, \boldsymbol{E}_0)$ (refer to [19]) as

$$\widetilde{W}_\Phi(\boldsymbol{C}_\phi, \boldsymbol{G}_\phi, C_\phi, \boldsymbol{E}_0) = -\sup_{\boldsymbol{D}_0}\left\{\boldsymbol{E}_0 \cdot \boldsymbol{D}_0 - \widetilde{W}\left(\boldsymbol{C}_\phi, \boldsymbol{G}_\phi, C_\phi, \boldsymbol{D}_0\right)\right\}. \tag{10}$$

4. Electro-Elastodynamics

The objective of this section is to present the variational formulation that will be used in order to develop an EM time integration scheme in Section 5.

4.1. Extension to electro-elastodynamics

A point of departure is the following action integral [34]

$$\begin{aligned}
L_{\widetilde{W}}\left(\boldsymbol{v}, \boldsymbol{\phi}, \varphi, \boldsymbol{D}_0\right) = \int_{t_0}^t &\left(\int_{\mathcal{B}_0}\left(\dot{\boldsymbol{\phi}} - \frac{1}{2}\boldsymbol{v}\right) \cdot \rho_0\boldsymbol{v}\, dV - \int_{\mathcal{B}_0}\widetilde{W}\left(\boldsymbol{C}_\phi, \boldsymbol{G}_\phi, C_\phi, \boldsymbol{D}_0\right)\, dV \right. \\
&\left. - \int_{\mathcal{B}_0}\boldsymbol{D}_0 \cdot \boldsymbol{\nabla}_0\varphi\, dV + \Pi_{\text{ext}}^m\left(\boldsymbol{\phi}\right) + \Pi_{\text{ext}}^e\left(\varphi\right)\right)\, dt,
\end{aligned} \tag{11}$$

5

where t_0 and t represent any two instances of time with $t > t_0$. Furthermore, in (11) the external contributions Π_{ext}^m and Π_{ext}^e are defined as

$$\Pi_{\text{ext}}^m (\boldsymbol{\phi}) = \int_{\mathcal{B}_0} \boldsymbol{f}_0 \cdot \boldsymbol{\phi} \, dV + \int_{\partial_t \mathcal{B}_0} \boldsymbol{t}_0 \cdot \boldsymbol{\phi} \, dA; \qquad \Pi_{\text{ext}}^e (\varphi) = - \int_{\mathcal{B}_0} \rho_0^e \varphi \, dV - \int_{\partial_\omega \mathcal{B}_0} \omega_0^e \varphi \, dA. \quad (12)$$

The objective of this section is to extend the above action integral $L_{\widetilde{W}}$ in (11), with the purpose of deriving a new mixed formulation where strain measures and stress fields are also part of the unknown fields of the problems. Starting with the four field action integral $L_{\widetilde{W}}$ in (11), originally introduced in [34], the following ten field action integral $\hat{L}_{\widetilde{W}}$ is proposed,

$$\hat{L}_{\widetilde{W}} (\boldsymbol{v}, \boldsymbol{\phi}, \varphi, \boldsymbol{D}_0, \boldsymbol{\mathcal{D}}, \boldsymbol{\Lambda}) = \int_{t_0}^{t} \left(\int_{\mathcal{B}_0} \left(\dot{\boldsymbol{\phi}} - \frac{1}{2} \boldsymbol{v} \right) \cdot \rho_0 \boldsymbol{v} \, dV - \Pi_{\widetilde{W}} (\boldsymbol{\phi}, \varphi, \boldsymbol{D}_0, \boldsymbol{\mathcal{D}}, \boldsymbol{\Lambda}) \right) dt;$$

$$\Pi_{\widetilde{W}} (\boldsymbol{\phi}, \varphi, \boldsymbol{D}_0, \boldsymbol{\mathcal{D}}, \boldsymbol{\Lambda}) = \int_{\mathcal{B}_0} \widetilde{W} (\boldsymbol{C}, \boldsymbol{G}, C, \boldsymbol{D}_0) \, dV + \int_{\mathcal{B}_0} \boldsymbol{D}_0 \cdot \boldsymbol{\nabla}_0 \varphi \, dV$$

$$+ \int_{\mathcal{B}_0} \boldsymbol{\Lambda}_{\boldsymbol{C}} : (\boldsymbol{C}_{\boldsymbol{\phi}} - \boldsymbol{C}) \, dV + \int_{\mathcal{B}_0} \boldsymbol{\Lambda}_{\boldsymbol{G}} : \left(\frac{1}{2} \boldsymbol{C} \times \boldsymbol{C} - \boldsymbol{G} \right) dV \qquad (13)$$

$$+ \int_{\mathcal{B}_0} \Lambda_C \left(\frac{1}{3} \boldsymbol{C} : \boldsymbol{G} - C \right) dV - \Pi_{\text{ext}}^m (\boldsymbol{\phi}) - \Pi_{\text{ext}}^e (\varphi),$$

and with the sets $\boldsymbol{\mathcal{D}} = \{\boldsymbol{C}, \boldsymbol{G}, C\}$ and $\boldsymbol{\Lambda} = \{\boldsymbol{\Lambda}_{\boldsymbol{C}}, \boldsymbol{\Lambda}_{\boldsymbol{G}}, \Lambda_C\}$. It is worth emphasising that whilst the action integral $L_{\widetilde{W}}$ (11) depends on the geometrically exact measures $\{\boldsymbol{C}_{\boldsymbol{\phi}}, \boldsymbol{G}_{\boldsymbol{\phi}}, C_{\boldsymbol{\phi}}\}$, the new action integral $\hat{L}_{\widetilde{W}}$ in (13) depends on the set of independent unknown fields $\{\boldsymbol{C}, \boldsymbol{G}, C\}$ which are not in general geometrically compatible, i.e. $\boldsymbol{C} \neq \boldsymbol{C}_{\boldsymbol{\phi}}$, $\boldsymbol{G} \neq \boldsymbol{G}_{\boldsymbol{\phi}}$ and $C \neq C_{\boldsymbol{\phi}}$ in a point-wise manner. Furthermore, in (13) $\{\boldsymbol{v}, \boldsymbol{\phi}, \varphi, \boldsymbol{D}_0, \boldsymbol{\mathcal{D}}, \boldsymbol{\Lambda}\} \in \mathbb{V}^{\boldsymbol{\phi}} \times \mathbb{V}^{\boldsymbol{\phi}} \times \mathbb{V}^{\varphi} \times \mathbb{V}^{\boldsymbol{D}_0} \times \mathbb{V}^{\boldsymbol{\mathcal{D}}} \times \mathbb{V}^{\boldsymbol{\mathcal{D}}}$, with $\mathbb{V}^{\boldsymbol{\mathcal{D}}} = \mathbb{V}^{\boldsymbol{C}} \times \mathbb{V}^{\boldsymbol{G}} \times \mathbb{V}^{C}$, where

$$\mathbb{V}^{\boldsymbol{\phi}} = \left\{ \boldsymbol{\phi} : \mathcal{B}_0 \to \mathbb{R}^3; \quad \boldsymbol{\phi} \in H^1 (\mathcal{B}_0) \mid J_{\boldsymbol{\phi}} > 0, \ \boldsymbol{\phi} = \bar{\boldsymbol{\phi}} \text{ on } \partial_{\boldsymbol{\phi}} \mathcal{B}_0 \right\};$$

$$\mathbb{V}^{\varphi} = \left\{ \varphi : \mathcal{B}_0 \to \mathbb{R}; \quad \varphi \in H^1 (\mathcal{B}_0) \mid \varphi = \bar{\varphi} \text{ on } \partial_{\varphi} \mathcal{B}_0 \right\};$$

$$\mathbb{V}^{\boldsymbol{D}_0} = \left\{ \boldsymbol{D}_0 : \mathcal{B}_0 \to \mathbb{R}^3; \ (\boldsymbol{D}_0)_I \in \mathbb{L}_2 (\mathcal{B}_0) \right\}; \qquad \mathbb{V}^{\boldsymbol{C}} = \left\{ \boldsymbol{C} : \mathcal{B}_0 \to \mathbb{S}; \ C_{IJ} \in \mathbb{L}_2 (\mathcal{B}_0) \right\};$$

$$\mathbb{V}^{\boldsymbol{G}} = \left\{ \boldsymbol{G} : \mathcal{B}_0 \to \mathbb{S}; \quad G_{IJ} \in \mathbb{L}_2 (\mathcal{B}_0) \right\}; \qquad \mathbb{V}^{C} = \left\{ C : \mathcal{B}_0 \to \mathbb{R}; \ C \in \mathbb{L}_2 (\mathcal{B}_0) \right\},$$

$$(14)$$

where H^1 denotes the Sobolev functional space of square integrable functions and derivatives, $\mathbb{L}_2$, the space of square integrable functions and $\mathbb{S}$, the space of symmetric second order tensors. By means of Hamilton's principle, the stationary conditions of $\hat{L}_{\widetilde{W}}$ in (13) with respect to variations $\{\delta \boldsymbol{v}, \delta \boldsymbol{\phi}, \delta \varphi, \delta \boldsymbol{D}_0\}$ are

$$\mathcal{W}_{\boldsymbol{v}} = \int_{\mathcal{B}_0} \left(\boldsymbol{v} - \dot{\boldsymbol{\phi}} \right) \cdot \rho_0 \delta \boldsymbol{v} \, dV = 0;$$

$$\mathcal{W}_{\boldsymbol{\phi}} = \int_{\mathcal{B}_0} \rho_0 \dot{\boldsymbol{v}} \cdot \delta \boldsymbol{\phi} \, dV + \int_{\mathcal{B}_0} \boldsymbol{\Lambda}_{\boldsymbol{C}} : D\boldsymbol{C}_{\boldsymbol{\phi}} [\delta \boldsymbol{\phi}] \, dV - \int_{\mathcal{B}_0} \boldsymbol{f}_0 \cdot \delta \boldsymbol{\phi} \, dV - \int_{\partial_t \mathcal{B}_0} \boldsymbol{t}_0 \cdot \delta \boldsymbol{\phi} \, dA = 0;$$

$$\mathcal{W}_{\varphi} = \int_{\mathcal{B}_0} \boldsymbol{D}_0 \cdot \boldsymbol{\nabla}_0 \delta \varphi \, dV + \int_{\mathcal{B}_0} \rho_0^e \delta \varphi \, dV + \int_{\partial_\omega \mathcal{B}_0} \omega_0^e \delta \varphi \, dA = 0; \qquad (15)$$

$$\mathcal{W}_{\boldsymbol{D}_0} = \int_{\mathcal{B}_0} \delta \boldsymbol{D}_0 \cdot \left(\partial_{\boldsymbol{D}_0} \widetilde{W} + \boldsymbol{\nabla}_0 \varphi \right) dV = 0,$$

with the admissible variations defined as $\{\delta \boldsymbol{v}, \delta \boldsymbol{\phi}, \delta \varphi, \delta \boldsymbol{D}_0\} \in \mathbb{V}_0^{\boldsymbol{\phi}} \times \mathbb{V}_0^{\varphi} \times \mathbb{V}^{\boldsymbol{D}_0}$, being

$$\mathbb{V}_0^{\boldsymbol{\phi}} = \left\{ \boldsymbol{\phi} : \mathcal{B}_0 \to \mathbb{R}^3; \quad \boldsymbol{\phi} \in H^1 (\mathcal{B}_0) \mid \boldsymbol{\phi} = \boldsymbol{0} \text{ on } \partial_{\boldsymbol{\phi}} \mathcal{B}_0 \right\};$$

$$\mathbb{V}_0^{\varphi} = \left\{ \varphi : \mathcal{B}_0 \to \mathbb{R}^3; \quad \varphi \in H^1 (\mathcal{B}_0) \mid \varphi = 0 \text{ on } \partial_{\varphi} \mathcal{B}_0 \right\}. \qquad (16)$$

Note that integration by parts with respect to time has been used on the inertia term of $(15)_b$. Equation $(15)_a$ represents the weak form for the relationship between the velocity field $\boldsymbol{v}$ and the time derivative of the mapping $\boldsymbol{\phi}$ and equation $(15)_b$, the balance of linear momentum (4). Notice that in $(15)_b$, the Lagrange multiplier $\boldsymbol{\Lambda_C}$ coincides in a weak sense with half of the second Piola-Kirchhoff stress tensor $\boldsymbol{S}$. Eventually, equations $(15)_c$ and $(15)_d$ represent the weak forms of the Gauss (5) and Faraday (6) laws, respectively. The stationary conditions of $\hat{L}_{\widetilde{W}}$ (13) with respect to variations $\delta\boldsymbol{\mathcal{D}}$ yield,

$$\mathcal{W}_{\boldsymbol{C}} = \int_{\mathcal{B}_0} \delta\boldsymbol{C} : \left(\partial_{\boldsymbol{C}}\widetilde{W} - \boldsymbol{\Lambda_C} + \boldsymbol{\Lambda_G} \times \boldsymbol{C} + \frac{1}{3}\Lambda_C \boldsymbol{G} \right) dV = 0;$$

$$\mathcal{W}_{\boldsymbol{G}} = \int_{\mathcal{B}_0} \delta\boldsymbol{G} : \left(\partial_{\boldsymbol{G}}\widetilde{W} - \boldsymbol{\Lambda_G} + \frac{1}{3}\Lambda_C \boldsymbol{C} \right) dV = 0; \qquad (17)$$

$$\mathcal{W}_C = \int_{\mathcal{B}_0} \delta C \left(\partial_C\widetilde{W} - \Lambda_C \right) dV = 0,$$

with $\{\delta\boldsymbol{C}, \delta\boldsymbol{G}, \delta C\} \in \mathbb{V}^{\boldsymbol{C}} \times \mathbb{V}^{\boldsymbol{G}} \in \mathbb{V}^C$. Notice that equation (17) represents the weak form of the constitutive equations. Finally, the stationary conditions of $\hat{L}_{\widetilde{W}}$ (13) with respect to $\delta\boldsymbol{\Lambda}$ are

$$\mathcal{W}_{\boldsymbol{\Lambda_C}} = \int_{\mathcal{B}_0} \delta\boldsymbol{\Lambda_C} : (\boldsymbol{C}_{\boldsymbol{\phi}} - \boldsymbol{C}) \, dV = 0;$$

$$\mathcal{W}_{\boldsymbol{\Lambda_G}} = \int_{\mathcal{B}_0} \delta\boldsymbol{\Lambda_G} : \left(\frac{1}{2}\boldsymbol{C} \times \boldsymbol{C} - \boldsymbol{G} \right) dV = 0; \qquad (18)$$

$$\mathcal{W}_{\Lambda_C} = \int_{\mathcal{B}_0} \delta\Lambda_C \left(\frac{1}{3}\boldsymbol{C} : \boldsymbol{G} - C \right) dV = 0,$$

with $\{\delta\boldsymbol{\Lambda_C}, \delta\boldsymbol{\Lambda_G}, \delta\Lambda_C\} \in \mathbb{V}^{\boldsymbol{C}} \times \mathbb{V}^{\boldsymbol{G}} \in \mathbb{V}^C$. It is worth emphasising that equation (18) represents the weak form of the kinematic constraints. This particular choice of kinematic constraints, taken from the EM time integrator presented by Betsch et. al. [8] in the context of elastodynamics, is crucial for the design of the EM time integration scheme in Section 5.

Remark 1. As shown in [8], differentiation with respect to time of the kinematic constraints in (18) yields the consistency conditions in the continuous setting

$$\dot{\mathcal{W}}_{\boldsymbol{\Lambda_C}} = \frac{d}{dt}\left(\int_{\mathcal{B}_0} \delta\boldsymbol{\Lambda_C} : (\boldsymbol{C}_{\boldsymbol{\phi}} - \boldsymbol{C}) \, dV \right) = \int_{\mathcal{B}_0} \delta\boldsymbol{\Lambda_C} : \left(\dot{\boldsymbol{C}}_{\boldsymbol{\phi}} - \dot{\boldsymbol{C}} \right) dV = 0;$$

$$\dot{\mathcal{W}}_{\boldsymbol{\Lambda_G}} = \frac{d}{dt}\left(\int_{\mathcal{B}_0} \delta\boldsymbol{\Lambda_G} : \left(\frac{1}{2}\boldsymbol{C} \times \boldsymbol{C} - \boldsymbol{G} \right) dV \right) = \int_{\mathcal{B}_0} \delta\boldsymbol{\Lambda_G} : \left(\boldsymbol{C} \times \dot{\boldsymbol{C}} - \dot{\boldsymbol{G}} \right) dV = 0; \qquad (19)$$

$$\dot{\mathcal{W}}_{\Lambda_C} = \frac{d}{dt}\left(\int_{\mathcal{B}_0} \delta\Lambda_C \left(\frac{1}{3}\boldsymbol{C} : \boldsymbol{G} - C \right) dV \right) = \int_{\mathcal{B}_0} \delta\Lambda_C \left(\frac{1}{3}\dot{\boldsymbol{C}} : \boldsymbol{G} + \frac{1}{3}\boldsymbol{C} : \dot{\boldsymbol{G}} - \dot{C} \right) dV = 0.$$

4.2. Balance laws and integrals in electro-elastodynamics

Starting with the stationary conditions (15) the following sections derive the global conservation laws that govern the motion of the EAP.

4.2.1. Global form for conservation of linear momentum

For a displacement field $\delta\boldsymbol{\phi} = \boldsymbol{\xi}$, with $\mathbb{R}^3 \ni \boldsymbol{\xi} = const.$, the stationary condition in $(15)_b$ leads to the global form of the conservation of linear momentum, namely

$$\dot{\boldsymbol{L}} - \boldsymbol{F}^{\text{ext}} = \boldsymbol{0}; \qquad \boldsymbol{L} = \int_{\mathcal{B}_0} \rho_0 \boldsymbol{v} \, dV; \qquad \boldsymbol{F}^{\text{ext}} = \int_{\partial_t \mathcal{B}_0} \boldsymbol{t}_0 \, dA + \int_{\mathcal{B}_0} \boldsymbol{f}_0 \, dV, \qquad (20)$$

where $\boldsymbol{L}$ represents the total linear momentum and $\boldsymbol{F}^{\text{ext}}$, the total external force. From (20) it is possible to conclude that $\boldsymbol{L}$ is a constant of motion for the case of vanishing external forces $\boldsymbol{F}^{\text{ext}}$.

4.2.2. Global form for conservation of angular momentum

For a rotational field $\delta\boldsymbol{\phi} = \boldsymbol{\xi} \times \boldsymbol{\phi}$, with $\mathbb{R}^3 \ni \boldsymbol{\xi} = const.$, the stationary condition in $(15)_b$ leads to the global form of the conservation of angular momentum, namely

$$\dot{\boldsymbol{J}} - \boldsymbol{M}^{\mathrm{ext}} = \boldsymbol{0}; \qquad \boldsymbol{J} = \int_{\mathcal{B}_0} \boldsymbol{\phi} \times \rho_0 \boldsymbol{v}\, dV; \qquad \boldsymbol{M}^{\mathrm{ext}} = \int_{\partial_t \mathcal{B}_0} \boldsymbol{\phi} \times \boldsymbol{t}_0\, dA + \int_{\mathcal{B}_0} \boldsymbol{\phi} \times \boldsymbol{f}_0\, dV, \quad (21)$$

where $\boldsymbol{J}$ represents the total angular momentum and $\boldsymbol{M}^{\mathrm{ext}}$, the total external torque. From (21), it is clear that $\boldsymbol{J}$ is a constant of motion for vanishing external torques $\boldsymbol{M}^{\mathrm{ext}}$.

4.2.3. Global form for Gauss's law

Taking $\delta\varphi = \xi$, with $\mathbb{R} \ni \xi = const.$, the stationary condition $\mathcal{W}_\varphi$ in $(15)_c$ leads to the global form of the Gauss' law

$$\int_{\mathcal{B}_0} \rho_0^e\, dV + \int_{\partial_\omega \mathcal{B}_0} \omega_0^e\, dA = 0. \tag{22}$$

Then, for time independent volumetric and surface electrical charges ρ_0^e and ω_0^e, equation (22) dictates that the total electric charge of the system is conserved and equal to zero.

4.2.4. Global form for conservation of energy

Let us replace the test functions $\{\delta\boldsymbol{v}, \delta\boldsymbol{\phi}, \delta\varphi, \delta\boldsymbol{D}_0\}$ in (15) with $\{\dot{\boldsymbol{v}}, \dot{\boldsymbol{\phi}}, \dot{\varphi}, \dot{\boldsymbol{D}}_0\} \in \mathbb{V}_0^\phi \times \mathbb{V}_0^\phi \times \mathbb{V}_0^\varphi \times \mathbb{V}^{\boldsymbol{D}_0}$. This yields

$$\begin{aligned}
&\int_{\mathcal{B}_0} \left(\boldsymbol{v} - \dot{\boldsymbol{\phi}}\right) \cdot \rho_0 \dot{\boldsymbol{v}}\, dV = 0; \\
&\int_{\mathcal{B}_0} \rho_0 \dot{\boldsymbol{v}} \cdot \dot{\boldsymbol{\phi}}\, dV + \int_{\mathcal{B}_0} \boldsymbol{\Lambda}_{\boldsymbol{C}} : \dot{\boldsymbol{C}}_\phi\, dV - \int_{\mathcal{B}_0} \boldsymbol{f}_0 \cdot \dot{\boldsymbol{\phi}}\, dV - \int_{\partial_t \mathcal{B}_0} \boldsymbol{t}_0 \cdot \dot{\boldsymbol{\phi}}\, dA = 0; \\
&\int_{\mathcal{B}_0} \boldsymbol{D}_0 \cdot \boldsymbol{\nabla}_0 \dot{\varphi}\, dV + \int_{\mathcal{B}_0} \rho_0^e \dot{\varphi}\, dV + \int_{\partial_\omega \mathcal{B}_0} \omega_0^e \dot{\varphi}\, dA = 0; \\
&\int_{\mathcal{B}_0} \dot{\boldsymbol{D}}_0 \cdot \left(\partial_{\boldsymbol{D}_0}\widetilde{W} + \boldsymbol{\nabla}_0\varphi\right) dV = 0.
\end{aligned} \tag{23}$$

Let us now replace $\{\delta\boldsymbol{C}, \delta\boldsymbol{G}, \delta C\}$ in (17) with $\{\dot{\boldsymbol{C}}, \dot{\boldsymbol{G}}, \dot{C}\} \in \mathbb{V}^{\boldsymbol{C}} \times \mathbb{V}^{\boldsymbol{G}} \times \mathbb{V}^C$, namely

$$\begin{aligned}
&\int_{\mathcal{B}_0} \dot{\boldsymbol{C}} : \left(\partial_{\boldsymbol{C}}\widetilde{W} - \boldsymbol{\Lambda}_{\boldsymbol{C}} + \boldsymbol{\Lambda}_{\boldsymbol{G}} \boldsymbol{\times} \boldsymbol{C} + \frac{1}{3}\Lambda_C \boldsymbol{G}\right) dV = 0; \\
&\int_{\mathcal{B}_0} \dot{\boldsymbol{G}} : \left(\partial_{\boldsymbol{G}}\widetilde{W} - \boldsymbol{\Lambda}_{\boldsymbol{G}} + \frac{1}{3}\Lambda_C \boldsymbol{C}\right) dV = 0; \\
&\int_{\mathcal{B}_0} \dot{C} \left(\partial_C\widetilde{W} - \Lambda_C\right) dV = 0.
\end{aligned} \tag{24}$$

Similarly, let us replace $\{\delta\boldsymbol{\Lambda}_{\boldsymbol{C}}, \delta\boldsymbol{\Lambda}_{\boldsymbol{G}}, \delta\Lambda_C\}$ in (19) with $\{\boldsymbol{\Lambda}_{\boldsymbol{C}}, \boldsymbol{\Lambda}_{\boldsymbol{G}}, \Lambda_C\} \in \mathbb{V}^{\boldsymbol{C}} \times \mathbb{V}^{\boldsymbol{G}} \times \mathbb{V}^C$, namely

$$\begin{aligned}
&\int_{\mathcal{B}_0} \boldsymbol{\Lambda}_{\boldsymbol{C}} : \left(\dot{\boldsymbol{C}}_\phi - \dot{\boldsymbol{C}}\right) dV = 0; \\
&\int_{\mathcal{B}_0} \boldsymbol{\Lambda}_{\boldsymbol{G}} : \left(\boldsymbol{C} \boldsymbol{\times} \dot{\boldsymbol{C}} - \dot{\boldsymbol{G}}\right) dV = 0; \\
&\int_{\mathcal{B}_0} \Lambda_C \left(\frac{1}{3}\dot{\boldsymbol{C}} : \boldsymbol{G} + \frac{1}{3}\boldsymbol{C} : \dot{\boldsymbol{G}} - \dot{C}\right) dV = 0.
\end{aligned} \tag{25}$$

Addition of equations (23), (24) and subtraction of (25) leads, in the case of time independent forces $\boldsymbol{f}_0$ and $\boldsymbol{t}_0$ and charges ρ_0^e and ω_0^e to

$$
\dot{K} + \int_{\mathcal{B}_0} \left(\partial_{\boldsymbol{C}}\widetilde{W} : \dot{\boldsymbol{C}} + \partial_{\boldsymbol{G}}\widetilde{W} : \dot{\boldsymbol{G}} + \partial_C \widetilde{W} \dot{C} + \partial_{\boldsymbol{D}_0}\widetilde{W} \cdot \dot{\boldsymbol{D}}_0 \right) dV
$$
$$
+ \int_{\mathcal{B}_0} \left(\boldsymbol{D}_0 \cdot \boldsymbol{\nabla}_0 \dot{\varphi} + \dot{\boldsymbol{D}}_0 \cdot \boldsymbol{\nabla}_0 \varphi \right) dV - \dot{\Pi}_{\text{ext}}^m (\boldsymbol{\phi}) - \dot{\Pi}_{\text{ext}}^e (\varphi) = 0,
\tag{26}
$$

where $K = \int_{\mathcal{B}_0} \frac{1}{2}\rho_0 \boldsymbol{v} \cdot \boldsymbol{v} \, dV$ in (26) represents the total kinetic energy of the system. Finally, equation (26) can be re-written as

$$
\dot{K} + \int_{\mathcal{B}_0} \dot{\widetilde{W}} (\boldsymbol{C}, \boldsymbol{G}, C, \boldsymbol{D}_0) \, dV + \int_{\mathcal{B}_0} \frac{d}{dt} (\boldsymbol{D}_0 \cdot \boldsymbol{\nabla}_0 \varphi) \, dV - \dot{\Pi}_{\text{ext}}^m (\boldsymbol{\phi}) - \dot{\Pi}_{\text{ext}}^e (\varphi) = 0.
\tag{27}
$$

It is therefore clear that in the case of time independent forces and electric charges, the following condition holds

$$
\dot{\mathcal{H}}_{\widetilde{W}} = 0; \qquad \mathcal{H}_{\widetilde{W}} = K + \int_{\mathcal{B}_0} \widetilde{W} (\boldsymbol{C}, \boldsymbol{G}, C, \boldsymbol{D}_0) \, dV + \int_{\mathcal{B}_0} \boldsymbol{D}_0 \cdot \boldsymbol{\nabla}_0 \varphi \, dV - \Pi_{\text{ext}}^m (\boldsymbol{\phi}) - \Pi_{\text{ext}}^e (\varphi),
\tag{28}
$$

and obviously the scalar field $\mathcal{H}_{\widetilde{W}}$ is preserved throughout the motion of the EAP. Note that $\mathcal{H}_{\widetilde{W}}$ can be regarded as the total Hamiltonian, defined through the following Legendre transformation

$$
\mathcal{H}_{\widetilde{W}} (\boldsymbol{p}, \boldsymbol{\phi}, \varphi, \boldsymbol{D}_0) = \sup_{\boldsymbol{v}} \left\{ \int_{\mathcal{B}_0} \boldsymbol{p} \cdot \boldsymbol{v} \, dV - \hat{L}_{\widetilde{W}} (\boldsymbol{v}, \boldsymbol{\phi}, \varphi, \boldsymbol{D}_0) \right\},
\tag{29}
$$

where $\boldsymbol{p} = \rho_0 \boldsymbol{v}$ denotes the linear momentum per unit undeformed volume $\mathcal{B}_0$.

5. Energy-Momentum integration scheme for electro-elastodynamics

The objective of this section is to propose an EM preserving time discretisation scheme for the set of weak forms given in (15), (17) and (18).

5.1. Design of the EM scheme

Let us consider a sequence of time steps $\{t_1, t_2, ..., t_n, t_{n+1}\}$, where t_{n+1} denotes the endpoint of the current time step. From the stationary conditions in (15), the following implicit one-step time integrator is proposed

$$
(\mathcal{W}_{\boldsymbol{v}})_{\text{algo}} = \int_{\mathcal{B}_0} \left(\boldsymbol{v}_{n+1/2} - \frac{\Delta\boldsymbol{\phi}}{\Delta t} \right) \cdot \rho_0 \delta\boldsymbol{v} \, dV = 0;
$$
$$
(\mathcal{W}_{\boldsymbol{\phi}})_{\text{algo}} = \int_{\mathcal{B}_0} \rho_0 \frac{\Delta\boldsymbol{v}}{\Delta t} \cdot \delta\boldsymbol{\phi} \, dV + \int_{\mathcal{B}_0} \boldsymbol{\Lambda}_{\boldsymbol{C}} : (D\boldsymbol{C}_{\boldsymbol{\phi}}[\delta\boldsymbol{\phi}])_{\text{algo}} \, dV - \int_{\mathcal{B}_0} \boldsymbol{f}_{0_{n+1/2}} \cdot \delta\boldsymbol{\phi} \, dV
$$
$$
- \int_{\partial_{\boldsymbol{t}}\mathcal{B}_0} \boldsymbol{t}_{0_{n+1/2}} \cdot \delta\boldsymbol{\phi} \, dA = 0;
\tag{30}
$$
$$
(\mathcal{W}_{\varphi})_{\text{algo}} = \int_{\mathcal{B}_0} \boldsymbol{D}_{0_{n+1/2}} \cdot \boldsymbol{\nabla}_0 \delta\varphi \, dV + \int_{\mathcal{B}_0} \rho_{0_{n+1/2}}^e \delta\varphi \, dV + \int_{\partial_\omega \mathcal{B}_0} \omega_{0_{n+1/2}}^e \delta\varphi \, dA = 0;
$$
$$
(\mathcal{W}_{\boldsymbol{D}_0})_{\text{algo}} = \int_{\mathcal{B}_0} \delta\boldsymbol{D}_0 \cdot \left(D_{\boldsymbol{D}_0}\widetilde{W} + \boldsymbol{\nabla}_0 \varphi_{n+1/2} \right) dV = 0.
$$

Note that $(\mathcal{W}_{\boldsymbol{v}})_{\text{algo}}$, $(\mathcal{W}_{\boldsymbol{\phi}})_{\text{algo}}$, $(\mathcal{W}_{\varphi})_{\text{algo}}$ and $(\mathcal{W}_{\boldsymbol{D}_0})_{\text{algo}}$ in (30) represent the algorithmic or time discrete versions of the stationary conditions in (15) and $(\bullet)_{n+1/2} = \frac{1}{2}\left((\bullet)_{n+1} + (\bullet)_n \right)$ and $\Delta(\bullet) = (\bullet)_{n+1} - (\bullet)_n$. Furthermore the Lagrange multipliers $\boldsymbol{\Lambda}_{(\bullet)}$ are constant throughout the

timestep, such that $\mathbf{\Lambda}_{(\bullet)} := \mathbf{\Lambda}_{(\bullet)_{n,n+1}}$. In equation $(30)_b$, where the algorithmic or time discrete directional derivative $(D\boldsymbol{C}_\phi[\delta\phi])^{\text{algo}}$ is defined as

$$(D\boldsymbol{C}_\phi[\delta\phi])_{\text{algo}} = \left((\boldsymbol{\nabla}_0\delta\phi)^T \boldsymbol{F}_{\phi_{n+1/2}} + \boldsymbol{F}_{\phi_{n+1/2}}^T \boldsymbol{\nabla}_0\delta\phi \right). \tag{31}$$

In addition, following [8], the algorithmic counterparts of the stationary conditions $\mathcal{W}_{\boldsymbol{C}}$, $\mathcal{W}_{\boldsymbol{G}}$ and $\mathcal{W}_C$ in (17) are

$$(\mathcal{W}_{\boldsymbol{C}})_{\text{algo}} = \int_{\mathcal{B}_0} \delta\boldsymbol{C} : \left(D_{\boldsymbol{C}}\widetilde{W} - \mathbf{\Lambda}_{\boldsymbol{C}} + \mathbf{\Lambda}_{\boldsymbol{G}} \times \boldsymbol{C}_{n+1/2} + \frac{1}{3}\Lambda_C \boldsymbol{G}_{n+1/2} \right) dV = 0;$$

$$(\mathcal{W}_{\boldsymbol{G}})_{\text{algo}} = \int_{\mathcal{B}_0} \delta\boldsymbol{G} : \left(D_{\boldsymbol{G}}\widetilde{W} - \mathbf{\Lambda}_{\boldsymbol{G}} + \frac{1}{3}\Lambda_C \boldsymbol{C}_{n+1/2} \right) dV = 0; \tag{32}$$

$$(\mathcal{W}_C)_{\text{algo}} = \int_{\mathcal{B}_0} \delta C \left(D_C\widetilde{W} - \Lambda_C \right) dV = 0.$$

Finally, following [8], the algorithmic counterpart of the stationary conditions $\mathcal{W}_{\mathbf{\Lambda}_{\boldsymbol{C}}}$, $\mathcal{W}_{\mathbf{\Lambda}_{\boldsymbol{G}}}$ and $\mathcal{W}_{\Lambda_C}$ (18) are

$$(\mathcal{W}_{\mathbf{\Lambda}_{\boldsymbol{C}}})_{\text{algo}} = \int_{\mathcal{B}_0} \delta\mathbf{\Lambda}_{\boldsymbol{C}} : \left(\boldsymbol{C}_{\phi_{n+1}} - \boldsymbol{C}_{n+1} \right) dV = 0;$$

$$(\mathcal{W}_{\mathbf{\Lambda}_{\boldsymbol{G}}})_{\text{algo}} = \int_{\mathcal{B}_0} \delta\mathbf{\Lambda}_{\boldsymbol{G}} : \left(\frac{1}{2}\boldsymbol{C}_{n+1} \times \boldsymbol{C}_{n+1} - \boldsymbol{G}_{n+1} \right) dV = 0; \tag{33}$$

$$(\mathcal{W}_{\Lambda_C})_{\text{algo}} = \int_{\mathcal{B}_0} \delta\Lambda_C \left(\frac{1}{3}\boldsymbol{C}_{n+1} : \boldsymbol{G}_{n+1} - C_{n+1} \right) dV = 0.$$

In (30) and (32), $\{D_{\boldsymbol{C}}\widetilde{W}, D_{\boldsymbol{G}}\widetilde{W}, D_C\widetilde{W}, D_{\boldsymbol{D}_0}\widetilde{W}\}$ represent the discrete derivatives (see next section) of the internal energy $\widetilde{W}$ with respect to $\{\boldsymbol{C}, \boldsymbol{G}, C, \boldsymbol{D}_0\}$, respectively. In particular $\{D_{\boldsymbol{C}}\widetilde{W}, D_{\boldsymbol{G}}\widetilde{W}, D_C\widetilde{W}, D_{\boldsymbol{D}_0}\widetilde{W}\}$ are the algorithmic or time discrete counterparts of $\{\partial_{\boldsymbol{C}}\widetilde{W}, \partial_{\boldsymbol{G}}\widetilde{W}, \partial_C\widetilde{W}, \partial_{\boldsymbol{D}_0}\widetilde{W}\}$ respectively.

5.1.1. Discretive derivatives of the internal energy

In this work, we make use of the same definition of the discrete derivative expressions $D_{\boldsymbol{C}}\widetilde{W}$, $D_{\boldsymbol{G}}\widetilde{W}$, $D_C\widetilde{W}$ and $D_{\boldsymbol{D}_0}\widetilde{W}$ of the internal energy proposed in [34]. These discrete derivatives were derived for the EM time integrator proposed in [34], which stemmed from the four field action integral $L_{\widetilde{W}}$ in (11). However, as it will be shown in Section 5.2, the expressions for the discrete derivatives $D_{\boldsymbol{C}}\widetilde{W}$, $D_{\boldsymbol{G}}\widetilde{W}$, $D_C\widetilde{W}$ and $D_{\boldsymbol{D}_0}\widetilde{W}$ in [34] comply also with the required conservation properties of the new time integrator in equations (30), (32) and (33).

For completeness, the expressions for the discrete derivatives have been included in Appendix A. It was proven in [34] that the proposed expressions for the discrete derivatives satisfy the following two crucial properties for the design of EM time integrators, namely:

- They fulfil the so called *directionality property* [18, 20],

$$D_{\boldsymbol{C}}\widetilde{W} : \Delta\boldsymbol{C} + D_{\boldsymbol{G}}\widetilde{W} : \Delta\boldsymbol{G} + D_C\widetilde{W}\Delta C + D_{\boldsymbol{D}_0}\widetilde{W} \cdot \Delta\boldsymbol{D}_0 = \Delta\widetilde{W}. \tag{34}$$

This property is critical for the algorithm in (30) to preserve energy under zero or time invariant external forces and electric charges.

- They are well defined in the limit as $||\Delta\boldsymbol{C}|| \to 0$, $||\Delta\boldsymbol{G}|| \to 0$, $||\Delta C|| \to 0$ and $||\Delta\boldsymbol{D}_0|| \to 0$. Furthermore, the proposed EM time integrator is second order accurate, such that

$$D_{\widetilde{\mathcal{V}}}\widetilde{W} = D_{\widetilde{\mathcal{V}}}\widetilde{W}\left(\widetilde{\mathcal{V}}_{n+1/2} \right) + O\left(\Delta t^2 \right); \qquad \widetilde{\mathcal{V}} = \{\boldsymbol{C}, \boldsymbol{G}, C, \boldsymbol{D}_0\}. \tag{35}$$

10

Remark 2. Although not pursued in this work (from the computational standpoint), it is possible to derive a Helmholtz-based EM time integrator very similar to the internal energy-based EM time integrator proposed in (30), (32) and (33). For the Helmholtz-based time integrator, depending upon the Helmholtz's energy functional $\widetilde{W}_\Phi$ in (10), similar to equation (30) one may introduce

$$
\begin{aligned}
(\mathcal{W}_{\boldsymbol{v}})_{\text{algo}} &= \int_{\mathcal{B}_0} \left(\boldsymbol{v}_{n+1/2} - \frac{\Delta\boldsymbol{\phi}}{\Delta t} \right) \cdot \rho_0 \delta\boldsymbol{v} \, dV = 0; \\
(\mathcal{W}_{\boldsymbol{\phi}})_{\text{algo}} &= \int_{\mathcal{B}_0} \rho_0 \frac{\Delta\boldsymbol{v}}{\Delta t} \cdot \delta\boldsymbol{\phi} \, dV + \int_{\mathcal{B}_0} \boldsymbol{\Lambda}_{\boldsymbol{C}} : (D\boldsymbol{C}_{\boldsymbol{\phi}}[\delta\boldsymbol{\phi}])_{\text{algo}} \, dV - \int_{\mathcal{B}_0} \boldsymbol{f}_{0_{n+1/2}} \cdot \delta\boldsymbol{\phi} \, dV \\
&\quad - \int_{\partial_t \mathcal{B}_0} \boldsymbol{t}_{0_{n+1/2}} \cdot \delta\boldsymbol{\phi} \, dA = 0; \\
(\mathcal{W}_{\varphi})_{\text{algo}} &= -\int_{\mathcal{B}_0} D_{\boldsymbol{E}_0}\widetilde{W}_\Phi \cdot \boldsymbol{\nabla}_0 \delta\varphi \, dV + \int_{\mathcal{B}_0} \rho^e_{0_{n+1/2}} \delta\varphi \, dV + \int_{\partial_\omega \mathcal{B}_0} \omega^e_{0_{n+1/2}} \delta\varphi \, dA = 0.
\end{aligned}
\tag{36}
$$

with $(D\boldsymbol{C}[\delta\boldsymbol{\phi}])^{\text{algo}}$ defined as in (31) and with $D_{\boldsymbol{E}_0}\widetilde{W}_\Phi$ representing the discretive derivative of $\widetilde{W}_\Phi$ with respect to $\boldsymbol{E}_0$. The algorithmic stationary conditions $\{(\mathcal{W}_{\boldsymbol{C}})_{\text{algo}}, (\mathcal{W}_{\boldsymbol{G}})_{\text{algo}}, (\mathcal{W}_C)_{\text{algo}}\}$ for the Helmholtz-based time integrator are

$$
\begin{aligned}
(\mathcal{W}_{\boldsymbol{C}})_{\text{algo}} &= \int_{\mathcal{B}_0} \delta\boldsymbol{C} : \left(D_{\boldsymbol{C}}\widetilde{W}_\Phi - \boldsymbol{\Lambda}_{\boldsymbol{C}} + \boldsymbol{\Lambda}_{\boldsymbol{G}} \times \boldsymbol{C}_{n+1/2} + \frac{1}{3}\Lambda_C \boldsymbol{G}_{n+1/2} \right) dV = 0; \\
(\mathcal{W}_{\boldsymbol{G}})_{\text{algo}} &= \int_{\mathcal{B}_0} \delta\boldsymbol{G} : \left(D_{\boldsymbol{G}}\widetilde{W}_\Phi - \boldsymbol{\Lambda}_{\boldsymbol{G}} + \frac{1}{3}\Lambda_C \boldsymbol{C}_{n+1/2} \right) dV = 0; \\
(\mathcal{W}_C)_{\text{algo}} &= \int_{\mathcal{B}_0} \delta C \left(D_C\widetilde{W}_\Phi - \Lambda_C \right) dV = 0,
\end{aligned}
\tag{37}
$$

where $\{D_{\boldsymbol{C}}\widetilde{W}_\Phi, D_{\boldsymbol{G}}\widetilde{W}_\Phi, D_C\widetilde{W}_\Phi\}$ represent the discrete derivatives of $\widetilde{W}_\Phi$ with respect to $\{\boldsymbol{C}, \boldsymbol{G}, C\}$. Finally, the algorithmic stationary conditions $\{(\mathcal{W}_{\boldsymbol{\Lambda}_{\boldsymbol{C}}})_{\text{algo}}, (\mathcal{W}_{\boldsymbol{\Lambda}_{\boldsymbol{G}}})_{\text{algo}}, (\mathcal{W}_{\Lambda_C})_{\text{algo}}\}$ are identical to those for the internal energy-based time integrator in (33), namely

$$
\begin{aligned}
(\mathcal{W}_{\boldsymbol{\Lambda}_{\boldsymbol{C}}})_{\text{algo}} &= \int_{\mathcal{B}_0} \delta\boldsymbol{\Lambda}_{\boldsymbol{C}} : \left(\boldsymbol{C}_{\boldsymbol{\phi}_{n+1}} - \boldsymbol{C}_{n+1} \right) dV = 0; \\
(\mathcal{W}_{\boldsymbol{\Lambda}_{\boldsymbol{G}}})_{\text{algo}} &= \int_{\mathcal{B}_0} \delta\boldsymbol{\Lambda}_{\boldsymbol{G}} : \left(\frac{1}{2}\boldsymbol{C}_{n+1} \times \boldsymbol{C}_{n+1} - \boldsymbol{G}_{n+1} \right) dV = 0; \\
(\mathcal{W}_{\Lambda_C})_{\text{algo}} &= \int_{\mathcal{B}_0} \delta\Lambda_{\boldsymbol{C}} \left(\frac{1}{3}\boldsymbol{C}_{n+1} : \boldsymbol{G}_{n+1} - C_{n+1} \right) dV = 0.
\end{aligned}
\tag{38}
$$

It can be proven that identical expressions for the discrete derivatives $\{D_{\boldsymbol{C}}\widetilde{W}_\Phi, D_{\boldsymbol{G}}\widetilde{W}_\Phi, D_C\widetilde{W}_\Phi, D_{\boldsymbol{E}_0}\widetilde{W}_\Phi\}$ as those for $\{D_{\boldsymbol{C}}\widetilde{W}, D_{\boldsymbol{G}}\widetilde{W}, D_C\widetilde{W}, D_{\boldsymbol{D}_0}\widetilde{W}\}$ in (30) (refer to Appendix A) guarantee the directionality property of the Helmholtz-based EM time in (36)-(38) and hence, its required conservation properties.

5.2. Discrete form of the balance laws and integrals in electro-dynamics

We next show that the proposed scheme is capable to satisfy important balance laws in analogy to the continous formulation treated in Section 4.2.

5.2.1. Discrete form of the global form for conservation of linear momentum

Following a similar procedure to that in Section 4.2.1, taking $\delta\boldsymbol{\phi} = \boldsymbol{\xi}$, with $\mathbb{R}^3 \ni \boldsymbol{\xi} = const.$ in $\mathcal{W}_\phi$ in $(30)_b$ yields

$$\frac{\Delta\boldsymbol{L}}{\Delta t} - \boldsymbol{F}^{\text{ext}}_{n+1/2} = \boldsymbol{0}; \qquad \boldsymbol{F}^{\text{ext}}_{n+1/2} = \int_{\partial_t\mathcal{B}_0} \boldsymbol{t}_{0_{n+1/2}}\, dA + \int_{\mathcal{B}_0} \boldsymbol{f}_{0_{n+1/2}}\, dV, \tag{39}$$

From equation (39) and for vanishing external forces $\boldsymbol{F}^{\text{ext}}_{n+1/2}$, it can be seen that the total linear momentum $\boldsymbol{L}$ remains constant.

5.2.2. Discrete form of the global form for conservation of angular momentum

Taking $\delta\boldsymbol{\phi} = \boldsymbol{\xi} \times \boldsymbol{\phi}_{n+1/2}$, with $\mathbb{R}^3 \ni \boldsymbol{\xi} = const.$ in $\mathcal{W}_\phi$ in $(30)_b$ yields

$$\frac{\Delta\boldsymbol{J}}{\Delta t} - \boldsymbol{M}^{\text{ext}}_{n+1/2} = \boldsymbol{0}; \qquad \boldsymbol{M}^{\text{ext}}_{n+1/2} = \int_{\partial_t\mathcal{B}_0} \boldsymbol{\phi}_{n+1/2} \times \boldsymbol{t}_{0_{n+1/2}}\, dA + \int_{\mathcal{B}_0} \boldsymbol{\phi}_{n+1/2} \times \boldsymbol{f}_{0_{n+1/2}}\, dV. \tag{40}$$

From equation (40) and for vanishing external torques $\boldsymbol{M}^{\text{ext}}_{n+1/2}$, it can be seen that the total angular momentum $\boldsymbol{J}$ remains constant.

5.2.3. Discrete form of the global form for the Gauss law

Taking $\delta\varphi = \xi$, with $\mathbb{R} \ni \xi = const.$, the weak form $\mathcal{W}_\varphi$ in (30) leads to

$$\int_{\mathcal{B}_0} \rho^e_{0_{n+1/2}}\, dV + \int_{\partial_\omega\mathcal{B}_0} \omega^e_{0_{n+1/2}}\, dA = 0. \tag{41}$$

For time independent volumetric and surface electrical charges ρ^e_0 and ω^e_0, (41) shows that the total electrical charge is zero.

5.2.4. Discrete form of the global form for conservation of energy

In this section, a similar analysis to that in Section 4.2.4 will be presented for the semi-discrete weak forms in (30), (32) and (33). For this purpose, we replace the test functions $\{\delta\boldsymbol{v}, \delta\boldsymbol{\phi}, \delta\varphi, \delta\boldsymbol{D}_0\}$ in (30) with $\{\Delta\boldsymbol{v}, \Delta\boldsymbol{\phi}, \Delta\varphi, \Delta\boldsymbol{D}_0\} \in \mathbb{V}_0^\phi \times \mathbb{V}_0^\phi \times \mathbb{V}_0^\varphi \times \mathbb{V}^{\boldsymbol{D}_0}$. This yields

$$\int_{\mathcal{B}_0} \left(\boldsymbol{v}_{n+1/2} - \frac{\Delta\boldsymbol{\phi}}{\Delta t}\right) \cdot \rho_0 \Delta\boldsymbol{v}\, dV = 0;$$

$$\int_{\mathcal{B}_0} \rho_0 \frac{\Delta\boldsymbol{v}}{\Delta t} \cdot \Delta\boldsymbol{\phi}\, dV + \int_{\mathcal{B}_0} \boldsymbol{\Lambda}_{\boldsymbol{C}} : (D\boldsymbol{C}_\phi[\Delta\boldsymbol{\phi}])_{\text{algo}}\, dV - \int_{\mathcal{B}_0} \boldsymbol{f}_0 \cdot \Delta\boldsymbol{\phi}\, dV - \int_{\partial_t\mathcal{B}_0} \boldsymbol{t}_0 \cdot \Delta\boldsymbol{\phi}\, dA = 0;$$

$$\int_{\mathcal{B}_0} \boldsymbol{D}_{0_{n+1/2}} \cdot \boldsymbol{\nabla}_0 \Delta\varphi\, dV + \int_{\mathcal{B}_0} \rho^e_{0_{n+1/2}} \Delta\varphi\, dV + \int_{\partial_\omega\mathcal{B}_0} \omega^e_{0_{n+1/2}} \Delta\varphi\, dA = 0;$$

$$\int_{\mathcal{B}_0} \Delta\boldsymbol{D}_0 \cdot \left(D_{\boldsymbol{D}_0}\widetilde{W} + \boldsymbol{\nabla}_0\varphi_{n+1/2}\right) dV = 0. \tag{42}$$

Furthermore, replace $\{\delta\boldsymbol{C}, \delta\boldsymbol{G}, \delta C\}$ in (32) with $\{\Delta\boldsymbol{C}, \Delta\boldsymbol{G}, \Delta C\} \in \mathbb{V}^{\boldsymbol{C}} \times \mathbb{V}^{\boldsymbol{G}} \times \mathbb{V}^{C}$, namely

$$\int_{\mathcal{B}_0} \Delta\boldsymbol{C} : \left(D_{\boldsymbol{C}}\widetilde{W} - \boldsymbol{\Lambda}_{\boldsymbol{C}} + \boldsymbol{\Lambda}_{\boldsymbol{G}} \times \boldsymbol{C}_{n+1/2} + \frac{1}{3}\Lambda_C \boldsymbol{G}_{n+1/2}\right) dV = 0;$$

$$\int_{\mathcal{B}_0} \Delta\boldsymbol{G} : \left(D_{\boldsymbol{G}}\widetilde{W} - \boldsymbol{\Lambda}_{\boldsymbol{G}} + \frac{1}{3}\Lambda_C \boldsymbol{C}_{n+1/2}\right) dV = 0; \tag{43}$$

$$\int_{\mathcal{B}_0} \Delta C \left(D_C\widetilde{W} - \Lambda_C\right) dV = 0.$$

Let us now replace $\{\delta\mathbf{\Lambda}_{\boldsymbol{C}}, \delta\mathbf{\Lambda}_{\boldsymbol{G}}, \delta\Lambda_C\}$ in (32) with $\{\mathbf{\Lambda}_{\boldsymbol{C}}, \mathbf{\Lambda}_{\boldsymbol{G}}, \Lambda_C\} \in \mathbb{V}^{\boldsymbol{C}} \times \mathbb{V}^{\boldsymbol{G}} \times \mathbb{V}^C$. Noticing that equation (32) is satisfied both at times t_{n+1} and t_n, the following expression can be obtained

$$\int_{\mathcal{B}_0} \mathbf{\Lambda}_{\boldsymbol{C}} : \Delta\left(\boldsymbol{C}_\phi - \boldsymbol{C}\right) dV = 0;$$

$$\int_{\mathcal{B}_0} \mathbf{\Lambda}_{\boldsymbol{G}} : \Delta\left(\frac{1}{2}\boldsymbol{C}\times\boldsymbol{C} - \boldsymbol{G}\right) dV = 0; \tag{44}$$

$$\int_{\mathcal{B}_0} \Lambda_C \Delta\left(\frac{1}{3}\boldsymbol{C} : \boldsymbol{G} - C\right) dV = 0.$$

Equations $(44)_b$ and $(44)_c$ can be conveniently written as

$$\int_{\mathcal{B}_0} \mathbf{\Lambda}_{\boldsymbol{G}} : \Delta\left(\frac{1}{2}\boldsymbol{C}\times\boldsymbol{C} - \boldsymbol{G}\right) dV = \int_{\mathcal{B}_0} \mathbf{\Lambda}_{\boldsymbol{G}} : \left(\Delta\boldsymbol{C}\times\boldsymbol{C}_{n+1/2} - \Delta\boldsymbol{G}\right) dV = 0;$$

$$\int_{\mathcal{B}_0} \Lambda_C \Delta\left(\frac{1}{3}\boldsymbol{C} : \boldsymbol{G} - C\right) dV = \int_{\mathcal{B}_0} \Lambda_C \left(\frac{1}{3}\Delta\boldsymbol{C} : \boldsymbol{G}_{n+1/2} + \frac{1}{3}\boldsymbol{C}_{n+1/2} : \Delta\boldsymbol{G} - \Delta C\right) dV = 0. \tag{45}$$

where use of the two following two identities has been made

$$\Delta\left(\frac{1}{2}\boldsymbol{C}\times\boldsymbol{C}\right) = \Delta\boldsymbol{C}\times\boldsymbol{C}_{n+1/2}$$

$$\Delta\left(\frac{1}{3}\boldsymbol{C} : \boldsymbol{G}\right) = \frac{1}{3}\Delta\boldsymbol{C} : \boldsymbol{G}_{n+1/2} + \frac{1}{3}\boldsymbol{C}_{n+1/2} : \Delta\boldsymbol{G}. \tag{46}$$

Addition of equation (42), (43) and substraction of $(44)_a$ and (45), yields

$$\Delta K + \int_{\mathcal{B}_0} \left(D_{\boldsymbol{C}}\widetilde{W} : \Delta\boldsymbol{C} + D_{\boldsymbol{G}}\widetilde{W} : \Delta\boldsymbol{G} + D_C\widetilde{W}\Delta C + D_{\boldsymbol{D}_0}\widetilde{W} \cdot \Delta\boldsymbol{D}_0\right) dV$$

$$+ \int_{\mathcal{B}_0} \Delta\left(\boldsymbol{D}_0 \cdot \boldsymbol{\nabla}_0\varphi\right) dV - \Delta\Pi_{\text{ext}}^m\left(\boldsymbol{\phi}\right) - \Delta\Pi_{\text{ext}}^e\left(\varphi\right) = 0. \tag{47}$$

in the case of time independent forces $\boldsymbol{f}_0$, $\boldsymbol{t}_0$ and charges ρ_0^e, ω_0^e.

Comparison of (47) and the definition of the total Hamiltonian $\mathcal{H}_{\widetilde{W}}$ in (28) enables to conclude that conservation of energy for the implicit one-step time integrator in equation (30) requires the directionality property in equation (34) to be satisfied. Four points have been crucial to arrive at this conclusion: i) the consideration of the algorithmic derivative $(D\boldsymbol{C}_\phi[\delta\boldsymbol{\phi}])_{\text{algo}}$ in (31); (ii) the consideration of $\boldsymbol{D}_{0_{n+1/2}}$ $(30)_c$ and of $\boldsymbol{\nabla}_0\varphi_{n+1/2}$ in $(30)_d$; (iii) the consideration of $\boldsymbol{C}_{n+1/2}$ and $\boldsymbol{G}_{n+1/2}$ in $(32)_a$ and $(32)_b$; (iv) the particular choice of kinematic constraints in (33) and their evaluation at time $n+1$. These four points led to the important implication that conservation of energy is guaranteed if the discrete derivatives $D_{\boldsymbol{C}}\widetilde{W}$, $D_{\boldsymbol{G}}\widetilde{W}$, $D_C\widetilde{W}$ and $D_{\boldsymbol{D}_0}\widetilde{W}$ comply with the directionality property in (34).

6. Finite Element implementation

As standard in finite elements, the domain $\mathcal{B}_0$ described in Section 2.1 and representing the EAP is sub-divided into a finite set of non-overlapping elements $e \in \mathbb{E}$ such that

$$\mathcal{B}_0 \approx \mathcal{B}_0^h = \bigcup_{e\in\mathbb{E}} \mathcal{B}_0^e. \tag{48}$$

The unknown fields $\{\boldsymbol{v}, \boldsymbol{\phi}, \varphi, \boldsymbol{D}_0, \boldsymbol{\mathcal{D}}, \mathbf{\Lambda}_{\boldsymbol{\mathcal{D}}}\}$ in the semi-discrete weak forms $\{\mathcal{W}_{\boldsymbol{v}}, \mathcal{W}_{\boldsymbol{\phi}}, \mathcal{W}_{\varphi}, \mathcal{W}_{\boldsymbol{D}_0}\}$ in (30), $\mathcal{W}_{\boldsymbol{\mathcal{D}}}$ in (32) and $\mathcal{W}_{\mathbf{\Lambda}_{\boldsymbol{\mathcal{D}}}}$ in (33) are discretised employing the following functional spaces

$\mathbb{V}^{\boldsymbol{\phi}^h} \times \mathbb{V}^{\boldsymbol{\phi}^h} \times \mathbb{V}^{\varphi^h} \times \mathbb{V}^{\boldsymbol{D}_0^h} \times \mathbb{V}^{\boldsymbol{\mathcal{D}}^h} \times \mathbb{V}^{\boldsymbol{\mathcal{D}}^h}$, with $\mathbb{V}^{\boldsymbol{\mathcal{D}}^h} = \{\mathbb{V}^{\boldsymbol{C}^h}, \mathbb{V}^{\boldsymbol{G}^h}, \mathbb{V}^{C^h}\}$ defined as

$$\mathbb{V}^{\boldsymbol{\phi}^h} = \{\boldsymbol{\phi} \in \mathbb{V}^{\boldsymbol{\phi}}; \quad \boldsymbol{\phi}^h\big|_{\mathcal{B}_0^e} = \sum_{a=1}^{n_{\text{node}}^{\boldsymbol{\phi}}} N_a^{\boldsymbol{\phi}} \boldsymbol{\phi}_a \mid \boldsymbol{\phi}_a = \bar{\boldsymbol{\phi}}^h \text{ on } \partial_{\boldsymbol{\phi}} \mathcal{B}_0^h\};$$

$$\mathbb{V}^{\varphi^h} = \{\varphi \in \mathbb{V}^{\varphi}; \quad \varphi^h\big|_{\mathcal{B}_0^e} = \sum_{a=1}^{n_{\text{node}}^{\varphi}} N_a^{\varphi} \varphi_a \mid \varphi_a = \bar{\varphi}^h \text{ on } \partial_{\varphi} \mathcal{B}_0^h\};$$

$$\mathbb{V}^{\boldsymbol{D}_0^h} = \{\boldsymbol{D}_0 \in \mathbb{V}^{\boldsymbol{D}_0}; \quad \boldsymbol{D}_0^h\big|_{\mathcal{B}_0^e} = \sum_{a=1}^{n_{\text{node}}^{\boldsymbol{D}_0}} N_a^{\boldsymbol{D}_0} \boldsymbol{D}_{0_a}\};$$ (49)

$$\mathbb{V}^{\boldsymbol{\mathcal{D}}^h} = \{\boldsymbol{\mathcal{D}} \in \mathbb{V}^{\boldsymbol{\mathcal{D}}}; \quad \boldsymbol{\mathcal{D}}_0^h\big|_{\mathcal{B}_0^e} = \sum_{a=1}^{n_{\text{node}}^{\boldsymbol{\mathcal{D}}}} N_a^{\boldsymbol{\mathcal{D}}} \boldsymbol{\mathcal{D}}_a\},$$

where for any field $\boldsymbol{\mathcal{Y}} \in \{\boldsymbol{\phi}, \varphi, \boldsymbol{D}_0, \boldsymbol{\mathcal{D}}, \boldsymbol{\Lambda_\mathcal{D}}\}$, $n_{\text{node}}^{\boldsymbol{\mathcal{Y}}}$ denotes the number of nodes per element of the discretisation associated with the field $\boldsymbol{\mathcal{Y}}$ and $N_a^{\boldsymbol{\mathcal{Y}}} : \mathcal{B}_0^e \to \mathbb{R}$, the ath shape function used for the interpolation of $\boldsymbol{\mathcal{Y}}$. In addition, $\boldsymbol{\mathcal{Y}}_a$ represents the value of the field $\boldsymbol{\mathcal{Y}}$ at the ath node of a given finite element. Similarly, following a Bubnov-Galerkin approach, the functional spaces for the virtual variations $\{\delta\boldsymbol{v}, \delta\boldsymbol{\phi}, \delta\varphi, \delta\boldsymbol{D}_0, \delta\boldsymbol{\mathcal{V}}, \delta\boldsymbol{\Lambda_\mathcal{D}}\} \in \mathbb{V}_0^{\boldsymbol{\phi}^h} \times \mathbb{V}_0^{\boldsymbol{\phi}^h} \times \mathbb{V}_0^{\varphi^h} \times \mathbb{V}^{\boldsymbol{D}_0^h} \times \mathbb{V}^{\boldsymbol{\mathcal{D}}^h} \times \mathbb{V}^{\boldsymbol{\mathcal{D}}^h}$ are defined as

$$\mathbb{V}_0^{\boldsymbol{\phi}^h} = \left\{\forall \boldsymbol{\phi} \in \mathbb{V}^{\boldsymbol{\phi}^h}; \quad \boldsymbol{\phi} = \boldsymbol{0} \text{ on } \partial_{\boldsymbol{\phi}} \mathcal{B}_0\right\};$$
$$\mathbb{V}_0^{\varphi^h} = \left\{\forall \varphi \in \mathbb{V}^{\varphi^h}; \quad \varphi = 0 \text{ on } \partial_{\varphi} \mathcal{B}_0\right\}.$$ (50)

Even though the relation between the time derivative of $\boldsymbol{\phi}$ and the velocity field $\boldsymbol{v}$ is considered in a weak manner (refer to the weak form $\mathcal{W}_{\boldsymbol{v}}$ in $(30)_a$), the consideration of equal functional spaces for both fields, namely $\boldsymbol{\phi} \in \mathbb{V}^{\boldsymbol{\phi}^h}$ and $\boldsymbol{v} \in \mathbb{V}^{\boldsymbol{\phi}^h}$ enables to conclude that equation $(30)_a$ holds strongly at the discrete level, namely[6]

$$\frac{\Delta\boldsymbol{\phi}}{\Delta t} = \boldsymbol{v}_{n+1/2}. \qquad (51)$$

Consideration of the functional spaces for $\{\boldsymbol{v}, \boldsymbol{\phi}, \varphi, \boldsymbol{D}_0, \boldsymbol{\mathcal{D}}, \boldsymbol{\Lambda_\mathcal{D}}\}$ and $\{\delta\boldsymbol{v}, \delta\boldsymbol{\phi}, \delta\varphi, \delta\boldsymbol{D}_0, \delta\boldsymbol{\mathcal{D}}, \delta\boldsymbol{\Lambda_\mathcal{D}}\}$ in (49) and (50) enables the weak forms $\mathcal{W}_{\boldsymbol{\phi}}$, $\mathcal{W}_{\varphi}$ and $\mathcal{W}_{\boldsymbol{D}_0}$ in (30), $\mathcal{W}_{\boldsymbol{\mathcal{D}}}$ in (32) and $\mathcal{W}_{\boldsymbol{\Lambda_\mathcal{D}}}$ in (33) to be written in terms of their associated elemental residual contributions, namely

$$\mathcal{W}_{\boldsymbol{\phi}} = \sum_{e=1}^{N} \delta\boldsymbol{\phi}_a \cdot \boldsymbol{R}_{a,e}^{\boldsymbol{\phi}}; \qquad \mathcal{W}_{\varphi} = \sum_{e=1}^{N} \delta\varphi_a R_{a,e}^{\varphi}; \qquad \mathcal{W}_{\boldsymbol{D}_0} = \sum_{e=1}^{N} \delta\boldsymbol{D}_{0_a} \cdot \boldsymbol{R}_{a,e}^{\boldsymbol{D}_0};$$

$$\mathcal{W}_{\boldsymbol{C}} = \sum_{e=1}^{N} \delta\boldsymbol{C}_a : \boldsymbol{R}_{a,e}^{\boldsymbol{C}}; \qquad \mathcal{W}_{\boldsymbol{G}} = \sum_{e=1}^{N} \delta\boldsymbol{G}_a : \boldsymbol{R}_{a,e}^{\boldsymbol{G}}; \qquad \mathcal{W}_{C} = \sum_{e=1}^{N} \delta C_a R_{a,e}^{C}; \qquad (52)$$

$$\mathcal{W}_{\boldsymbol{\Lambda_C}} = \sum_{e=1}^{N} \delta\boldsymbol{\Lambda_C}_a : \boldsymbol{R}_{a,e}^{\boldsymbol{\Lambda_C}}; \qquad \mathcal{W}_{\boldsymbol{\Lambda_G}} = \sum_{e=1}^{N} \delta\boldsymbol{\Lambda_G}_a : \boldsymbol{R}_{a,e}^{\boldsymbol{\Lambda_G}}; \qquad \mathcal{W}_{\Lambda_C} = \sum_{e=1}^{N} \delta\Lambda_{C_a} R_{a,e}^{\Lambda_C},$$

---

[6]Notice that in the discrete setting, $(30)_a$ transforms into a mass matrix multiplied by the discrete vector version of $\frac{\Delta\boldsymbol{\phi}}{\Delta t} - \boldsymbol{v}_{n+1/2}$ equaling zero. For this to hold, given the positive definite nature of the mass matrix, the discrete vector version of $\frac{\Delta\boldsymbol{\phi}}{\Delta t} - \boldsymbol{v}_{n+1/2}$ must be zero. Thus, equation (51) holds at the nodes of the discretisation and thus, at the quadrature points.

where N denotes the number of elements for the underlying discretisation. Each of the residual contributions $\{\boldsymbol{R}_{a,e}^{\phi}, R_{a,e}^{\varphi}, \boldsymbol{R}_{a,e}^{\boldsymbol{D_0}}\}$ in (52) can be expressed as[7]

$$\boldsymbol{R}_{a,e}^{\phi} = \int_{\mathcal{B}_0^e} \rho_0 N_a^{\phi} \left(2\frac{\Delta\phi}{\Delta t^2} - 2\frac{\boldsymbol{v}_n}{\Delta t} \right) dV + \int_{\mathcal{B}_0^e} \left(\boldsymbol{F}_{\phi_{n+1/2}}\boldsymbol{\Lambda_C} \right) \boldsymbol{\nabla}_0 N_a^{\phi} \, dV + \int_{\mathcal{B}_0^e} N_a^{\phi} \boldsymbol{f}_{0_{n+1/2}} \, dV;$$

$$R_{a,e}^{\varphi} = \int_{\mathcal{B}_0^e} \boldsymbol{D}_{0_{n+1/2}} \cdot \boldsymbol{\nabla}_0 N_a^{\varphi} \, dV + \int_{\mathcal{B}_0^e} N_a^{\varphi} \rho_{0_{n+1/2}}^e \, dV; \qquad (53)$$

$$\boldsymbol{R}_{a,e}^{\boldsymbol{D_0}} = \int_{\mathcal{B}_0^e} N_a^{\boldsymbol{D_0}} \left(D_{\boldsymbol{D_0}}\widetilde{W} + \boldsymbol{\nabla}_0 \varphi_{n+1/2} \right) dV,$$

where use of equation (51) has been made of in the inertial term of the residual $\boldsymbol{R}_{a,e}^{\phi}$ in $(53)_a$. The residual contributions $\{\boldsymbol{R}_{a,e}^{\boldsymbol{C}}, \boldsymbol{R}_{a,e}^{\boldsymbol{G}}, R_{a,e}^{C}\}$ in (52) can be expressed as

$$\boldsymbol{R}_{a,e}^{\boldsymbol{C}} = \int_{\mathcal{B}_0} N_a^{\boldsymbol{C}} \left(D_{\boldsymbol{C}}\widetilde{W} - \boldsymbol{\Lambda_C} + \boldsymbol{\Lambda_G} \times \boldsymbol{C}_{n+1/2} + \frac{1}{3}\Lambda_C \boldsymbol{G}_{n+1/2} \right) dV;$$

$$\boldsymbol{R}_{a,e}^{\boldsymbol{G}} = \int_{\mathcal{B}_0} N_a^{\boldsymbol{G}} \left(D_{\boldsymbol{G}}\widetilde{W} - \boldsymbol{\Lambda_G} + \frac{1}{3}\Lambda_C \boldsymbol{C}_{n+1/2} \right) dV; \qquad (54)$$

$$R_{a,e}^{C} = \int_{\mathcal{B}_0} N_a^{C} \left(D_C\widetilde{W} - \Lambda_C \right) dV.$$

Finally, the residual contributions $\{\boldsymbol{R}_{a,e}^{\boldsymbol{\Lambda_C}}, \boldsymbol{R}_{a,e}^{\boldsymbol{\Lambda_G}}, R_{a,e}^{\Lambda_C}\}$ in (52) can be expressed as

$$\boldsymbol{R}_{a,e}^{\boldsymbol{\Lambda_C}} = \int_{\mathcal{B}_0} N_a^{\boldsymbol{C}} \left(\boldsymbol{C}_{\phi_{n+1}} - \boldsymbol{C}_{n+1} \right) dV;$$

$$\boldsymbol{R}_{a,e}^{\boldsymbol{\Lambda_G}} = \int_{\mathcal{B}_0} N_a^{\boldsymbol{G}} \left(\frac{1}{2}\boldsymbol{C}_{n+1} \times \boldsymbol{C}_{n+1} - \boldsymbol{G}_{n+1} \right) dV; \qquad (55)$$

$$R_{a,e}^{\Lambda_C} = \int_{\mathcal{B}_0} N_a^{C} \left(\frac{1}{3}\boldsymbol{C}_{n+1} : \boldsymbol{G}_{n+1} - C_{n+1} \right) dV.$$

A consistent linearisation of the nonlinear residual contributions (53), (54) and (55) has been used in this work. Finally, in order to reduce the computational cost of the proposed formulation, a piecewise discontinuous interpolation of the fields $\{\boldsymbol{D_0}, \boldsymbol{C}, \boldsymbol{G}, C, \boldsymbol{\Lambda_C}, \boldsymbol{\Lambda_G}, \Lambda_C\}$ is followed. A standard static condensation procedure [9, 36] is used to condense out the degrees of freedom of the fields $\{\boldsymbol{D_0}, \boldsymbol{C}, \boldsymbol{G}, C, \boldsymbol{\Lambda_C}, \boldsymbol{\Lambda_G}, \Lambda_C\}$. Note that appropriate choices of functional spaces for the different unknown fields are restricted by appropriate stability (or inf-sup) conditions (see [8]).

7. Numerical examples

In order to examine the proposed mixed formulation in the field of electro-elastodynamics, a series of numerical examples are investigated. In particular, four quasi-static examples (see Sec. 7.1-7.3) are presented in order to demonstrate the spatial convergence of the formulation for two different finite elements. Subsequently, four dynamic examples (see Sec. 7.4-7.7) are presented in order to investigate the performance of the proposed EM time integration scheme when compared to the classical midpoint rule. In all the examples the internal energy is split into a purely mechanical and a coupled electromechanical part:

$$\widetilde{W}\left(\boldsymbol{C}, \boldsymbol{G}, C, \boldsymbol{D_0} \right) = \widetilde{W}_m\left(\boldsymbol{C}, \boldsymbol{G}, C \right) + \widetilde{W}_{em}\left(\boldsymbol{C}, C, \boldsymbol{D_0} \right). \qquad (56)$$

---

[7]For simplicity, the external contributions on the boundary of the continuum and associated with $\boldsymbol{t}_0$ and ω_0^e have not been included in (53).

Herein we focus on ideal dielectric elastomers modelled by

$$\widetilde{W}_{em}\left(\boldsymbol{C}, C, \boldsymbol{D}_0\right) = \frac{1}{2\varepsilon_r\varepsilon_0 C^{1/2}} \boldsymbol{D}_0 \cdot \boldsymbol{C}\boldsymbol{D}_0, \tag{57}$$

where ε_0 represents the permittivity of vacuum $\varepsilon_0 = 8.8541 \times 10^{-12} NC^{-2}m^{-2}$ and ϵ_r is the relative permittivity (see [17] for more informations). An isotropic behaviour is considered for the mechanical component $\widetilde{W}_m$ in the examples in Sec. 7.1-7.5 and 7.7. Specifically, a Mooney-Rivlin strain energy functional is used, defined as

$$\widetilde{W}_m^{MR}\left(\boldsymbol{C}, \boldsymbol{G}, C\right) = \frac{\mu_1}{2}(\mathrm{tr}\,\boldsymbol{C} - 3) + \frac{\mu_2}{2}(\mathrm{tr}\,\boldsymbol{G} - 3) - (\mu_1 + 2\mu_2)\ln C^{1/2} + \frac{\lambda}{2}\left(C^{1/2} - 1\right)^2, \tag{58}$$

where μ_1, μ_2 and λ are material parameters with units of stress related to the Lamé parameters $\{\mu_0, \lambda_0\}$ in the origin as $\mu_0 = \mu_1 + \mu_2$ and $\lambda_0 = \lambda + 2\mu_2$. For the examples in Sec. 7.3 and 7.6, anisotropic effects are taken into account. In particular, a transversely isotropic mechanical model is employed for which the mechanical contribution of the internal energy is additively decomposed into isotropic and anisotropic parts as

$$\widetilde{W}_m\left(\boldsymbol{C}, \boldsymbol{G}, C\right) = \widetilde{W}_m^{\mathrm{iso}}\left(\boldsymbol{C}, \boldsymbol{G}, C\right) + \widetilde{W}_m^{\mathrm{aniso}}\left(\boldsymbol{C}, \boldsymbol{G}, C\right). \tag{59}$$

The isotropic contribution $\widetilde{W}_m^{\mathrm{iso}}\left(\boldsymbol{C}, \boldsymbol{G}, C\right)$ is given in (58), whereas the anisotropic contribution is chosen as in [45] as

$$\widetilde{W}_m^{\mathrm{aniso}}\left(\boldsymbol{C}, \boldsymbol{G}, C\right) = \frac{\mu_3}{g_{\boldsymbol{C}} + 1}\left(\mathrm{tr}(\boldsymbol{C}\,\boldsymbol{M})\right)^{g_{\boldsymbol{C}}+1} + \frac{\mu_3}{g_{\boldsymbol{G}} + 1}\left(\mathrm{tr}(\boldsymbol{G}\,\boldsymbol{M})\right)^{g_{\boldsymbol{G}}+1} + \frac{\mu_3}{g_C} C^{-g_C}, \tag{60}$$

where

$$\boldsymbol{M} = \boldsymbol{N}_0 \otimes \boldsymbol{N}_0, \tag{61}$$

and $\boldsymbol{N}_0$ denotes the fibre direction in the reference configuration. In addition, $\mu_3 > 0$, $g_{\boldsymbol{C}} > 0$, $g_{\boldsymbol{G}} > 0$ and $g_C \geq 1$ are suitable anisotropic material parameters (see [45] for more details).
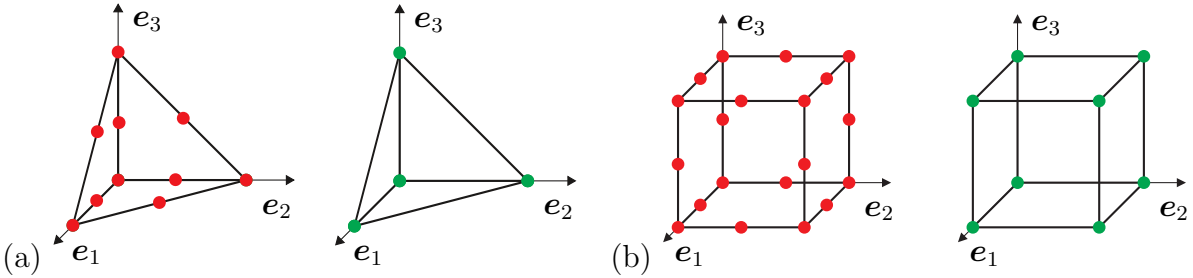
Figure 2: (a) Ten node quadratic/four node linear tetrahedron (*tet 10/4*) elements; (b) Twenty node serendipity/eight node tri-linear hexahedron (*hex 20/8*) elements. Quadratic continuous interpolation spaces $P2^C/Q2^C$ and linear discontinuuous interpolation spaces $P1^D/Q1^D$ are employed such that $\{\phi, \Phi\} \in P2^C/Q2^C$ (elements with red nodes) and $\{\boldsymbol{D}_0, \boldsymbol{\mathcal{D}}, \boldsymbol{\Lambda}\} \in P1^D/Q1^D$ (elements with green nodes).

For all examples, either ten node quadratic/four node linear tetrahedron elements, in the following referred to as *tet 10/4*, or twenty node serendipity/eight node tri-linear hexahedron elements, in the following referred to as *hex 20/8*, are employed (see Fig. 2 for more details). A standard static condensation procedure has been carried out in all examples in order to condense out the discontinuous fields $\{\boldsymbol{D}_0, \boldsymbol{\mathcal{D}}, \boldsymbol{\Lambda}\}$.

16

7.1. Patch test

The objective of this example is:

O1.I To test the consistency of the proposed element formulation by means of the well-known three-dimensional patch test (see [29]), verifying that the element formulation is able to recover homogeneous states of stress and electrical potential.

An initial domain Ω_0 in the form of a cube is considered with dimensions $(0,1)[\text{m}] \times (0,1)[\text{m}] \times (0,1)[\text{m}]$ (see Fig. 3). The cube is restricted to move such that only an expansion into the e_1-e_2-plane is permitted. Accordingly, Dirichlet boundary conditions are employed on the faces at $x_i = 0$ where $i = 1, 2, 3$ and are fixed in the respective e_i-directions. Further Dirichlet boundary conditions are applied on the top face as depicted in Fig. 3 (left), i.e. the upper boundary (face at $x_3 = 1$) is displaced in the negative e_3-direction reducing the initial height by a factor of two. Neither electrical Dirichlet nor Neumann boundary conditions are imposed. The material and simulation parameters are provided by Tab. 1. A regular mesh comprised of 64 *hex 20/8* elements and 1700 displacement and electrical potential unknowns and an initially distorted mesh comprised of 7 *hex 20/8* elements and 192 (condensed) unknowns (see Fig. 3) are employed. The final von Mises stress distribution[8] and the electrical potential distribution are shown in Fig. 4 for the regular mesh and for the initially distorted mesh, respectively. As can be observed, for both meshes homogeneous states of stress and electrical potential are reproduced.
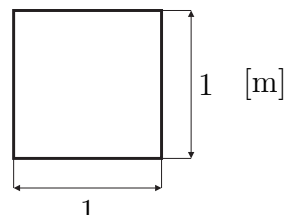
Mechanical parameters	μ_1	$1/2 \times 10^5$	Pa	Geometry of the body
	μ_2	1×10^5	Pa	
	λ	1×10^6	Pa	
Electrical parameters	ϵ_0	8.854×10^{-12}	$\text{A}^2\,\text{s}^4\,\text{kg}^{-1}\,\text{m}^{-3}$	
	ϵ_r	4	$-$	
Ref. potential	φ_0	0	V	
Newton tolerance	ϵ	$1 \cdot 10^{-6}$	-	

Table 1: Patch test: Material and simulation parameters.
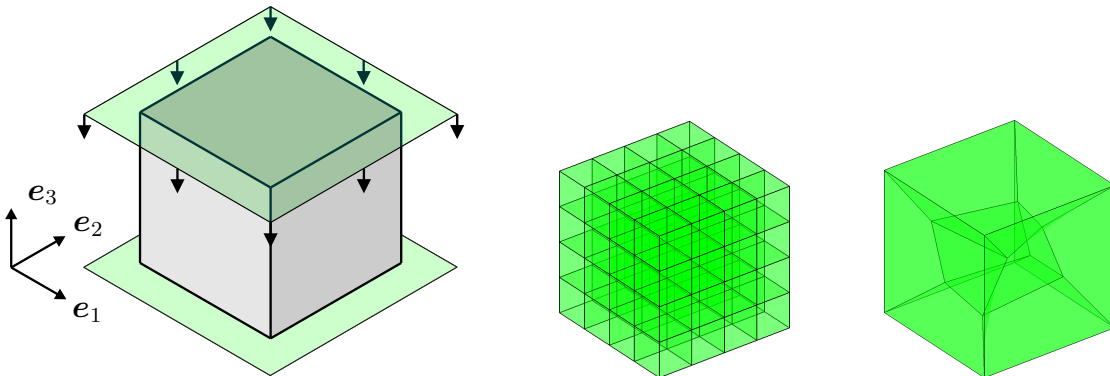
Figure 3: Patch test: Boundary conditions (left), initial regular mesh (middle) and initial distorted mesh (right).

---

[8]The von Mises stress is computed by $\sigma_{vM} = \sqrt{\sigma_{11}^2 + \sigma_{22}^2 + \sigma_{33}^2 - \sigma_{11}\,\sigma_{22} - \sigma_{11}\,\sigma_{33} - \sigma_{22}\,\sigma_{33} + 3\,(\sigma_{12}^2 + \sigma_{13}^2 + \sigma_{23}^2)}$, where σ_{ij}, $i,j = 1,2,3$ denotes the components of the Cauchy stress tensor.
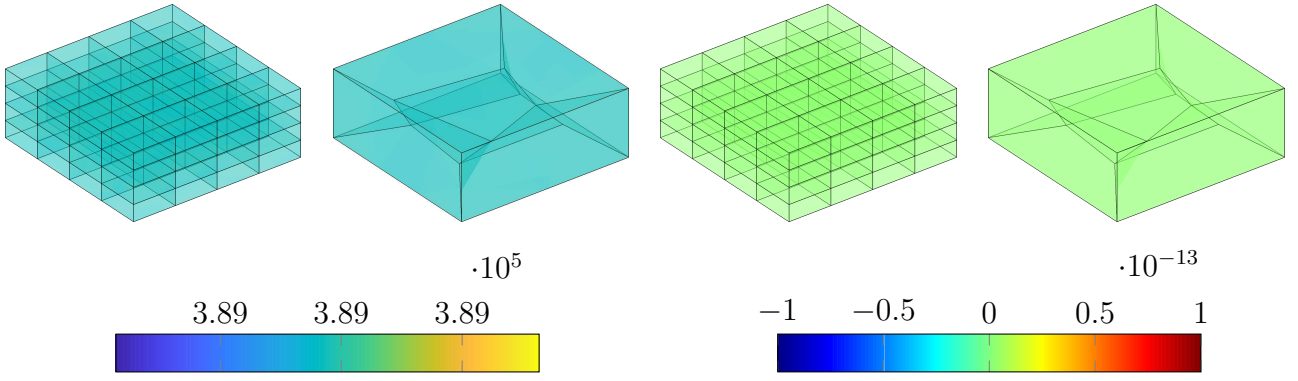
Figure 4: Patch test: Von Mises stress distribution (left) and electrical potential distribution (right) for patch tests with regular and initially distorted meshes.

7.2. Static convergence analysis

Mechanical parameters	μ_1	$1/2$	Pa	Geometry of the body
	μ_2	1	Pa	
	λ	1	Pa	
Electrical parameters	ϵ_0	8.854×10^{-12}	$\mathrm{A^2\,s^4\,kg^{-1}\,m^{-3}}$	
	ϵ_r	4	–	
Ref. potential	φ_0	0	V	
Newton tolerance	ϵ	$1 \cdot 10^{-7}$	-	

Table 2: Static convergence analysis: Material and simulation parameters.
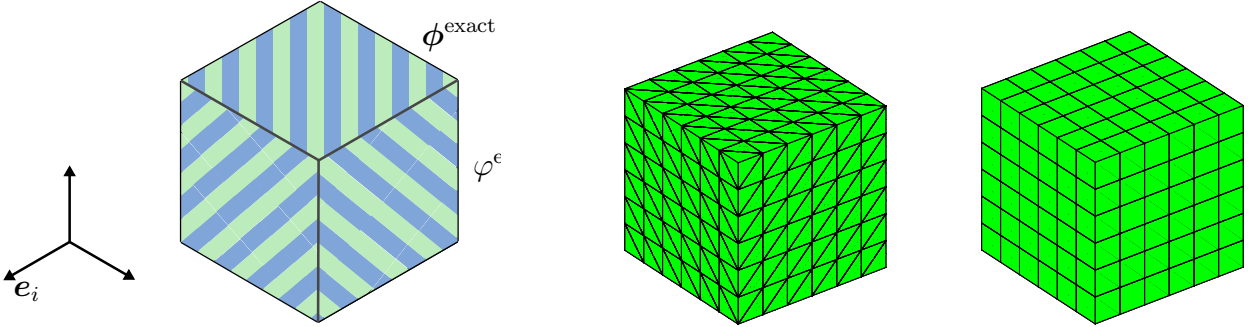
Figure 5: Static convergence analysis: For all outer faces (patterned surfaces) Dirichlet boundary conditions are imposed for ϕ^{exact} and φ^{exact} given in (62) (left). Typical *tet 10/4* (centred) and *hex 20/8* (right) meshes are shown.

The objectives of this example are:

O2.I To demonstrate the p-order of accuracy of the mixed formulation when using elements *tet 10/4* and *hex 20/8* (see [42] for more details).

A cube Ω_0 $(0,1)[\mathrm{m}] \times (0,1)[\mathrm{m}] \times (0,1)[\mathrm{m}]$ is considered (see Fig. 5) where geometry, boundary conditions and material parameters are provided in Tab. 2 and Fig. 5. The analysis of an ad hoc manufactured problem is carried out following a similar procedure as that described in [42].

18

The following exact fields associated with the deformed configuration $\boldsymbol{\phi}^{\text{exact}}$ and the electrical potential φ^{exact} are chosen,

$$\boldsymbol{\phi}^{\text{exact}} = \boldsymbol{X} + \gamma_1 \sin(X)\, \boldsymbol{e}_1 + \gamma_2 \cos(Y)\, \boldsymbol{e}_2 + \gamma_3\, (\sin(Z) + \cos(Z))\, \boldsymbol{e}_3; \quad \varphi^{\text{exact}} = \varphi_0 \sin(X), \quad (62)$$

where $\gamma_i = \frac{i}{2}\,e\text{-}1$, $i = 1, 2, 3$ and $\varphi_0 = 1\,e4$ (cf. [42]). It is now possible to derive:

- the deformation gradient

$$\boldsymbol{F}(\boldsymbol{\phi}^{\text{exact}}) = (1 + \gamma_1 \cos(X))\, \boldsymbol{e}_1 \otimes \boldsymbol{E}_1 + (1 - \gamma_2 \sin(Y))\, \boldsymbol{e}_2 \otimes \boldsymbol{E}_2 + (1 + \gamma_3\, (\cos(Z) - \sin(Z)))\, \boldsymbol{e}_3 \otimes \boldsymbol{E}_3,$$

- the Cauchy-Green tensor, its cofactor and its determinant

$$\boldsymbol{C}^{\text{exact}} = \boldsymbol{F}^{\text{T}}(\boldsymbol{\phi}^{\text{exact}})\, \boldsymbol{F}(\boldsymbol{\phi}^{\text{exact}}); \quad \boldsymbol{G}^{\text{exact}} = \frac{1}{2}\, \boldsymbol{C}^{\text{exact}} \times \boldsymbol{C}^{\text{exact}}; \quad C^{\text{exact}} = \frac{1}{3}\, \boldsymbol{G}^{\text{exact}} : \boldsymbol{C}^{\text{exact}},$$

- the electric displacement field is computed via $(6)_1$ and $(15)_4$

$$\boldsymbol{E}_0^{\text{exact}} = -\boldsymbol{\nabla}_0 \varphi^{\text{exact}} = -\varphi_0 \cos(X)\, \boldsymbol{E}_1; \quad \boldsymbol{E}_0^{\text{exact}} = \partial_{\boldsymbol{D}_0} \widetilde{W}^{\text{exact}} = \frac{1}{\varepsilon_r \varepsilon_0 (C^{\text{exact}})^{1/2}} \boldsymbol{C}^{\text{exact}} \boldsymbol{D}_0^{\text{exact}}$$

$$\Leftrightarrow \quad \boldsymbol{D}_0^{\text{exact}} = \varepsilon_r \varepsilon_0 (C^{\text{exact}})^{1/2} (\boldsymbol{C}^{\text{exact}})^{-1} \boldsymbol{E}_0^{\text{exact}} = -\varepsilon_r \varepsilon_0 \varphi_0 \cos(X)(C^{\text{exact}})^{1/2}(\boldsymbol{C}^{\text{exact}})^{-1} \boldsymbol{E}_1,$$

- the work-conjugates computed from (17)

$$\Lambda_C{}^{\text{exact}} = \partial_C \widetilde{W}^{\text{exact}}\, (\boldsymbol{C}, \boldsymbol{G}, C, \boldsymbol{D}_0);$$

$$\boldsymbol{\Lambda_G}^{\text{exact}} = \partial_{\boldsymbol{G}} \widetilde{W}^{\text{exact}}\, (\boldsymbol{C}, \boldsymbol{G}, C, \boldsymbol{D}_0) + \frac{1}{3}\, \Lambda_C{}^{\text{exact}}\, \boldsymbol{C}^{\text{exact}};$$

$$\boldsymbol{\Lambda_C}^{\text{exact}} = \partial_{\boldsymbol{C}} \widetilde{W}^{\text{exact}}\, (\boldsymbol{C}, \boldsymbol{G}, C, \boldsymbol{D}_0) + \boldsymbol{\Lambda_G}^{\text{exact}} \times \boldsymbol{C}^{\text{exact}} + \frac{1}{3}\, \Lambda_C{}^{\text{exact}}\, \boldsymbol{G}^{\text{exact}},$$

where

$$\partial_C \widetilde{W}^{\text{exact}} = \lambda\, (1 - \frac{1}{(C^{\text{exact}})^{1/2}}) - \frac{\mu_1 + 2\,\mu_2}{2\, C^{\text{exact}}} - \frac{1}{4\, \epsilon_r\, \epsilon_0}\, (C^{\text{exact}})^{-3/2}\, \boldsymbol{D}_0^{\text{exact}} \cdot (\boldsymbol{C}^{\text{exact}}\, \boldsymbol{D}_0^{\text{exact}});$$

$$\partial_{\boldsymbol{C}} \widetilde{W}^{\text{exact}} = \frac{\mu_1}{2}\, \boldsymbol{I} + \frac{1}{2\, \epsilon_r\, \epsilon_0\, (C^{\text{exact}})^{1/2}}\, (\boldsymbol{D}_0^{\text{exact}} \otimes \boldsymbol{D}_0^{\text{exact}});$$

$$\partial_{\boldsymbol{G}} \widetilde{W}^{\text{exact}} = \frac{\mu_2}{2}\, \boldsymbol{I},$$

- the second Piola-Kirchhoff stress tensor computed as

$$\boldsymbol{S}^{\text{exact}} = 2\, \boldsymbol{\Lambda_C}^{\text{exact}},$$

- volume load and charge densities

$$\boldsymbol{B}^{\text{exact}} = -\operatorname{Div}(\boldsymbol{F}^{\text{exact}}\, \boldsymbol{S}^{\text{exact}}); \quad \rho_0^{\text{exact}} = \operatorname{Div}(\boldsymbol{D}_0^{\text{exact}}).$$

Exact solutions provided by (62) are compared against the numerical solutions obtained by imposing the analytically computed volume load and charge density. The exact solution in (62) is imposed as a Dirichlet boundary at all six surfaces of the cube (see Fig. 5). The h-convergence rate for the different variables is studied where the L^2 norm of the error is employed, i.e.

$$\|e_\bullet\|_{L^2} = \frac{\|(\bullet) - (\bullet)^{\text{exact}}\|_{L^2}}{\|(\bullet)^{\text{exact}}\|_{L^2}}, \tag{63}$$

where ($\bullet$) denotes the numerically computed variable and ($\bullet^{\text{exact}}$) its analytical counterpart. Fig. 7 shows the convergence results for the displacement and electrical potential. A typical numerical solution with von Mises stress and electrical potential distribution is depicted in Fig. 6 for the *tet 10/4* and the *hex 20/8* elements.
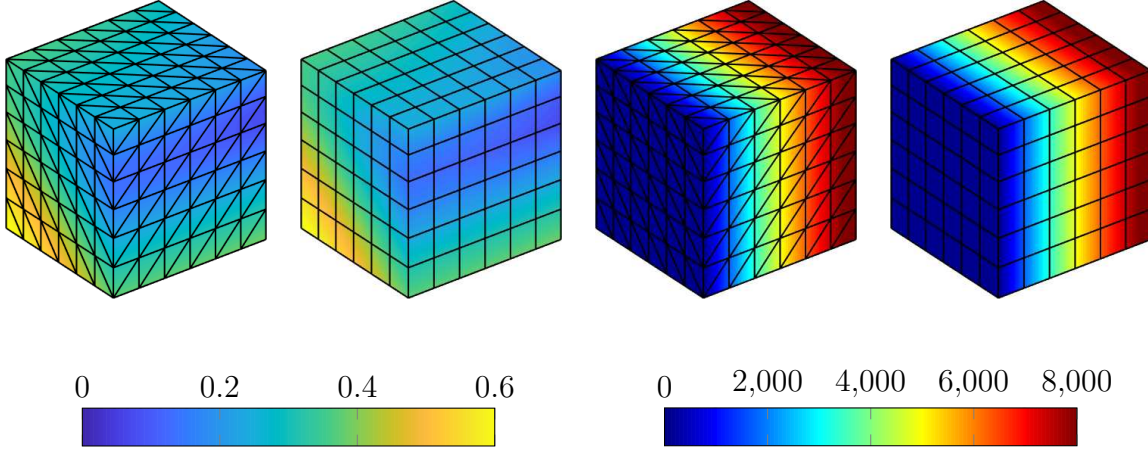

$$
\begin{array}{cccc}
0 & 0.2 & 0.4 & 0.6
\end{array}
\qquad
\begin{array}{ccccc}
0 & 2{,}000 & 4{,}000 & 6{,}000 & 8{,}000
\end{array}
$$

Figure 6: Static convergence analysis: Von Mises stress (left) and electrical potential distribution (right) for *tet 10/4* and *hex 20/8* meshes, respectively.

As expected $p + 1$ convergence is observed in all variables for the tetrahedral elements, since the convergence is optimal for this element (see Fig. 7). For the primary fields $\boldsymbol{\phi}$ and φ the convergence observed for the *hex 20/8* elements is even slightly better.
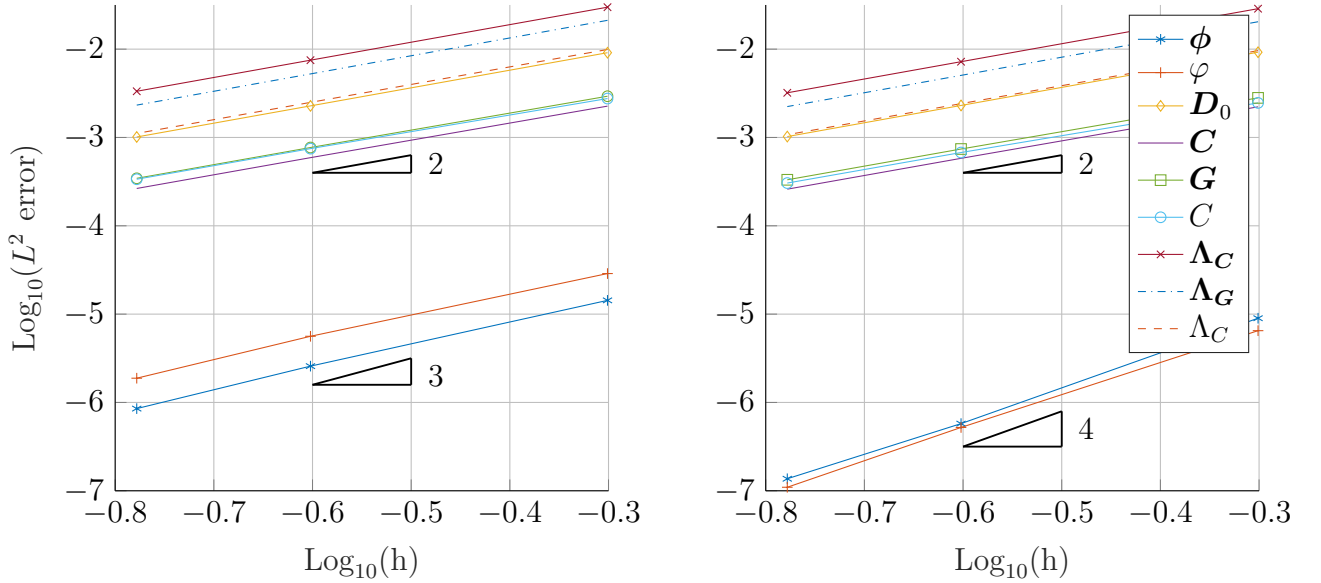
Figure 7: Spatial convergence analysis for *tet 10/4* (left) and *hex 20/8* (right) meshes.

7.3. Static Cook's membrane test

The objectives of the following two examples are:

O3.I To show the convergence behaviour for a nearly incompressible material model in different loading scenarios (cf. [8]).

O3.II To compare the numerical robustness of the 9-field formulation proposed against the 3-field formulation presented in [34] which is based on the three fields $\{\boldsymbol{\phi}, \varphi, \boldsymbol{D}_0\}$.

The well-known Cook's membrane problem is considered in what follows under two different settings. First, an isotropic model with mechanical loading is presented followed by a mechanical anisotropic model with electrical loading.

7.3.1. Cooks membrane test 1: Isotropic model with mechanical loading

The geometry of the Cook's membrane, material and simulation parameters are provided in Tab. 3. The material parameters $\{\mu_1, \mu_2, \lambda\}$ for the Mooney-Rivlin model in equation (58) can be related to the Young's modulus E and the Poisson's ratio ν in the origin as

$$E = 3\,\mu_1 \frac{18\,\mu_1 + 6\,\lambda}{7\,\mu_1 + 2\,\lambda}; \quad \nu = \frac{4\,\mu_1 + 2\,\lambda}{14\,\mu_1 + 4\,\lambda}, \tag{64}$$

where for convenience $\mu_2 = 2\,\mu_1$. In this specific example $E = 8.9888 \times 10^5 \ Pa$ and $\nu = 0.4981$. The membrane is fixed in space at face $x_1 = 0$ (see Fig. 8). A pressure load $p\,\boldsymbol{e}_3$ with magnitude $p = 20.000$Pa is applied at face $x_1 = 48$ (see Fig. 8). Homogeneous electrical Neumann boundary conditions are considered for all the boundaries. For this example, a series of progressively refined *tet 10/4* meshes is considered (see Fig. 9). A representation of the deformed configuration is shown in Fig. 8. For the convergence study the displacement of node $\boldsymbol{X} = (48, 60, 0)$ into $\boldsymbol{e}_3$-direction is investigated with respect to the number of degrees of freedom (DOFs). The results are depicted in Fig. 9, where the proposed 9-field formulation is compared against the 3-field formulation presented in [34]. As can be observed, the 9-field formulation performs better than the 3-field formulation especially in coarse mesh scenarios. In addition, fewer Newton iterations are required by the 9-field formulation, allowing the use of larger loading steps. Overall, the 9-field formulation exhibits superior numerical performance when compared to the 3-field formulation.
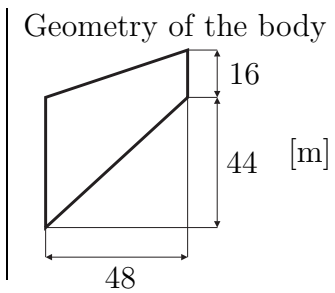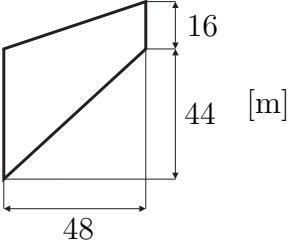
Mechanical parameters	μ_1	1×10^5	Pa	Geometry of the body
	μ_2	2×10^5	Pa	
	λ	4×10^7	Pa	
Electrical parameters	ϵ_0	8.854×10^{-12}	$A^2\,s^4\,kg^{-1}\,m^{-3}$	
	ϵ_r	4	N/V^2	
Ref. potential	φ_0	0	V	
Newton tolerance	ϵ	10^{-4}	J	

Table 3: Cook's membrane test 1: Material parameters, simulation parameters and geometry.
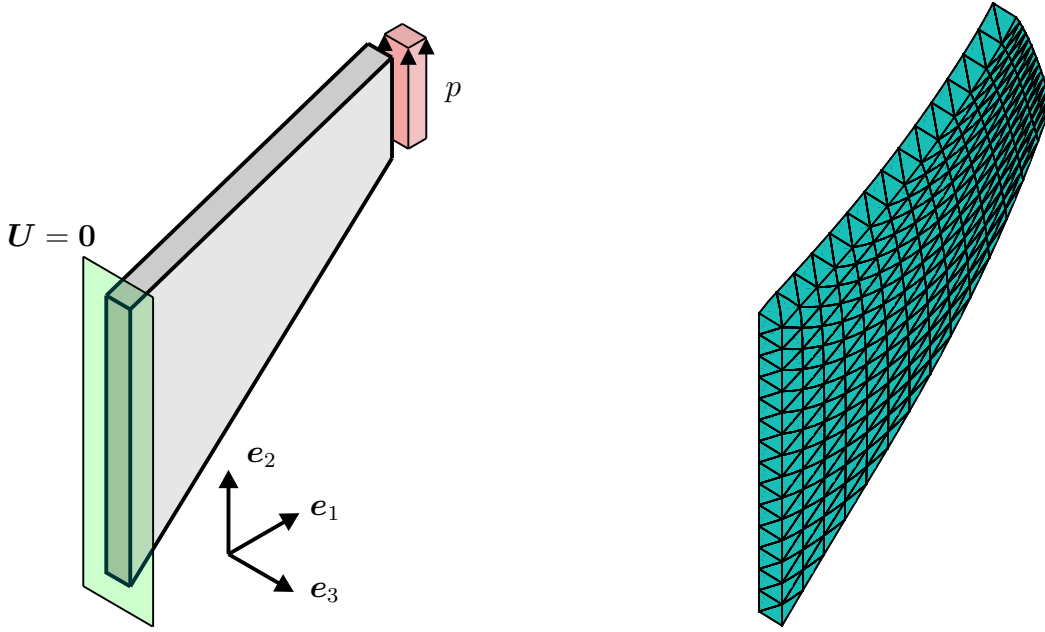
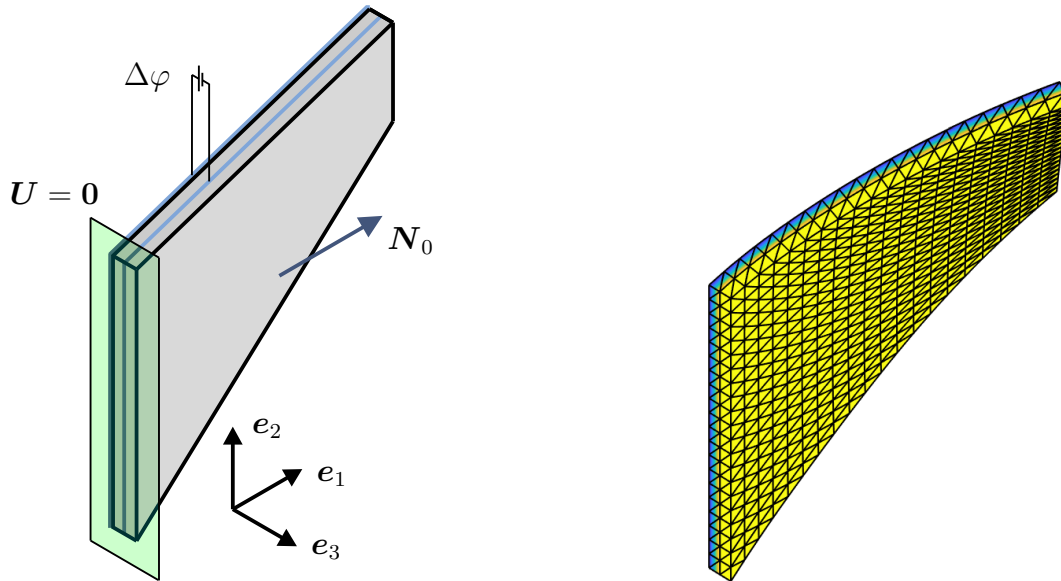Figure 8: Cook's membrane test 1: Geometry and boundary conditions (left) and typical mesh in current configuration (right).
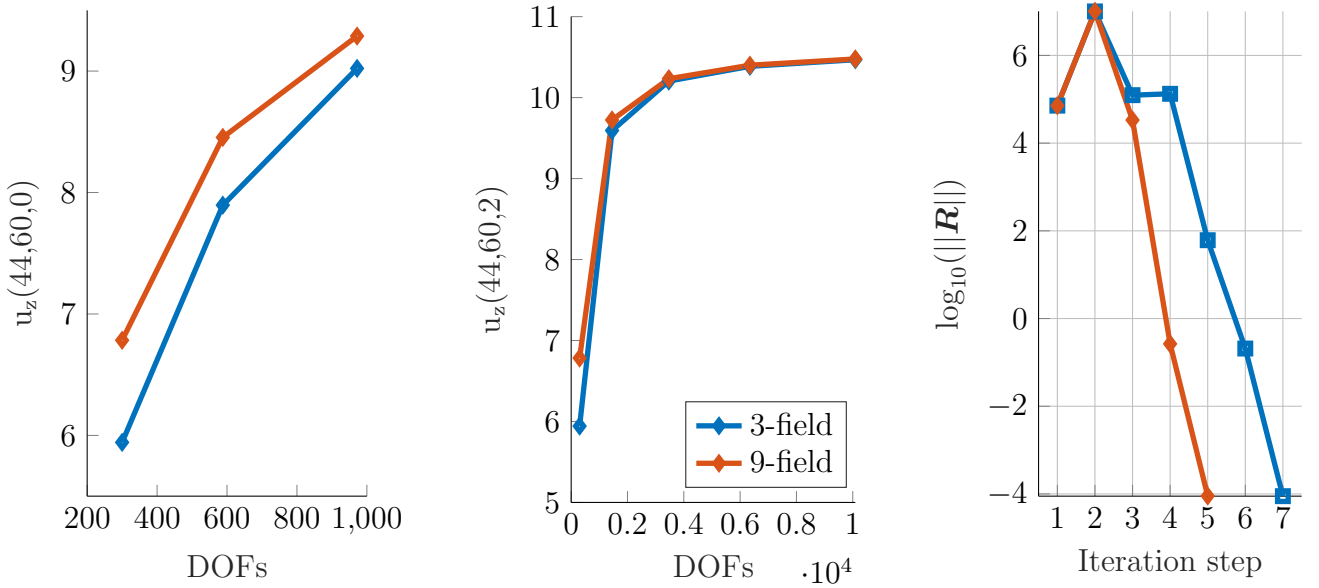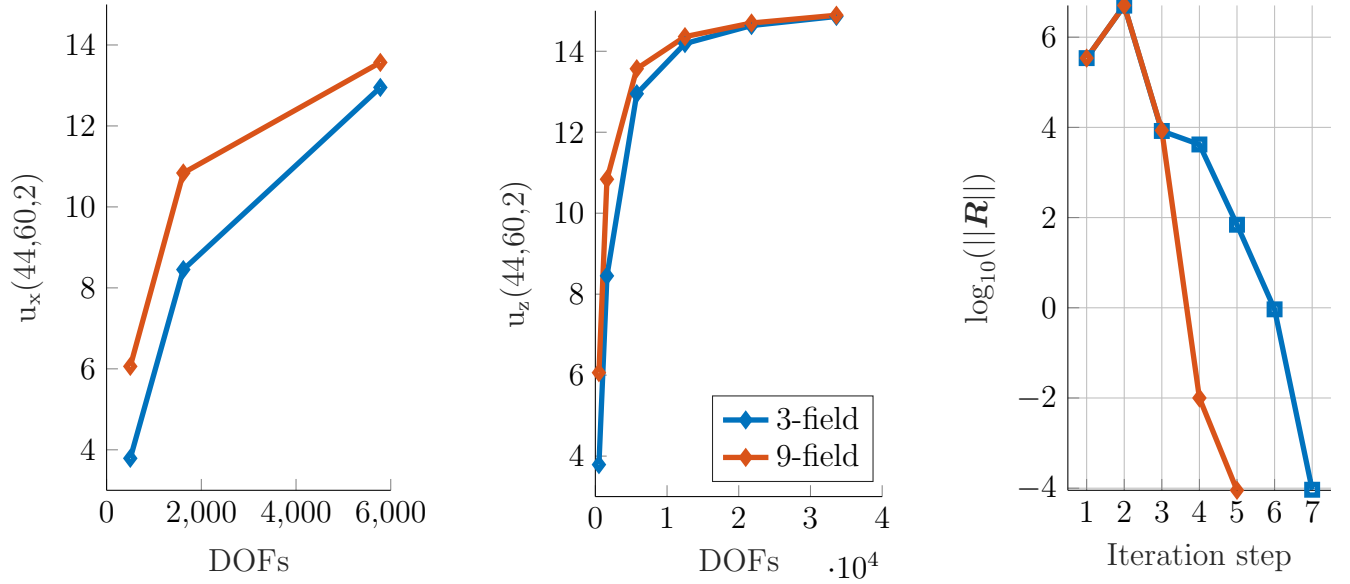

Figure 9: Cook's membrane test 1 using the proposed 9-field formulation and the 3-field formulation in [34]: Convergence plot for a selection of coarse meshes (left), a complete set of progressively refined meshes (centre) and typical Newton iteration convergence (right).

7.3.2. Cook's membrane test 2: Transversally isotropic model with electrical loading

In this example we consider the transversely isotropic energy functional in equation (59). Now electrical loading is applied. The geometry of the Cook's membrane, material and simulation parameters are displayed in Tab. 4. A fibre reinforcement with direction $\boldsymbol{N}_0 = [1\ 0\ 0]^{\mathrm{T}}$ is employed. The boundary conditions and a typical mesh in the current configuration are shown in Fig. 10. The electrical Dirichlet boundary conditions are given by

$$\Phi(X_1 = 0, X_2, X_3) = 0\,\mathrm{V}; \quad \Phi(X_1 = 2, X_2, X_3) = 7 \times 10^7\,\mathrm{V}. \tag{65}$$

22

By employing the above potentials the membrane starts to bend into the positive e_3-direction but its performance is also influenced by the fibre direction. For this example a series of progressively refined *tet 10/4* meshes are considered (see Fig. 11). For the spatial convergence study the displacement of node $X = (48, 60, 2)$ into e_1-direction is investigated with respect to the number of DOFs. The results are depicted in Fig. 11. Overall, the 9-field formulation exhibits superior numerical performance when compared to the 3-field formulation.

Mechanical parameters	μ_1	5×10^4	Pa	Geometry of the body
	μ_2	1×10^5	Pa	
	λ	4×10^7	Pa	
Anisotropic parameters	g_0	3×10^3	Pa	
	$g_{\mathbf{C}}$	4		
	$g_{\mathbf{G}}$	8		
	g_C	1		
Electrical parameters	ϵ_0	8.854×10^{-12}	$\mathrm{A^2\,s^4\,kg^{-1}\,m^{-3}}$	
	ϵ_r	4	$\mathrm{N/V^2}$	
Ref. potential	φ_0	0	V	
Newton tolerance	ϵ	10^{-4}	-	

Table 4: Cook's membrane test 2: Material parameters, simulation parameters and geometry.

Figure 10: Cook's membrane test 2: Geometry and boundary conditions (left) and typical mesh in current configuration (right).

Figure 11: Cook's membrane test 2 using the proposed 9-field formulation and the 3-field formulation in [34]: Convergence plot for a selection of coarse meshes (left), a complete set of progressively refined meshes (centre) and typical Newton iteration convergence (right).

7.4. Dynamic analysis of a shell-like actuator

The objectives of this example are:

O4.I To assess the conservation properties of the time integration scheme presented in (30), (32) and (33) for the *tet 10/4* finite element. In particular, the conservation properties of the proposed EM time integration scheme will be analysed.

O4.II To compare the stability and robustness of the proposed EM time integration scheme against the midpoint-rule integrator.

Mechanical parameters	μ_1	5×10^4	Pa	Geometry of the actuator
	μ_2	1×10^5	Pa	
	λ	1×10^5	Pa	
Electrical parameters	ϵ_0	8.854×10^{-12}	$A^2\, s^4\, kg^{-1}\, m^{-3}$	
	ϵ_r	4	N/V^2	
Ref. potential	φ_0	0	V	
Max. surface charge	ω_0	7.5×10^{-4}	Q/m^2	
Density	ρ_0	1000	$kg\, m^{-3}$	
Timestep size	Δt	0.1	s	
Simulation time	T	20	s	
Newton tolerance	ϵ	10^{-6}	-	[m]

Table 5: Shell-like actuator: Material parameters, simulation parameters and geometry. Length in $\boldsymbol{e}_3$ direction of the actuator is $2.5m$, the four holes are placed at $0.8333m$ and $1.6666m$ in $\boldsymbol{e}_3$ direction.

24
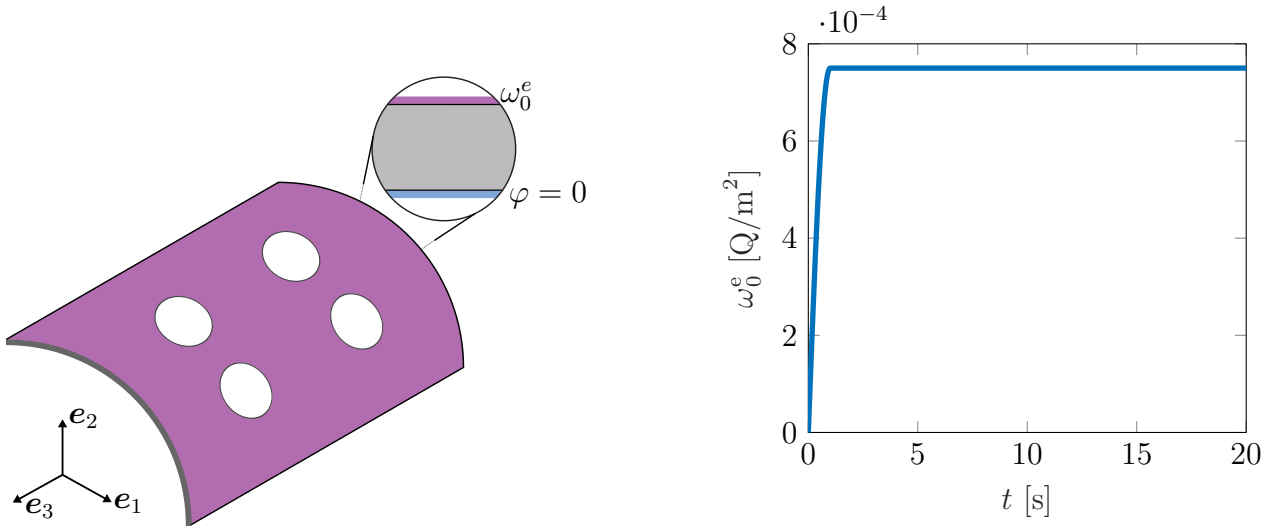
Figure 12: Shell-like actuator: Electrical boundary conditions are shown (left) and the mechanical Dirichlet boundary conditions are as follows: $U_1(X_1, X_2 = 0, X_3) = 0$, $U_2(X_1 = 0, X_2, X_3) = 0$ and $\boldsymbol{U}(X_1 = 1, X_2 = 0, X_3) = \boldsymbol{0}$. Applied surface electric charge ω_0^e corresponding to (66) is shown (right).

A shell like actuator perforated with four holes is investigated next. The geometry, boundary conditions, material and simulation parameters are provided in Tab. 5 and Fig. 12 and are chosen similar to those of the example given in [42, Sect. 4.6.1.]. A constant value for the electric potential of $\varphi = 0\,V$ is applied on the blue electrode, whereas a surface electric charge ω_0^e, with

$$\omega_0^e = \left(7.5 \times 10^{-4}\right) \times \begin{cases} \sin\left(\frac{0.5\,\pi}{1\,\text{s}}\,t\right) & \text{for } t \leq 1\,\text{s} \\ 1 & \text{for } t > 1\,\text{s} \end{cases} \quad [Q/m^2]. \tag{66}$$

is applied on the purple electrode (see Fig. 12). A mesh comprised of 6090 *tet 10/4* elements with a total of 50384 displacement and electrical potential unknowns (see Fig. 12) is employed. Fig. 13 shows typical snapshots of the deformation of the actuator together with the electric potential distribution, Fig. 14 shows the von Mises stress distribution and Fig. 15 shows the first component of the electrical displacement $\boldsymbol{D}_0$. Fig. 16 shows that the midpoint-rule time integrator exhibits an energy blow-up and becomes unstable approximately in the interval $6.2 < t < 6.4$. In contrast, the newly proposed EM time integrator conserves the total energy after the loading phase and remains stable for the whole simulation for the same fixed time step size of $\Delta t = 0.1\,s$. Accordingly, the proposed scheme is more robust and stable than the midpoint-rule.

7.5. Dynamic analysis of H-shaped actuator

The objectives of this example are:

O5.I To verify the conservation of angular momentum by the time integrator proposed.

O5.II To compare the conservation properties and robustness of the proposed time integrator to those of the midpoint-rule time integrator.
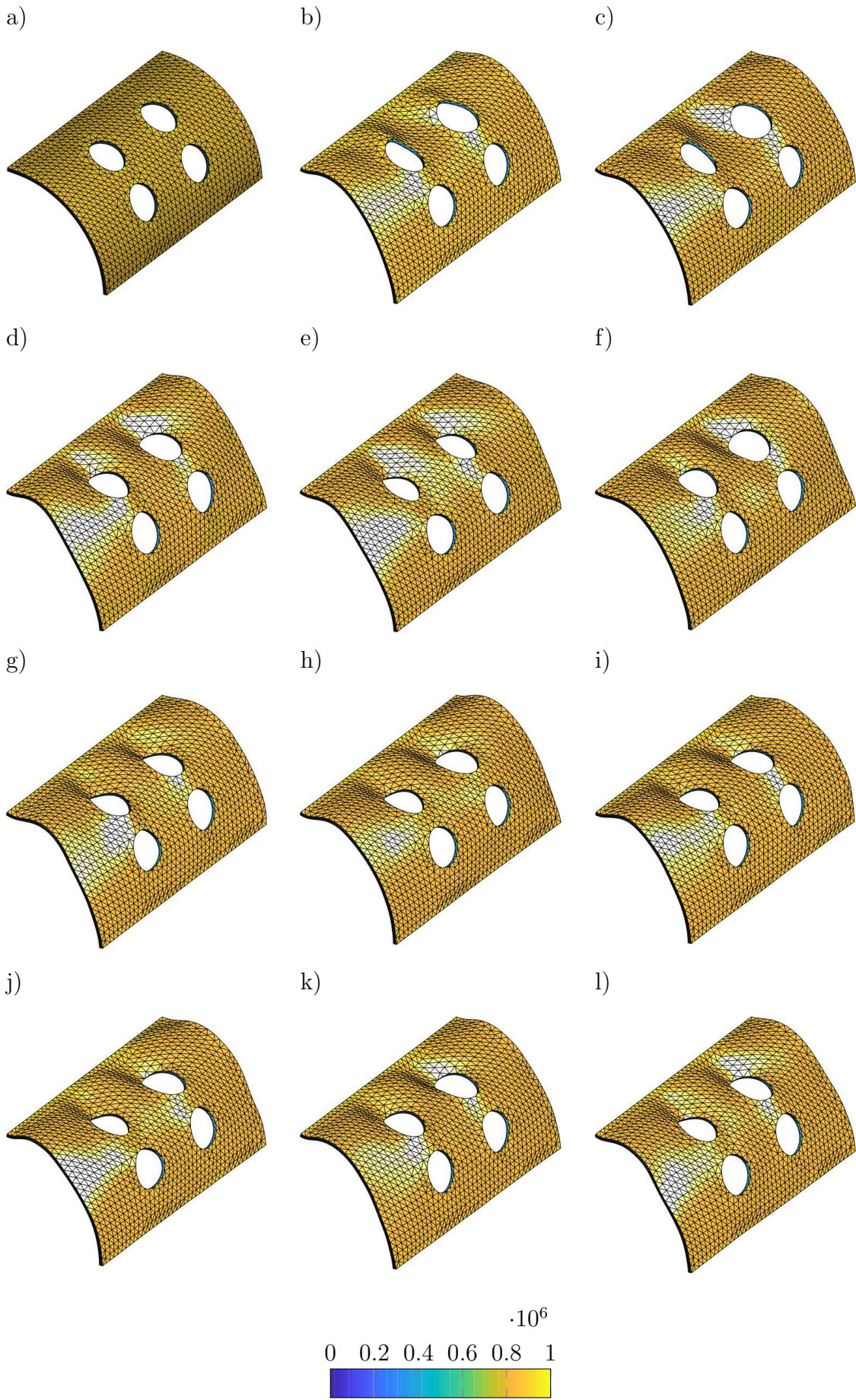
Figure 13: Shell-like actuator: Snapshots of electric potential φ for different configurations corresponding to (left to right-top to bottom): (a) $t = 0\,s$; (b) $t = 0.8\,s$; (c) $t = 1.6\,s$; (d) $t = 2.4\,s$; (e) $t = 3.2\,s$; (f) $t = 4.0\,s$; (g) $t = 4.8\,s$; (h) $t = 5.6\,s$; (i) $t = 6.4\,s$; (j) $t = 7.2\,s$; (k) $t = 8\,s$; (l) $t = 8.8\,s$.
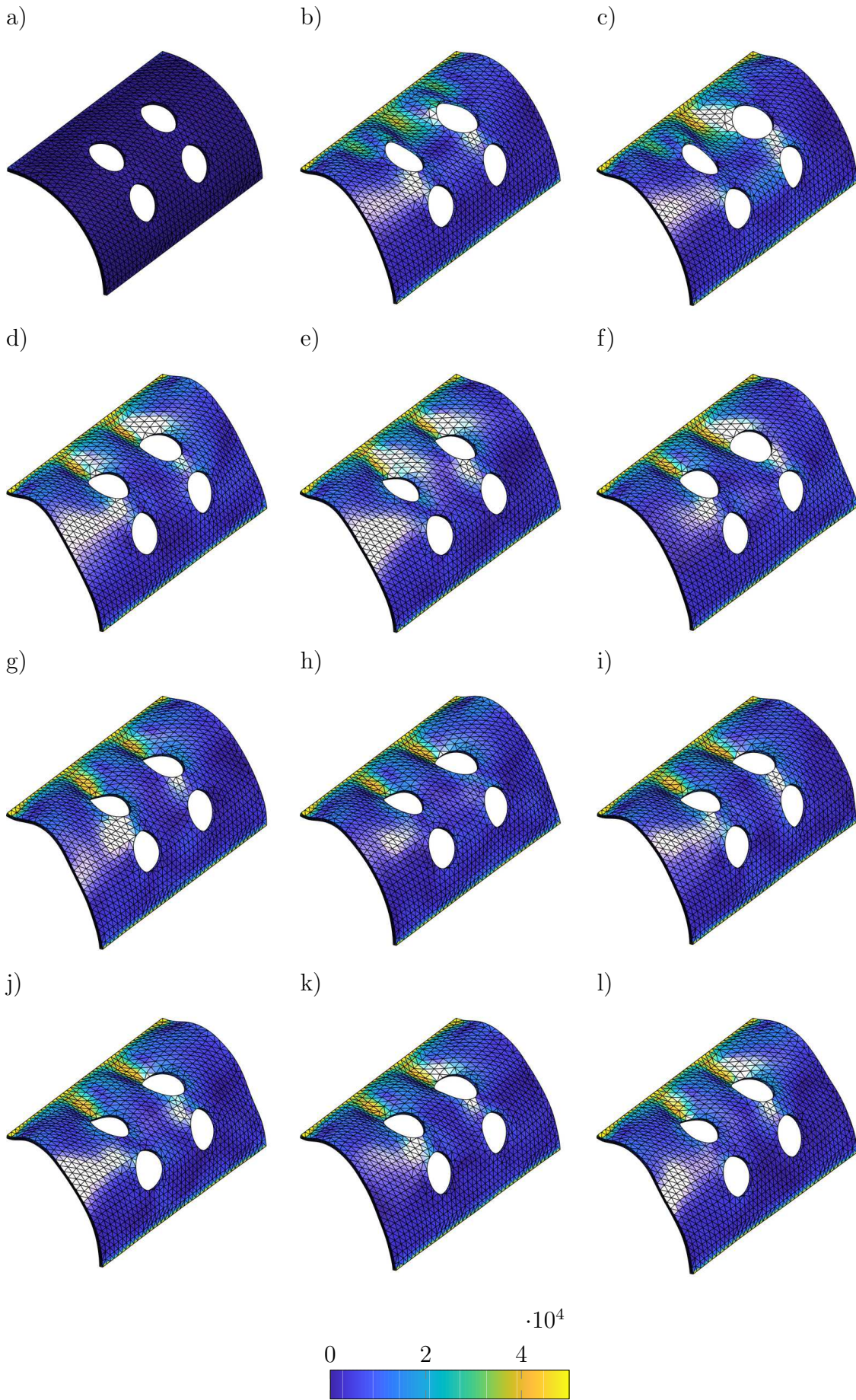
Figure 14: Shell-like actuator: Snapshots of von Mises stress for different configurations corresponding to (left to right-top to bottom): (a) $t = 0\,s$; (b) $t = 0.8\,s$; (c) $t = 1.6\,s$; (d) $t = 2.4\,s$; (e) $t = 3.2\,s$; (f) $t = 4.0\,s$; (g) $t = 4.8\,s$; (h) $t = 5.6\,s$; (i) $t = 6.4\,s$; (j) $t = 7.2\,s$; (k) $t = 8\,s$; (l) $t = 8.8\,s$.
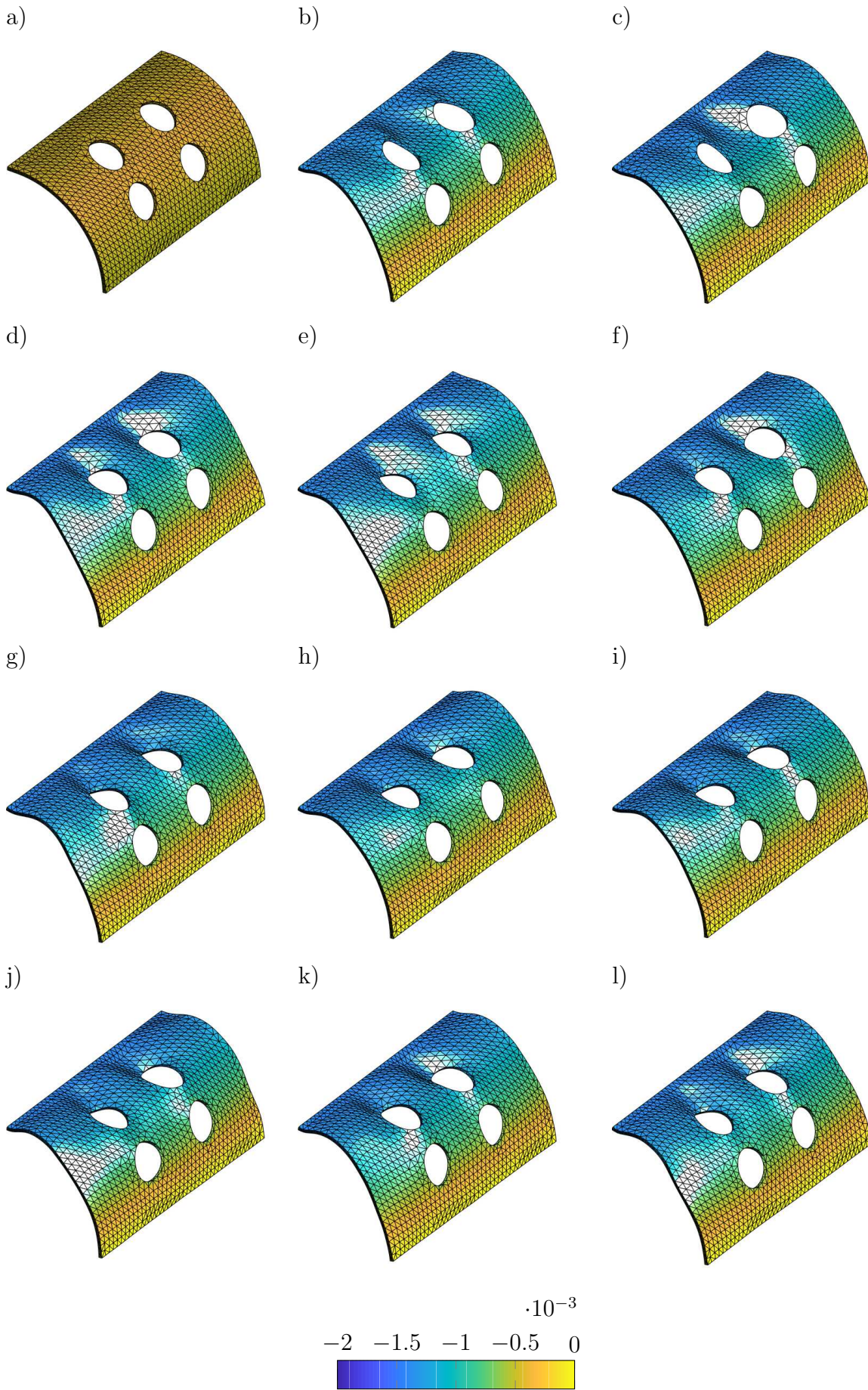
Figure 15: Shell-like actuator: Snapshots of first component of $\boldsymbol{D}_0$ for different configurations corresponding to (left to right-top to bottom): (a) $t = 0\,s$; (b) $t = 0.8\,s$; (c) $t = 1.6\,s$; (d) $t = 2.4\,s$; (e) $t = 3.2\,s$; (f) $t = 4.0\,s$; (g) $t = 4.8\,s$; (h) $t = 5.6\,s$; (i) $t = 6.4\,s$; (j) $t = 7.2\,s$; (k) $t = 8\,s$; (l) $t = 8.8\,s$.
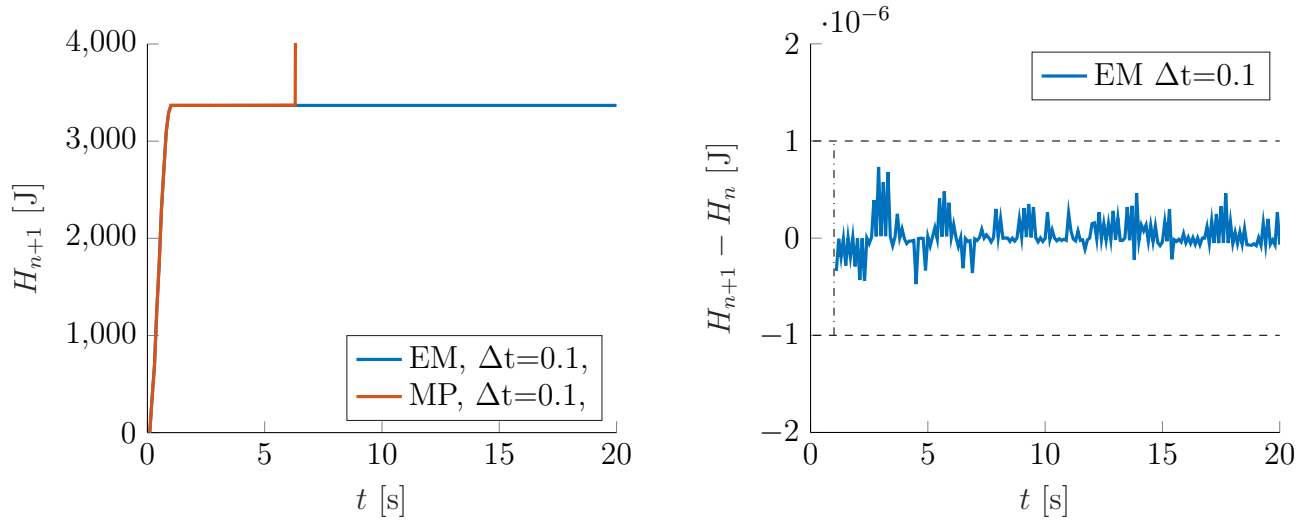
Figure 16: Shell-like actuator: Energy evolution for the proposed EM scheme. Left: Time evolution of $\mathcal{H}_{\widetilde{W}}$ for proposed scheme. Right: Time evolution of $\Delta\mathcal{H}_{\widetilde{W}}$ in the time interval $[1, 10]$.

Mechanical parameters	μ_1	5×10^4	Pa	Geometry of the H-shaped actuator
	μ_2	1×10^5	Pa	
	λ	5×10^5	Pa	
Electrical parameters	ϵ_0	8.854×10^{-12}	$A^2\,s^4\,kg^{-1}\,m^{-3}$	
	ϵ_r	4	N/V^2	
Ref. potential	φ_0	0	V	
Max. surface charge	ω_0	5×10^{-3}	Q/m^2	
Density	ρ_0	1000	$kg\,m^{-3}$	
Timestep size	Δt	0.05	s	
Simulation time	T	10	s	
Newton tolerance	ϵ	10^{-5}	-	

Table 6: H-shaped actuator: Material parameters, simulation parameters and geometry.
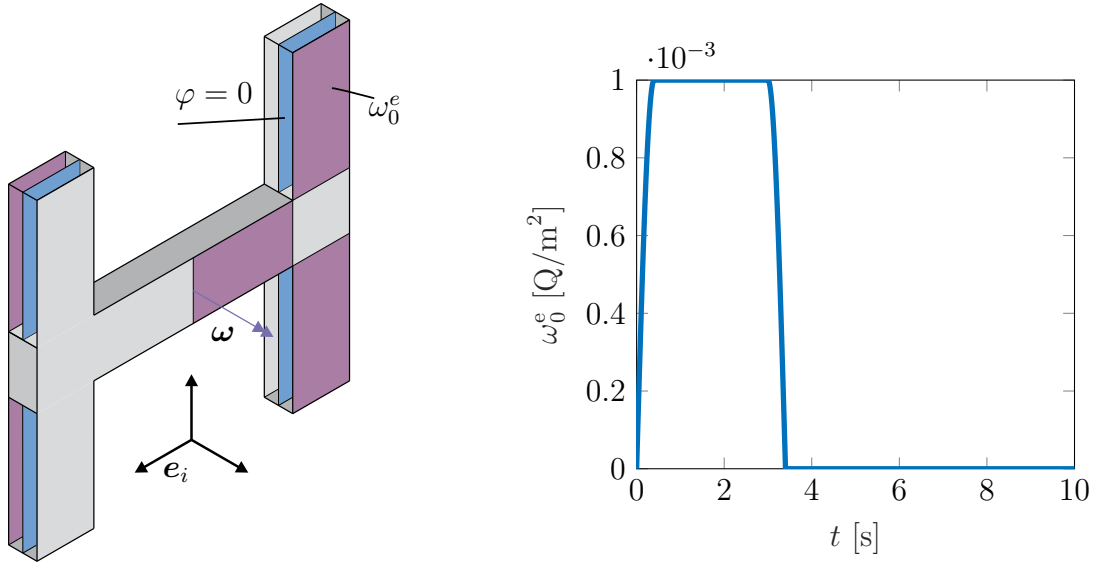
Figure 17: H-shaped actuator: Boundary conditions (left) and applied surface electric charge ω_0^e (right) corresponding to (68).

The geometry, boundary conditions, material and simulation parameters of an H-shaped actuator are depicted in Tab. 6 and Fig. 17. Note that this example is inspired by numerical example 3 in [34]. A mesh comprised of 15013 *tet 10/4* elements with a total of 95776 displacement and electrical potential unknowns (see Fig. 17) is employed. From a mechanically point of view the actuator is free in space, i.e. no mechanical Dirichlet conditions are imposed. An initial velocity $\boldsymbol{v}_0$ is prescribed and given by

$$\boldsymbol{v}_0 = \boldsymbol{\omega} \times \boldsymbol{X}; \qquad \boldsymbol{\omega} = [0, 0, 0.05]^T \, s^{-1}; \qquad \boldsymbol{X} = [X_1, X_2, X_3]^T, \tag{67}$$

with $\{X_1, X_2, X_3\}$ aligned with the orthonormal basis $\{\boldsymbol{e}_1, \boldsymbol{e}_2, \boldsymbol{e}_3\}$, respectively (see Figure 17). A constant value for the electric potential of $\varphi = 0 \, V$ is applied on the blue electrode. A surface electric charge ω_0^e, with

$$\omega_0^e = \left(1 \times 10^{-3}\right) \times \begin{cases} \sin(\frac{0.5\,\pi}{0.4\,s}\,t) & \text{for } t \leq 0.4\,s \\ 1 & \text{for } 0.4\,s < t \leq 3.0\,s \\ \cos(\frac{0.5\,\pi}{3.4\,s - 3.0\,s}\,(t - 3\,s)) & \text{for } 3.0\,s < t \leq 3.4\,s \\ 0 & \text{for } t > 3.4\,s \end{cases} \quad [Q/m^2]. \tag{68}$$

is applied (see Fig. 17) on the purple electrode (see detailed view in Fig. 17). Fig. 18, 19 and 20 show typical snapshots of the H-shaped actuator displaying the electric potential φ, von Mises stress σ_{vM} and third component of electrical displacement $\boldsymbol{D}_0$, respectively, where extremely large deformations can be observed. Results are smooth and do not show any spurious pressure or electric field. Fig. 21 shows the energy evolution and Fig. 22 the evolution of the norm of the total angular momentum $\boldsymbol{J}$ of the actuator for the proposed EM time integrator and the midpoint-rule. In addition, Fig. 21 shows that the midpoint-rule time integrator exhibits an energy blow-up and becomes unstable approximately in the interval $0.4\,s < t < 1.8\,s$. In contrast, the newly proposed EM time integrator perfectly conserves the energy after the loading phase. Also the discrete balance of angular momentum is perfectly preserved. The EM time integrator remains stable for the entire simulation time for the same fixed time step size of $\Delta t = 0.05\,s$. Accordingly, the proposed scheme is more robust and stable than the midpoint-rule.
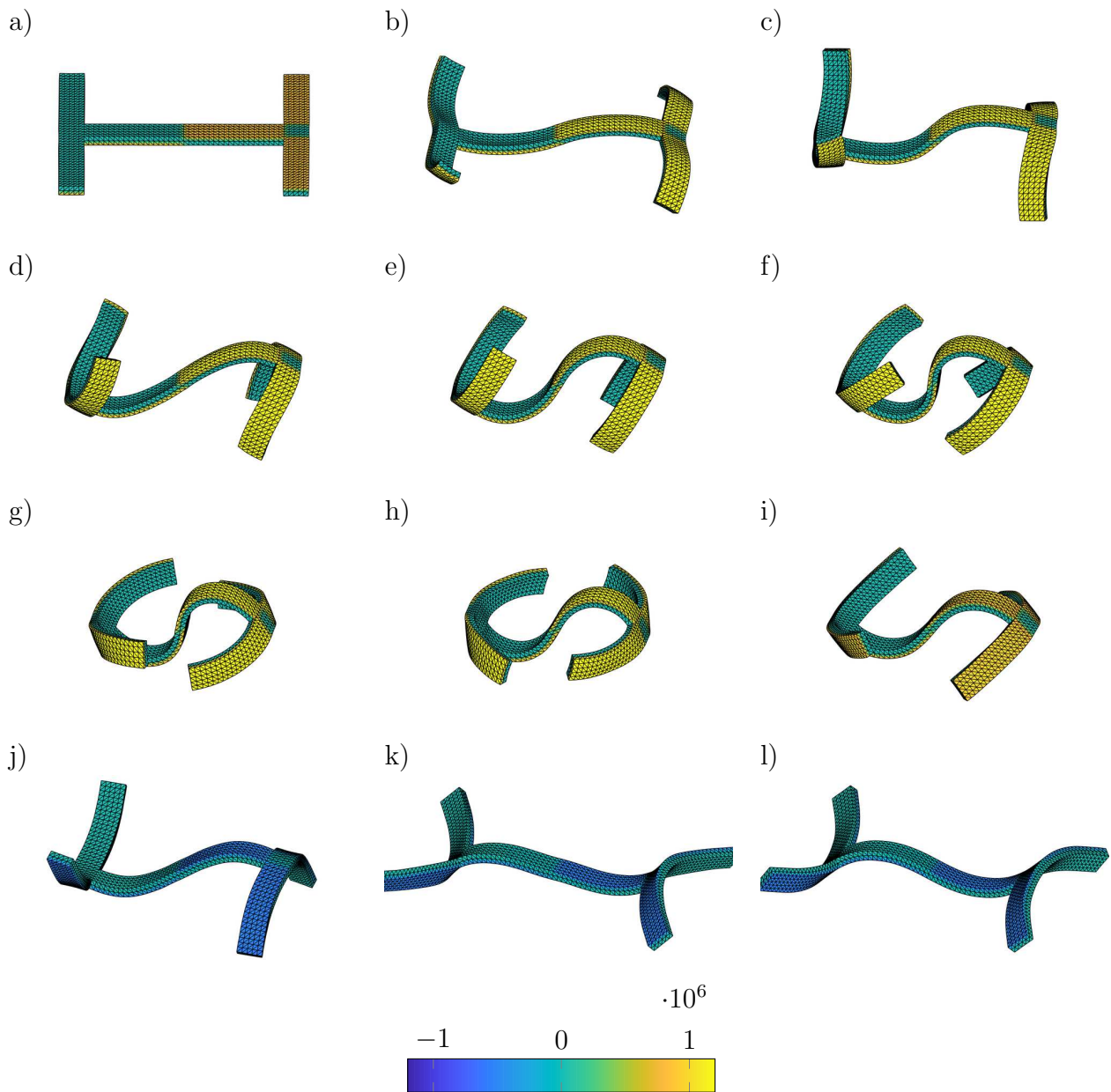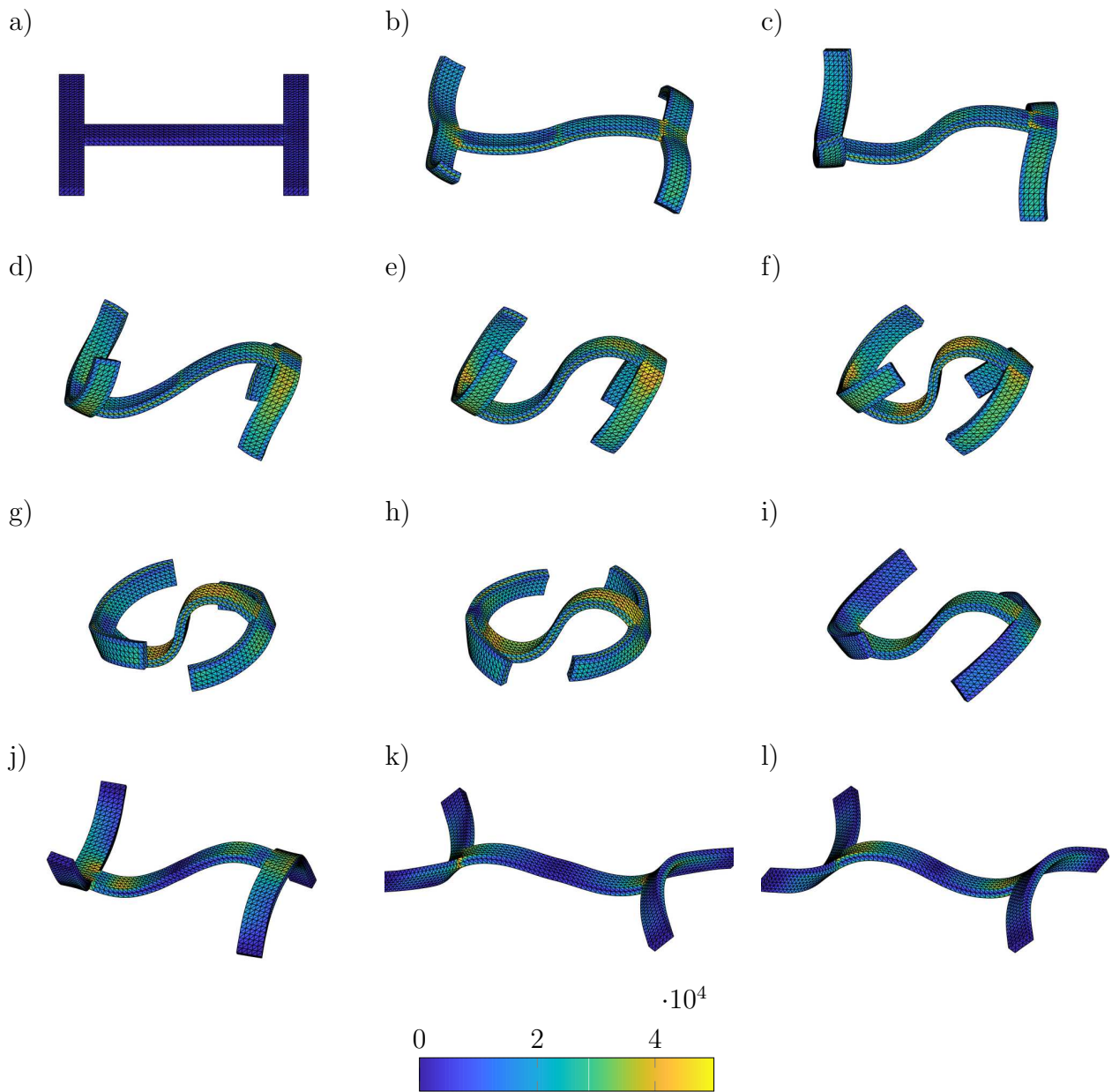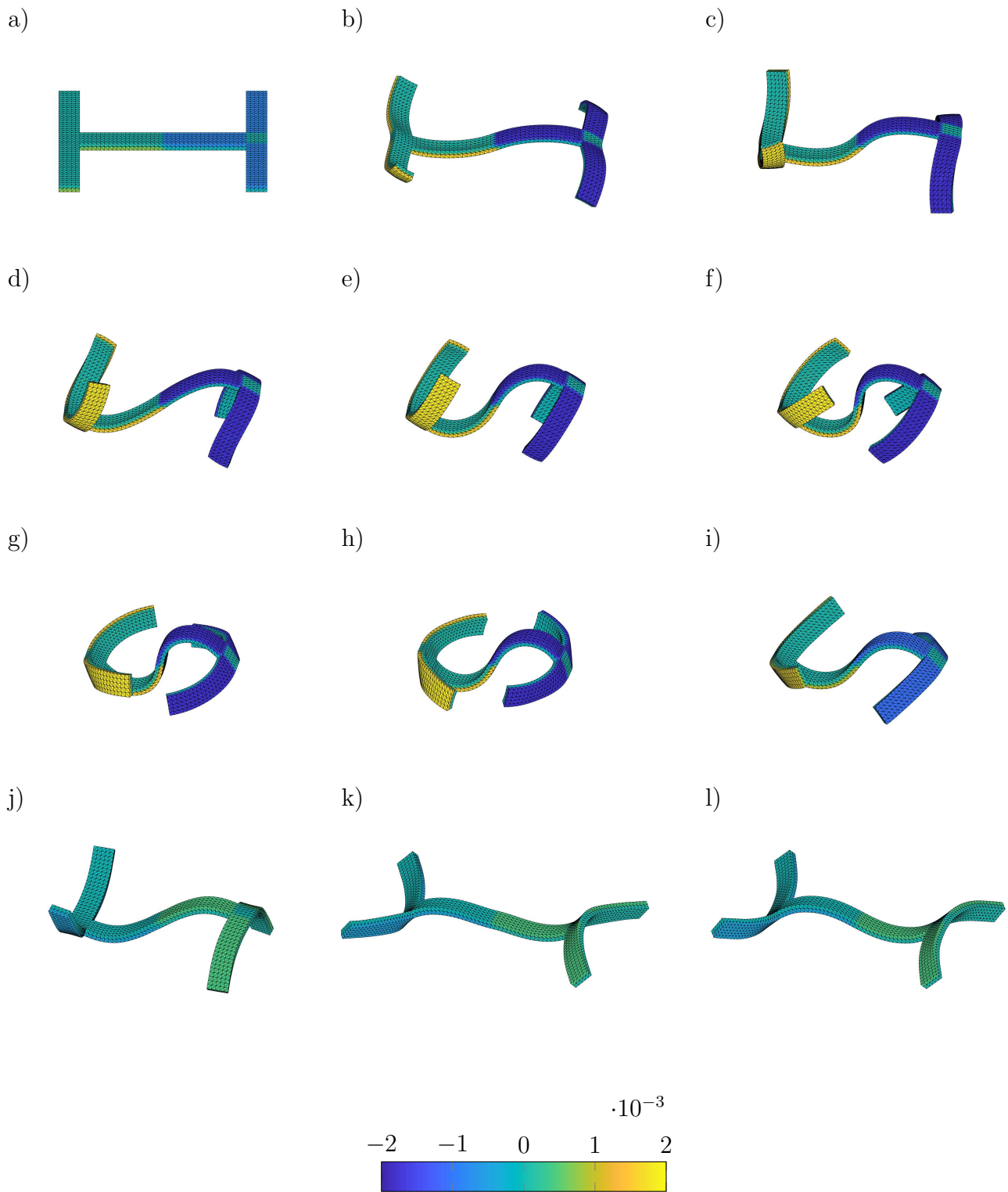
30

Figure 18: H-shaped actuator: Snapshots of electric potential φ for different configurations corresponding to (left to right-top to bottom): (a) $t = 0\,s$; (b) $t = 0.4\,s$; (c) $t = 0.8\,s$; (d) $t = 1.2\,s$; (e) $t = 1.6\,s$; (f) $t = 2\,s$; (g) $t = 2.4\,s$; (h) $t = 2.8\,s$; (i) $t = 3.2\,s$; (j) $t = 3.6\,s$; (k) $t = 4\,s$; (l) $t = 4.4\,s$.

Figure 19: H-shaped actuator: Snapshots of the von Mises stress σ_{vM} for different configurations corresponding to (left to right-top to bottom): (a) $t = 0\,s$; (b) $t = 0.4\,s$; (c) $t = 0.8\,s$; (d) $t = 1.2\,s$; (e) $t = 1.6\,s$; (f) $t = 2\,s$; (g) $t = 2.4\,s$; (h) $t = 2.8\,s$; (i) $t = 3.2\,s$; (j) $t = 3.6\,s$; (k) $t = 4\,s$; (l) $t = 4.4\,s$.

Figure 20: H-shaped actuator: Snapshots of third component of $\boldsymbol{D}_0$ for different configurations corresponding to (left to right-top to bottom): (a) $t = 0\,s$; (b) $t = 0.4\,s$; (c) $t = 0.8\,s$; (d) $t = 1.2\,s$; (e) $t = 1.6\,s$; (f) $t = 2\,s$; (g) $t = 2.4\,s$; (h) $t = 2.8\,s$; (i) $t = 3.2\,s$; (j) $t = 3.6\,s$; (k) $t = 4\,s$; (l) $t = 4.4\,s$.
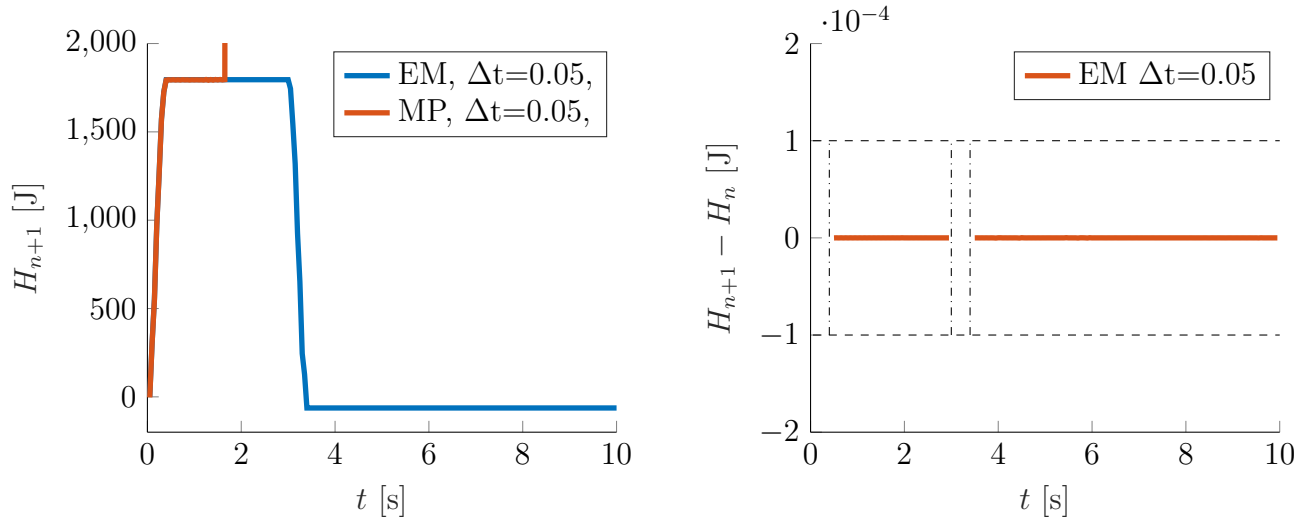
Figure 21: H-shaped actuator: Energy evolution for the proposed EM scheme. Left: Time evolution of $\mathcal{H}_{\widetilde{W}}$ with the proposed scheme. Right: Time evolution of $\Delta\mathcal{H}_{\widetilde{W}}$ in the time interval $[0.4, 3] \bigcup [3.4, 10]$.
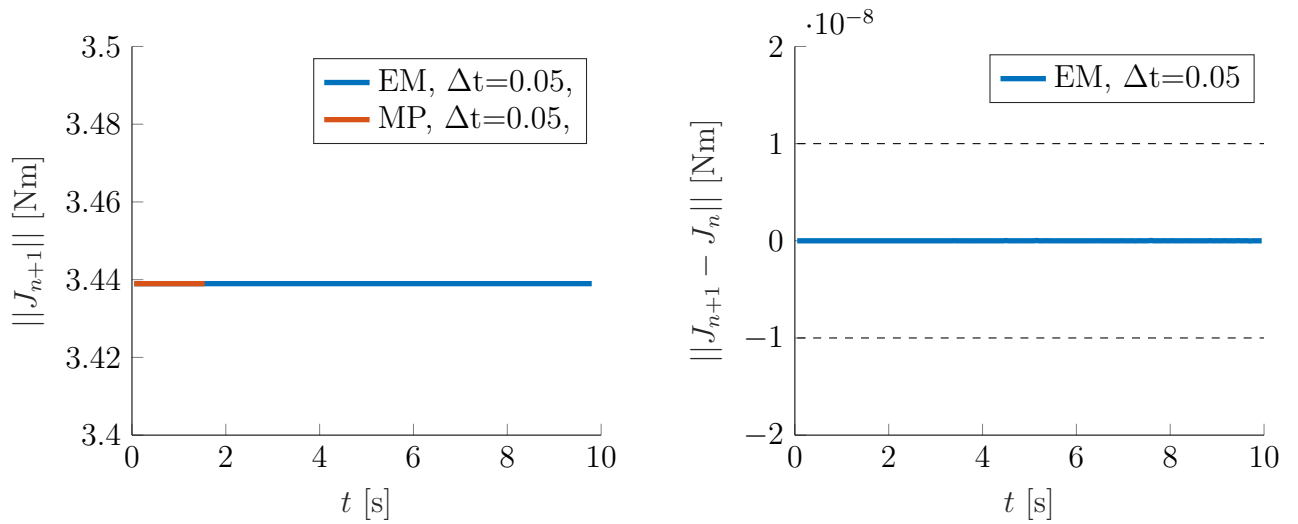
Figure 22: H-shaped actuator: Time evolution of the magnitude of the angular momentum $||\boldsymbol{J}||$ (left) with proposed EM scheme and midpoint-rule. Time evolution of $\Delta||\boldsymbol{J}||$ (right).

7.6. Dynamic contractions of an artificial muscle model

The objective of this example is:

O6.I The consideration of more sophisticated constitutive models allowing for the inclusion of anisotropic effects. A comparison of the stability and robustness between the proposed EM time integrator and the midpoint-rule integrator will also be carried out in this example.
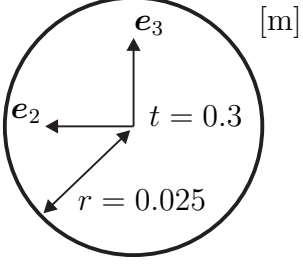
				Geometry of the body
Mechanical parameters	μ_1	5×10^4	Pa	
	μ_2	1×10^5	Pa	
	λ	1×10^6	Pa	
Anisotropic parameters	g_0	$3 \cdot 10^3$	Pa	
	$g_\mathbf{C}$	4		
	$g_\mathbf{G}$	8		
	g_C	1		
Electrical parameters	ϵ_0	8.854×10^{-12}	$\mathrm{A^2\,s^4\,kg^{-1}\,m^{-3}}$	
	ϵ_r	4	$\mathrm{N/V^2}$	
Ref. potential	φ_0	0	V	
Density	ρ_0	1	$\mathrm{kg\,m^{-3}}$	
Timestep size	Δt	0.1	s	
Simulation time	T	7	s	
Newton tolerance	ϵ	10^{-3}	-	

Table 7: Artificial muscle model: Material parameters, simulation parameters and geometry of an .
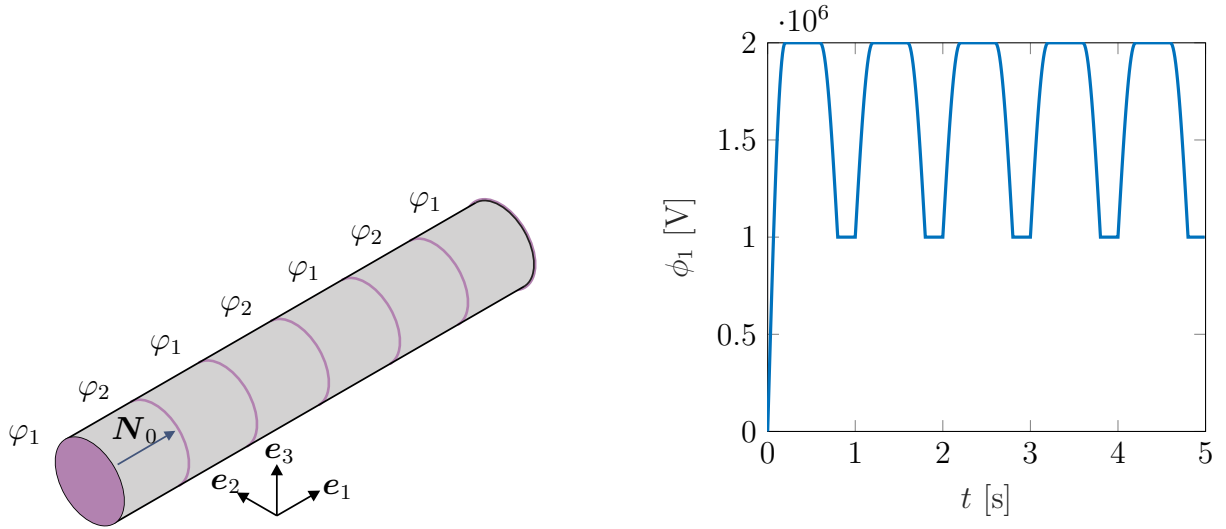
Figure 23: Artificial muscle model: Boundary conditions (left) and electric potential φ_1 (right) corresponding to (69).

A technical realization of EAPs are artificial muscles which will be modelled in the following. The geometry of the muscle model is depicted in Fig. 23 and is similar to an example given in [44]. The material parameters are given in Tab. 7. Boundary conditions are depicted in Fig. 23. A mesh comprised of 5790 *tet 10/4* elements with a total of 35076 displacement and electrical potential unknowns (see Fig. 24) is employed. The example contains multiple electrodes perpendicular to

the muscle's longitudinal axis with alternating signs. These electrodes dictate a particular electric potential, e.g. via electric voltages for

$$\varphi_1 = \bar{\varphi} + \widetilde{\varphi} \cdot \begin{cases} \sin(0.5\,\pi\,(t/t_k^1)) & \forall\, t \in [t_k^0, t_k^1) \\ 1 & \forall\, t \in [t_k^1, t_k^2) \\ \cos(0.5\,\pi\,(t - t_k^2)/0.2s) & \forall\, t \in [t_k^2, t_k^3) \\ 0 & \forall\, t \in [t_k^3, t_{k+1}^0) \end{cases} \quad [MV], \tag{69}$$

where

$$\bar{\varphi} = \begin{cases} 0 & \forall\, t \in [t_1^0, t_1^1) \\ 1 & \forall\, t \in [t_1^1, t_{n_{zyk}+1}^0] \end{cases} \quad [MV] \tag{70}$$

and

$$\widetilde{\varphi} = \begin{cases} 2 & \forall\, t \in [t_1^0, t_1^1) \\ 1 & \forall\, t \in [t_1^1, t_{n_{zyk}+1}^0] \end{cases} \quad [MV]. \tag{71}$$

Here, $t_k^0 = (k-1) \cdot 1s$, $t_k^1 = t_k^0 + 0.2s$, $t_k^2 = t_k^0 + 0.6s$, $t_k^3 = t_k^0 + 0.8s$ and $k \in \mathbb{Z}_{>0} = \{1, 2, ..., n_{zyk}\}$, where n_{zyk} denotes the maximum number of periods. Potential φ_1 is prescribed for electrodes positioned at $X_{e1} \in \{0,\ 0.1m,\ 0.2m,\ 0.3m\}$. The temporal evolution of the potential φ_1 is depicted in Fig. 23 ($n_{zyk} = 5$). Potentials $\varphi_2 = 0$ are applied for electrodes positioned at $X_{e2} \in \{0.05m,\ 0.15m,\ 0.25m\}$. The fibre reinforcement is chosen along the longitudinal axis of the model in the reference configuration as $\boldsymbol{N}_0 = [0\ 0\ 1]^{\mathrm{T}}$. Mechanical Dirichlet boundary conditions are applied as follows

$$u_1(X_1 = 0) = 0,$$
$$u_2(X_2 = 0) = 0,$$
$$u_3(X_3 = 0.15) = 0.$$

As can be seen in Fig. 23 the potential oscillates periodically between the prescribed values at the electrodes. Typical snapshots of the motion together with the electrical potential distribution are shown in Fig. 24. The von Mises stress and the third component of $\boldsymbol{D}_0$ are shown for some time steps in Figs. 25 and 26, respectively. The energy evolution is given in Fig. 27. Again the midpoint rule becomes unstable until it finally fails at $2.8s$. In contrast to that the EM scheme consistently approximates the energy and is stable for the entire simulation time.

7.7. Dynamic wrinkling in a dielectric plate

The objectives of this example are:

O7.I Comparison of the robustness between the proposed EM time integrator and the midpoint rule time integrator in scenarios with more sophisticated electrically induced configurations which can represent a challenge from the robustness standpoint of the algorithm.
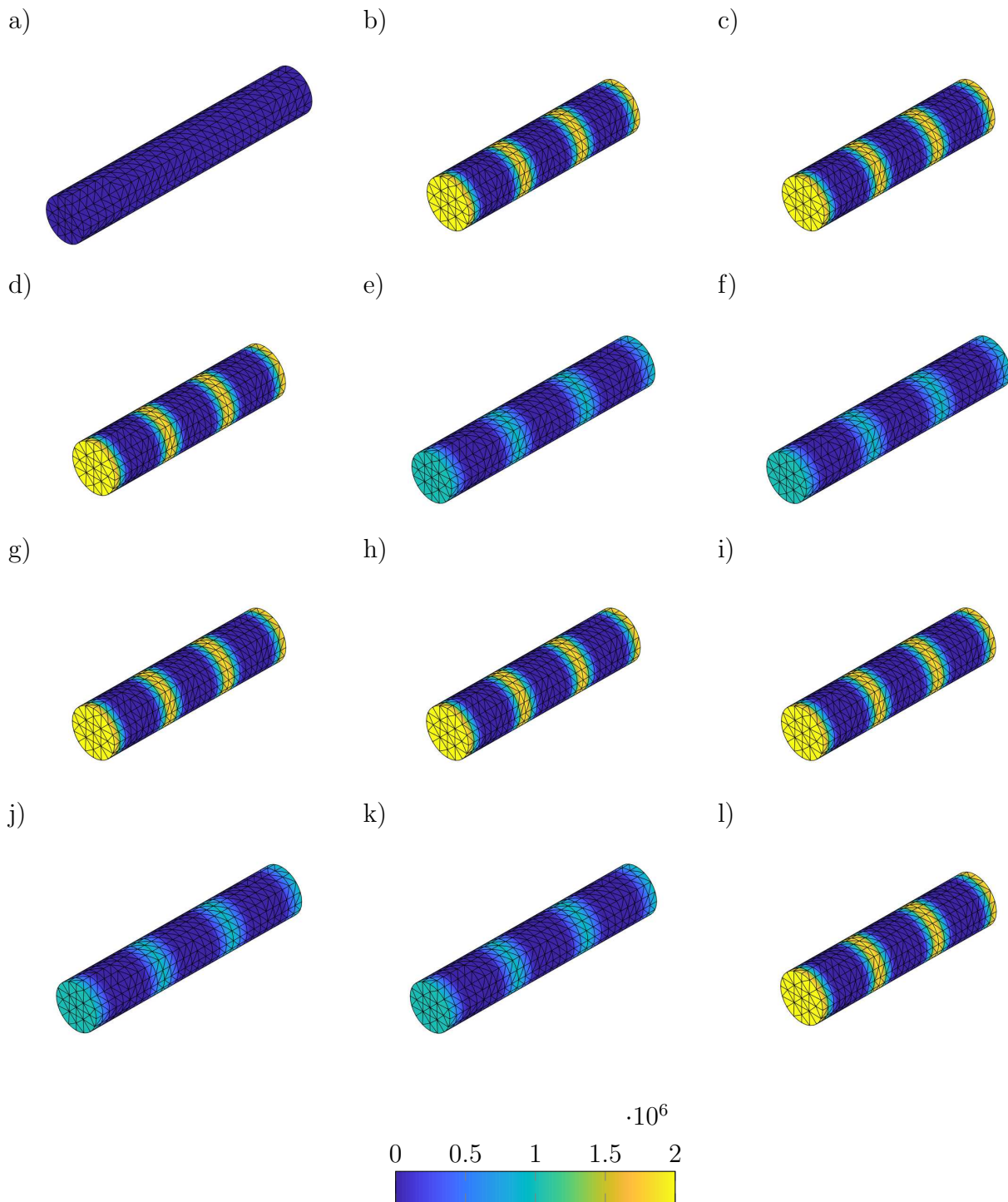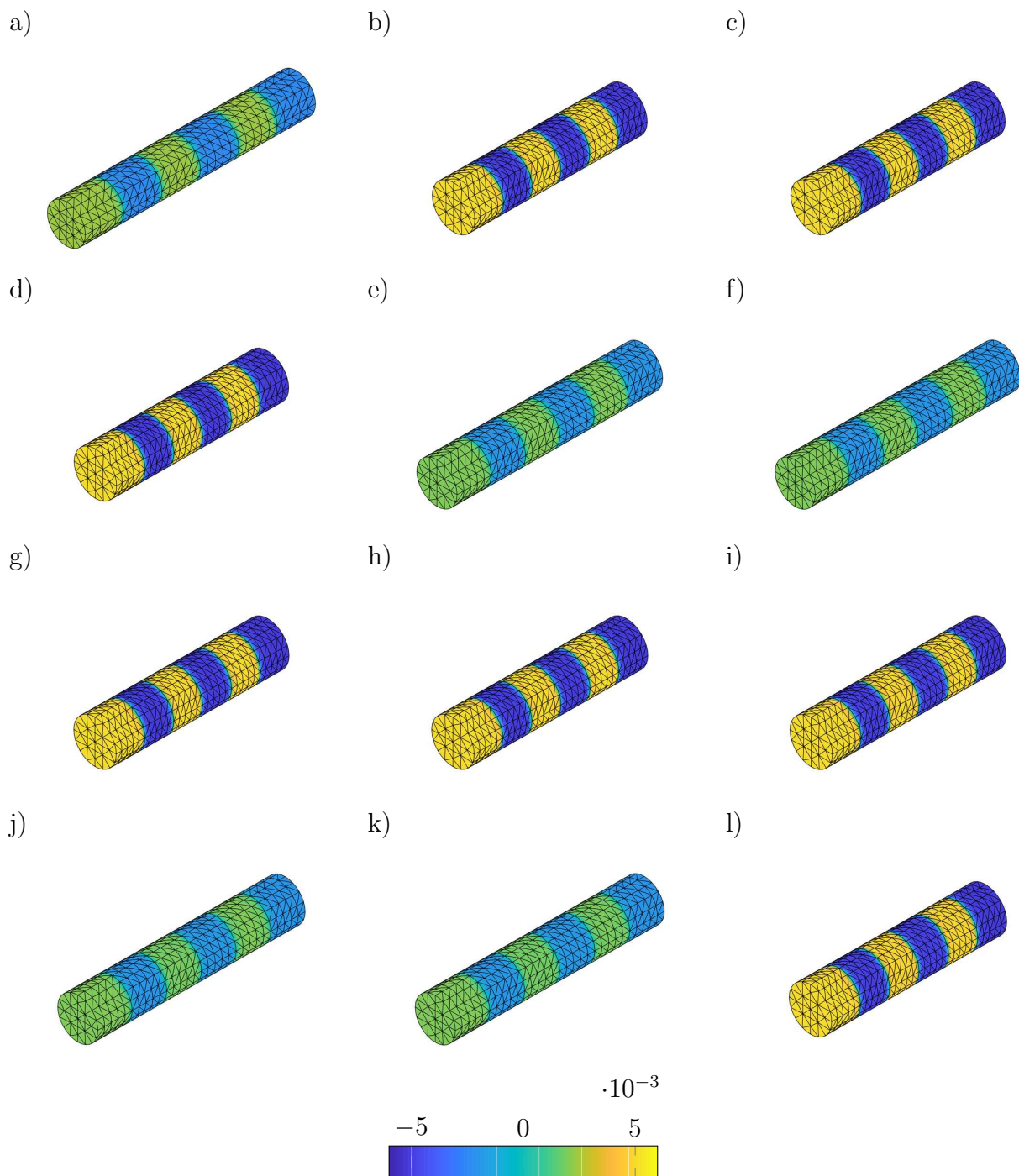
Figure 24: Artificial muscle model: Snapshots of electric potential φ for different configurations corresponding to (left to right-top to bottom): (a) $t = 0\,s$; (b) $t = 0.2\,s$; (c) $t = 0.4\,s$; (d) $t = 0.6\,s$; (e) $t = 0.8\,s$; (f) $t = 1.0\,s$; (g) $t = 1.2\,s$; (h) $t = 1.4\,s$; (i) $t = 1.6\,s$; (j) $t = 1.8\,s$; (k) $t = 2.0\,s$; (l) $t = 2.2\,s$.
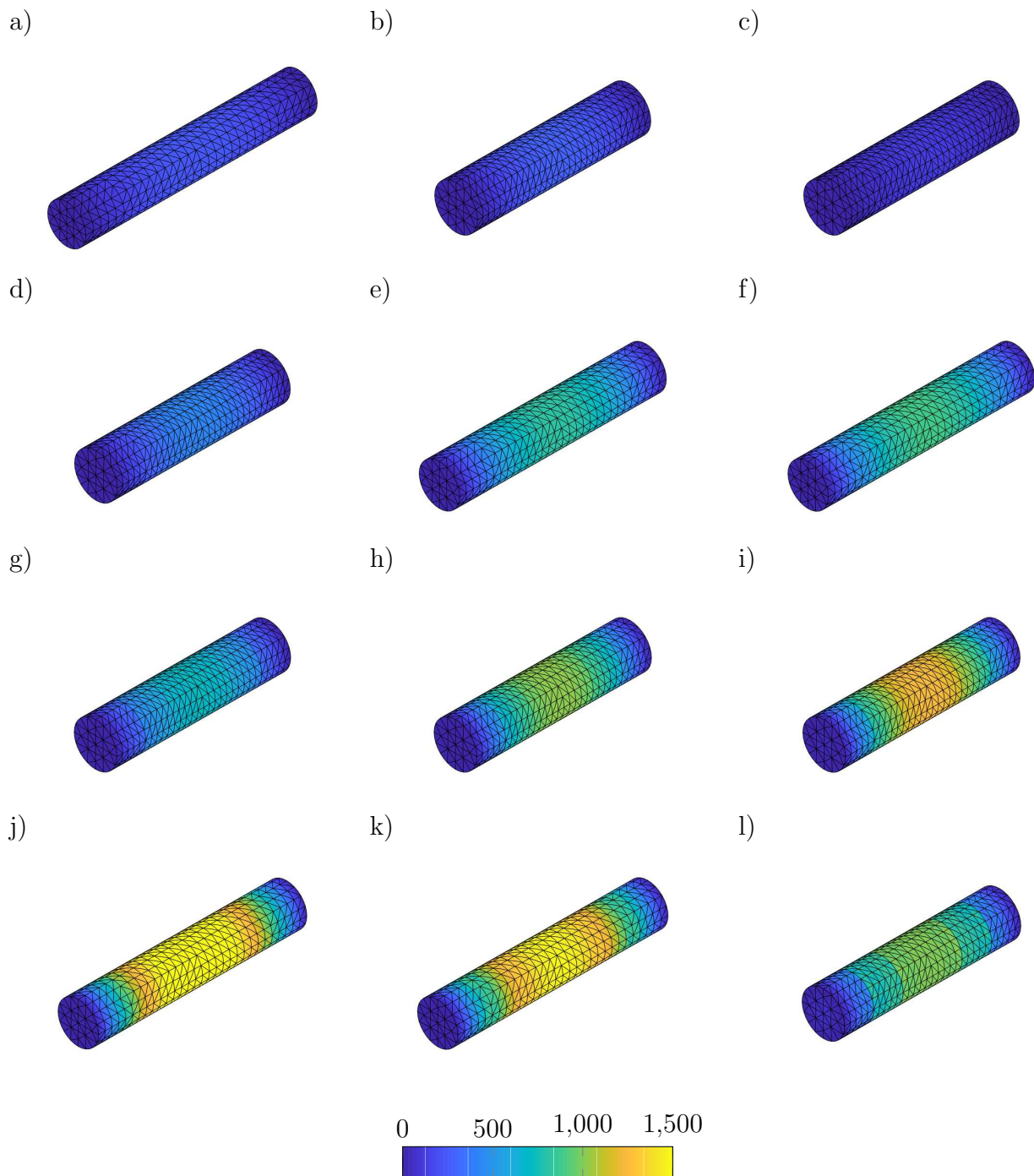
Figure 25: Artificial muscle model: Snapshots of von Mises stress σ_{vM} for different configurations corresponding to (left to right-top to bottom): (a) $t = 0\,s$; (b) $t = 0.2\,s$; (c) $t = 0.4\,s$; (d) $t = 0.6\,s$; (e) $t = 0.8\,s$; (f) $t = 1.0\,s$; (g) $t = 1.2\,s$; (h) $t = 1.4\,s$; (i) $t = 1.6\,s$; (j) $t = 1.8\,s$; (k) $t = 2.0\,s$; (l) $t = 2.2\,s$.

Figure 26: Artificial muscle model: Snapshots of third component of $\boldsymbol{D}_0$ for different configurations corresponding to (left to right-top to bottom): (a) $t = 0\,s$; (b) $t = 0.2\,s$; (c) $t = 0.4\,s$; (d) $t = 0.6\,s$; (e) $t = 0.8\,s$; (f) $t = 1.0\,s$; (g) $t = 1.2\,s$; (h) $t = 1.4\,s$; (i) $t = 1.6\,s$; (j) $t = 1.8\,s$; (k) $t = 2.0\,s$; (l) $t = 2.2\,s$.
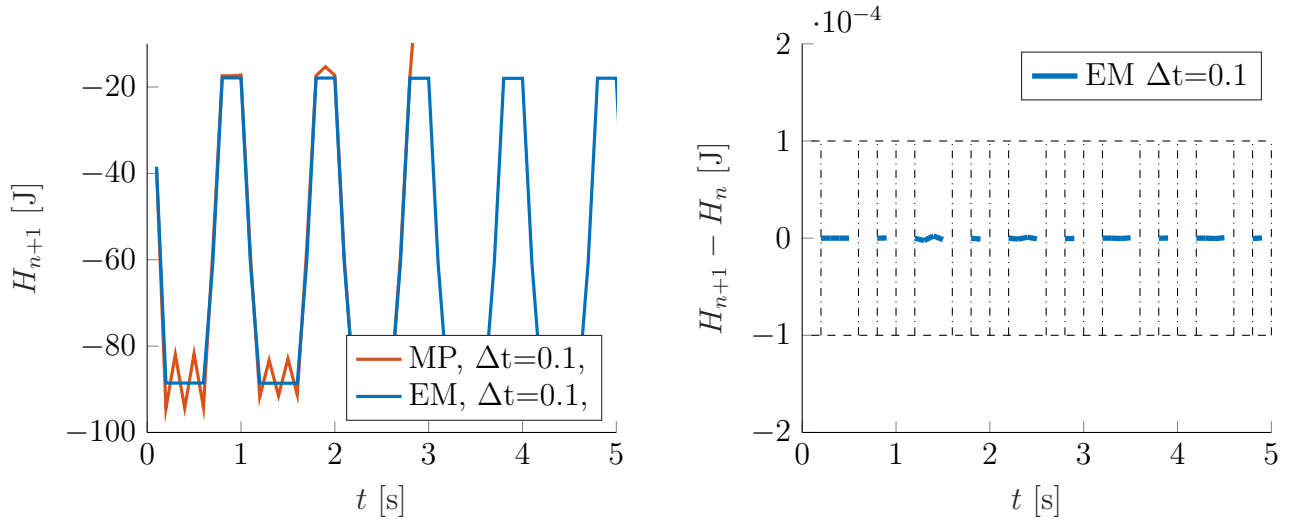
Figure 27: Artificial muscle model: Energy evolution for the proposed EM scheme. Left: Time evolution of $\mathcal{H}_{\widetilde{W}}$ with the proposed scheme. Right: Time evolution of $\Delta\mathcal{H}_{\widetilde{W}}$ in the time interval $[0.4, 3] \bigcup [3.4, 10]$.
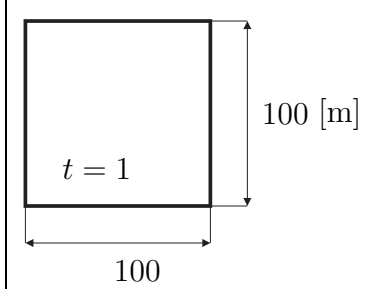
				Geometry of the body
Mechanical parameters	μ_1	2×10^5	Pa	
	μ_2	2×10^5	Pa	
	λ	2.5×10^5	Pa	
Electrical parameters	ϵ_0	8.854×10^{-12}	$A^2\,s^4\,kg^{-1}\,m^{-3}$	
	ϵ_r	4	N/V^2	
Ref. potential	φ_0	0	V	
Density	ρ_0	1	$kg\,m^{-3}$	
Timestep size	Δt	0.1	s	
Simulation time	T	3	s	
Newton tolerance	ϵ	10^{-4}	-	

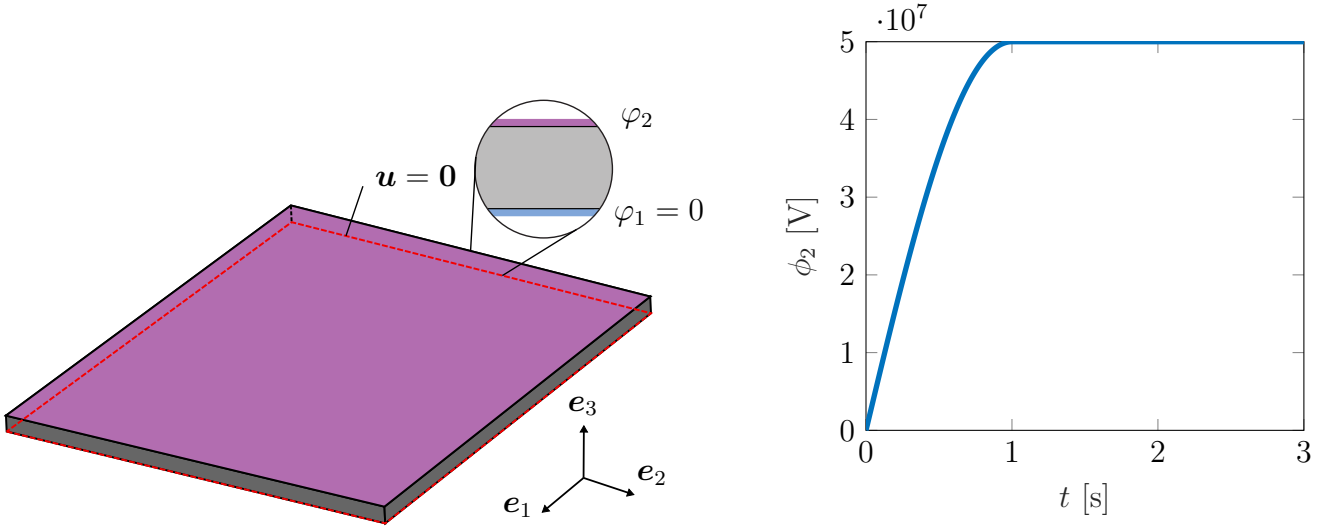Table 8: Dielectric plate: Material parameters, simulation parameters and geometry.

Figure 28: Dielectric plate: Mechanical boundary conditions (left) where $\boldsymbol{u}(X_1 = 0, X_2, X_3 = 0) = \boldsymbol{u}(X_1 = 100, X_2, X_3 = 0) = \boldsymbol{u}(X_1, X_2 = 0, X_3 = 0) = \boldsymbol{u}(X_1, X_2 = 100, X_3 = 0) = \boldsymbol{0}$ and applied electric potentials φ_1 and φ_2 (right) corresponding to (72).

The geometry, boundary conditions, material and simulation parameters of the dielectric plate are depicted in Tab. 8 and Fig. 28. Note that this example is inspired by the numerical example in [42, Sect. 4.6.4.]. A mesh comprised of 200 *tet 10/4* elements with a total of 5060 displacement and electrical potential unknowns (see Fig. 30) is employed. A constant value for the electric potential φ_1 is applied, whereas a time-varying value for φ_2 is applied according to (see Fig. 28)

$$\varphi_1 = 0 \ [V]; \quad \varphi_2 = \left(5 \times 10^7\right) \times \begin{cases} \sin(\frac{0.5\,\pi}{1\,\mathrm{s}}\,t) & \text{for } t \leq 1\,\mathrm{s} \\ 1 & \text{for } t > 1\,\mathrm{s} \end{cases} \ [V]. \tag{72}$$

Typical snapshots of the motion together with the electrical potential distribution are provided in Fig. 30. The von Mises stress and the third component of $\boldsymbol{D}_0$ are shown for some time steps in Figs. 31 and 32, respectively. Fig. 29 shows that the midpoint-rule time integrator exhibits an energy blow-up and becomes unstable approximately in the interval $1.1 < t < 1.3$. In contrast, the newly proposed EM time integrator conserves the total energy after the loading phase and remains stable for the whole simulation for the same fixed time step size of $\Delta t = 0.1\,s$.

8. Conclusions

This paper introduces a family of new mixed variational principles for EM time integrators in electro-elastodynamics. Building upon previous work in References [34] and [8], the following ingredients are shown to be key for the successful design of these EM schemes: (i) appropriate definition of the discrete derivatives of the strain energy, which coincide with those presented in [34]; (ii) use of the cascade system of kinematic constraints presented in [8] for the right Cauchy-Green deformation tensor, its co-factor and its Jacobian; (iii) consideration of piecewise interpolation of all the unknown fields except displacements and electric potential, making possible to carry out a standard static condensation procedure of the discontinuous fields; (iv) consideration of convex multi-variable constitutive models, hence guaranteeing material stability (or ellipticity) for the entire range of deformations and electric displacement fields.
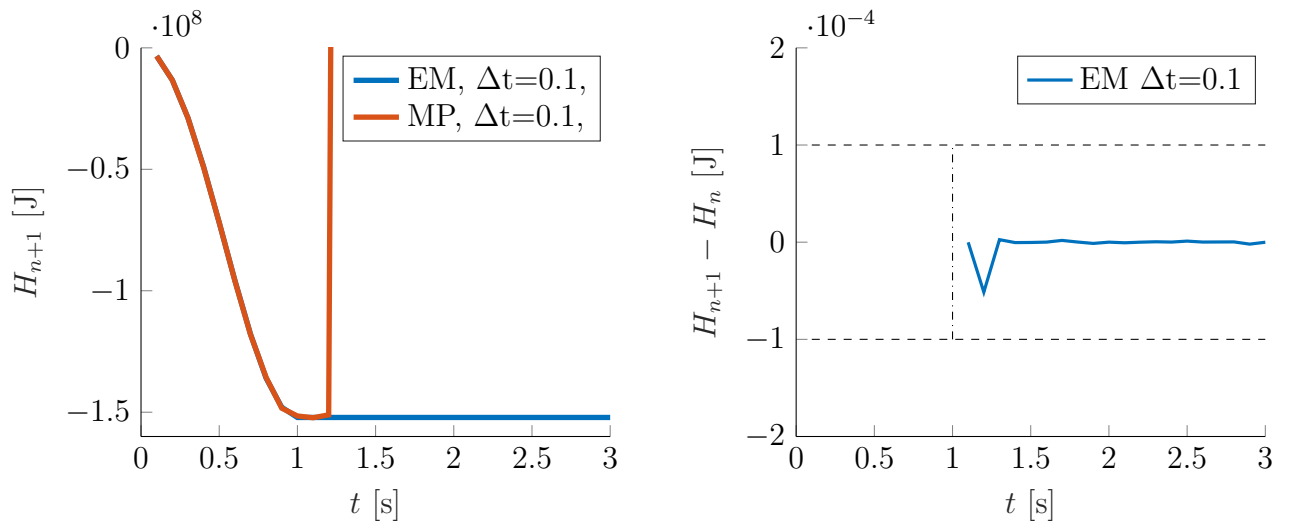
41

Figure 29: Dielectric plate: Energy evolution for the proposed EM scheme. Left: Time evolution of $\mathcal{H}_{\widetilde{W}}$ for proposed scheme. Right: Time evolution of $\Delta\mathcal{H}_{\widetilde{W}}$ in the time interval $[1,3]$.
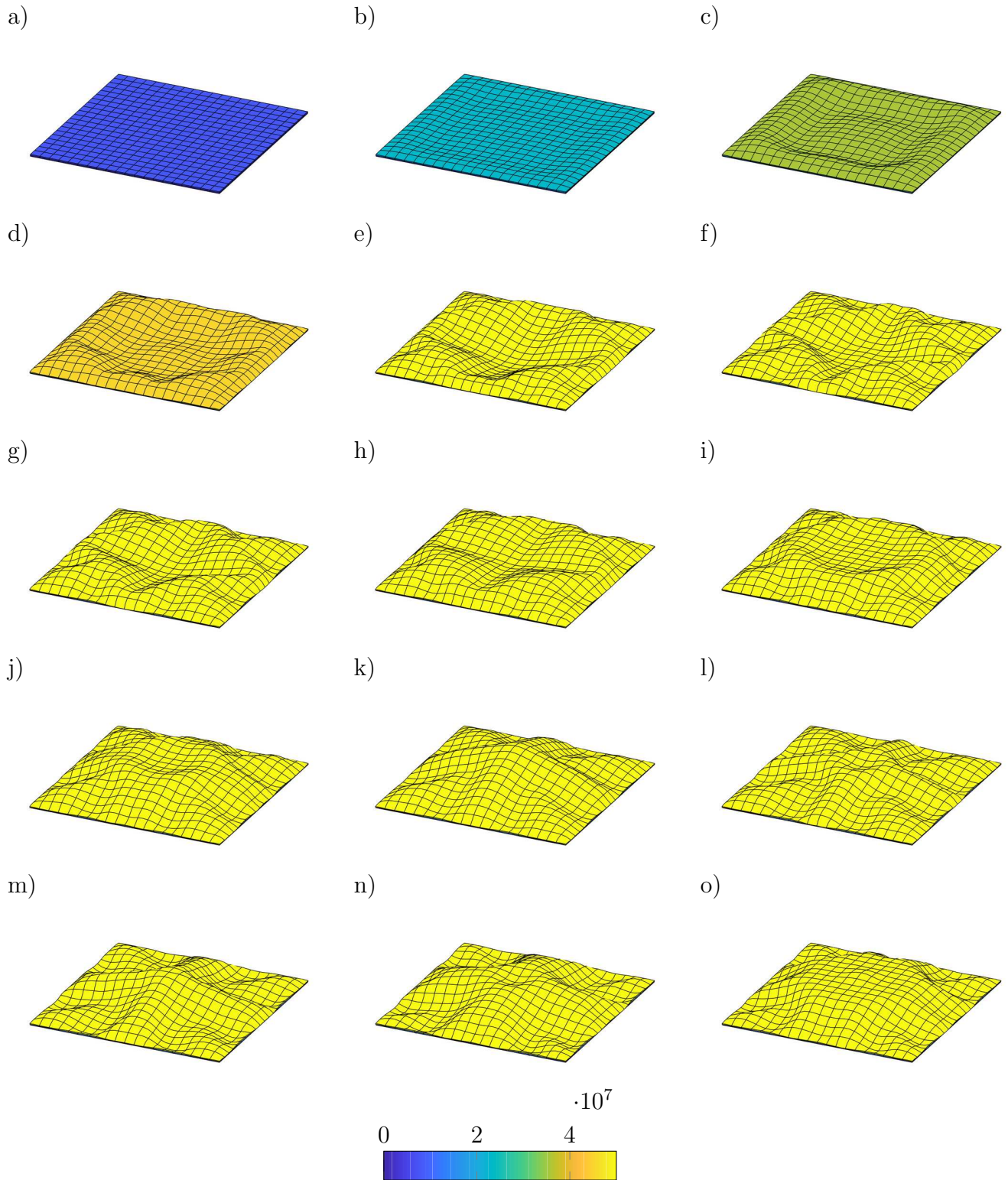
Figure 30: Dielectric plate: Snapshots of electric potential φ for different configurations corresponding to (left to right-top to bottom): (a) $t = 0.1\,s$; (b) $t = 0.3\,s$; (c) $t = 0.5\,s$; (d) $t = 0.7\,s$; (e) $t = 0.9\,s$; (f) $t = 1.1\,s$; (g) $t = 1.3\,s$; (h) $t = 1.5\,s$; (i) $t = 1.7\,s$; (j) $t = 1.9\,s$; (k) $t = 2.1\,s$; (l) $t = 2.3\,s$; (m) $t = 2.5\,s$; (n) $t = 2.7\,s$; (o) $t = 2.9\,s$.
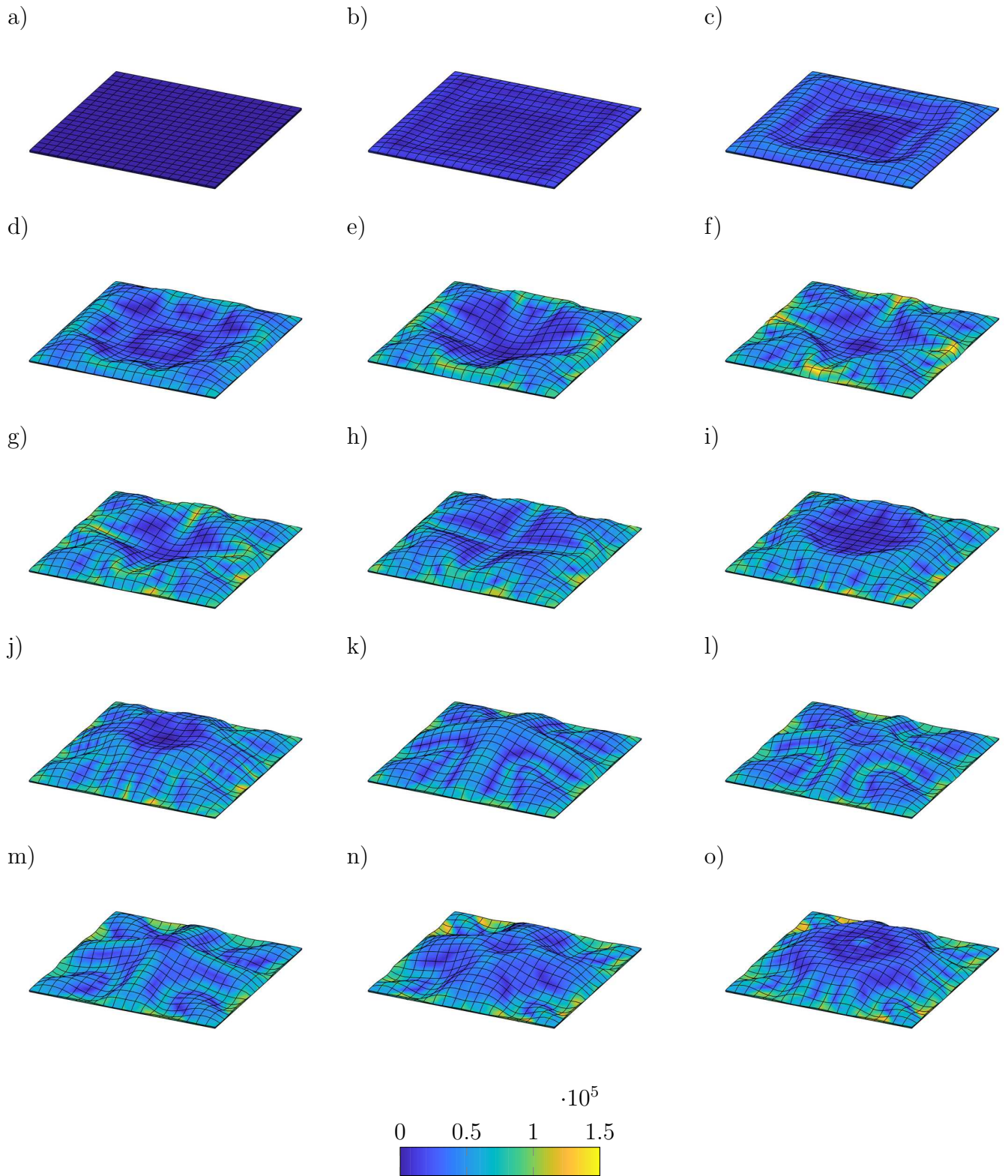
Figure 31: Dielectric plate: Snapshots of von Mises stress σ_{vM} for different configurations corresponding to (left to right-top to bottom): (a) $t = 0.1\,s$; (b) $t = 0.3\,s$; (c) $t = 0.5\,s$; (d) $t = 0.7\,s$; (e) $t = 0.9\,s$; (f) $t = 1.1\,s$; (g) $t = 1.3\,s$; (h) $t = 1.5\,s$; (i) $t = 1.7\,s$; (j) $t = 1.9\,s$; (k) $t = 2.1\,s$; (l) $t = 2.3\,s$; (m) $t = 2.5\,s$; (n) $t = 2.7\,s$; (o) $t = 2.9\,s$.
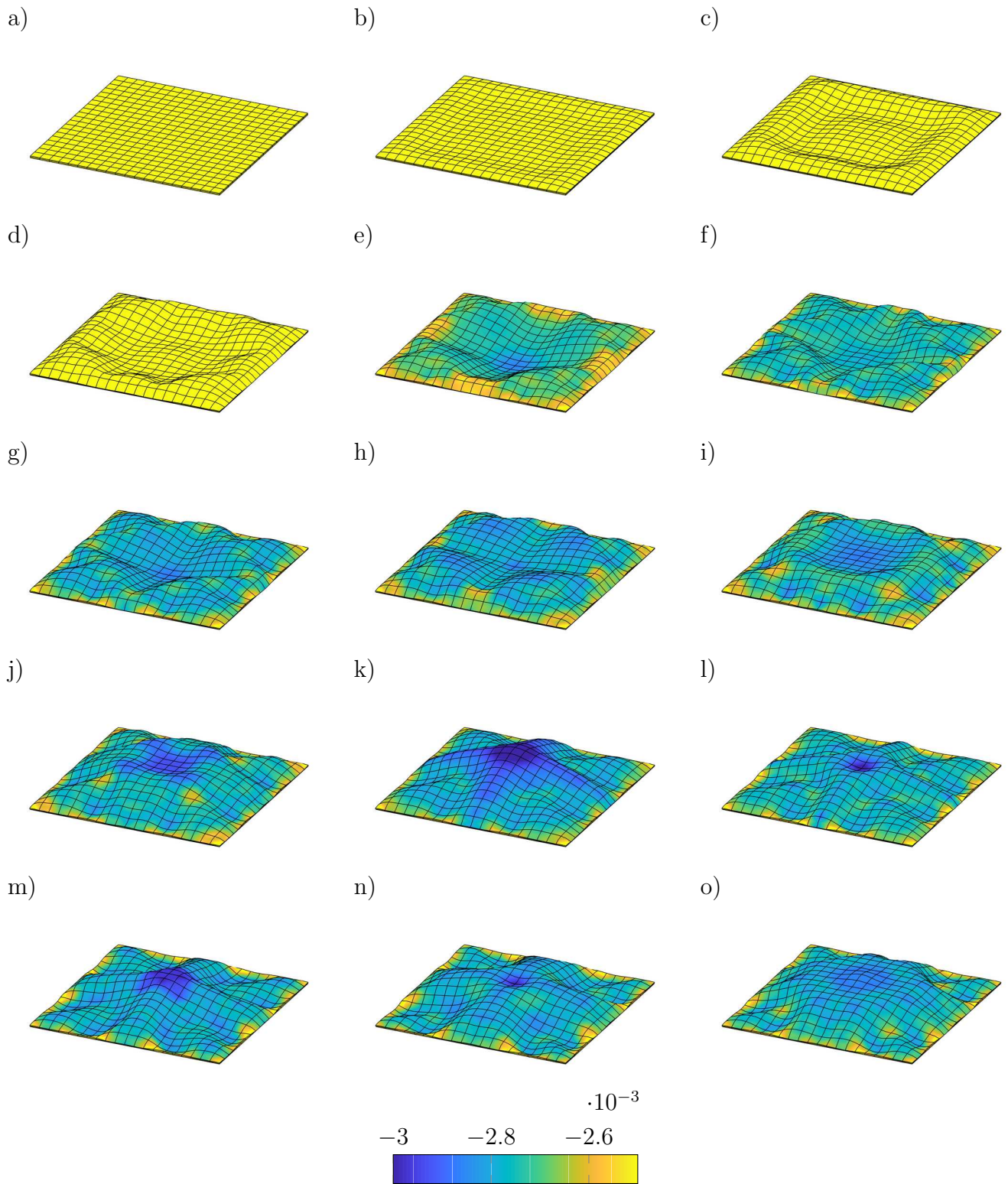
Figure 32: Dielectric plate: Snapshots of third component of $\boldsymbol{D}_0$ for different configurations corresponding to (left to right-top to bottom): (a) $t = 0.1\,s$; (b) $t = 0.3\,s$; (c) $t = 0.5\,s$; (d) $t = 0.7\,s$; (e) $t = 0.9\,s$; (f) $t = 1.1\,s$; (g) $t = 1.3\,s$; (h) $t = 1.5\,s$; (i) $t = 1.7\,s$; (j) $t = 1.9\,s$; (k) $t = 2.1\,s$; (l) $t = 2.3\,s$; (m) $t = 2.5\,s$; (n) $t = 2.7\,s$; (o) $t = 2.9\,s$.

Appendix A. Discrete derivatives of the internal energy

Appendix A.1. Definition of the discrete derivatives

The expressions for discrete derivatives $D_{\boldsymbol{C}}\widetilde{W}$, $D_{\boldsymbol{G}}\widetilde{W}$, $D_{\boldsymbol{G}}\widetilde{W}$, $D_{\boldsymbol{G}}\widetilde{W}$ in (32) and $D_{\boldsymbol{D}_0}\widetilde{W}$ in $(30)_d$ will be presented in this section. Although these expressions have been proposed in [34], we present them in this appendix for completeness. Let us introduce the following notation, $\{\mathcal{V}_1, \mathcal{V}_2, \mathcal{V}_3, \mathcal{V}_4\} = \{\boldsymbol{C}, \boldsymbol{G}, C, \boldsymbol{D}_0\}$. This will facilitate the definition of the discrete derivatives $D_{\widetilde{\mathcal{V}}_1}\widetilde{W} = D_{\boldsymbol{C}}\widetilde{W}$, $D_{\widetilde{\mathcal{V}}_2}\widetilde{W} = D_{\boldsymbol{G}}\widetilde{W}$ and $D_{\widetilde{\mathcal{V}}_3}\widetilde{W} = D_C\widetilde{W}$ and $D_{\widetilde{\mathcal{V}}_4}\widetilde{W} = D_{\boldsymbol{D}_0}\widetilde{W}$.

$$
\begin{aligned}
D_{\widetilde{\mathcal{V}}_i}\widetilde{W} &= \frac{1}{2}\left(D_{\widetilde{\mathcal{V}}_{i_{n+1,n}}}\widetilde{W} + D_{\widetilde{\mathcal{V}}_{i_{n,n+1}}}\widetilde{W} \right); && i \in Y = \{1,2,3,4\}; \\
D_{\widetilde{\mathcal{V}}_{i_{n+1,n}}}\widetilde{W} &= D_{\widetilde{\mathcal{V}}_i}\widetilde{W}\left(\widetilde{\mathcal{V}}_{i_{n+1}}, \widetilde{\mathcal{V}}_{i_n}\right)\Big|_{\widetilde{\mathcal{V}}_{j_{n+1}},\widetilde{\mathcal{V}}_{k_n}}; && \forall j \in Y : j < i; \ \forall k \in Y : k > i; \\
D_{\widetilde{\mathcal{V}}_{i_{n,n+1}}}\widetilde{W} &= D_{\widetilde{\mathcal{V}}_i}\widetilde{W}\left(\widetilde{\mathcal{V}}_{i_n}, \widetilde{\mathcal{V}}_{i_{n+1}}\right)\Big|_{\widetilde{\mathcal{V}}_{j_n},\widetilde{\mathcal{V}}_{k_{n+1}}}; && \forall j \in Y : j < i; \ \forall k \in Y : k > i,
\end{aligned} \tag{A.1}
$$

where the discrete operators $D_{\widetilde{\mathcal{V}}_i}\widetilde{W}\Big|_{\widetilde{\mathcal{V}}_{j_{n+1}},\widetilde{\mathcal{V}}_{k_n}}$ and $D_{\widetilde{\mathcal{V}}_i}\widetilde{W}\Big|_{\widetilde{\mathcal{V}}_{j_n},\widetilde{\mathcal{V}}_{k_{n+1}}}$ are defined as

$$
\begin{aligned}
D_{\widetilde{\mathcal{V}}_i}\widetilde{W}\Big|_{\widetilde{\mathcal{V}}_{j_{n+1}},\widetilde{\mathcal{V}}_{k_n}} &= \partial_{\widetilde{\mathcal{V}}_i}\widetilde{W}\left(\widetilde{\mathcal{V}}_{n+1/2}\right)\Big|_{\widetilde{\mathcal{V}}_{j_{n+1}},\widetilde{\mathcal{V}}_{k_n}} \\
&+ \frac{\widetilde{W}\left(\widetilde{\mathcal{V}}_{n+1}\right)\Big|_{\widetilde{\mathcal{V}}_{j_{n+1}},\widetilde{\mathcal{V}}_{k_n}} - \widetilde{W}\left(\widetilde{\mathcal{V}}_n\right)\Big|_{\widetilde{\mathcal{V}}_{j_{n+1}},\widetilde{\mathcal{V}}_{k_n}} - \partial_{\widetilde{\mathcal{V}}_i}\widetilde{W}\left(\widetilde{\mathcal{V}}_{n+1/2}\right)\Big|_{\widetilde{\mathcal{V}}_{j_{n+1}},\widetilde{\mathcal{V}}_{k_n}} : \Delta\widetilde{\mathcal{V}}_i}{\|\Delta\widetilde{\mathcal{V}}_i\|^2}\Delta\widetilde{\mathcal{V}}_i; \\
D_{\widetilde{\mathcal{V}}_i}\widetilde{W}\Big|_{\widetilde{\mathcal{V}}_{j_n},\widetilde{\mathcal{V}}_{k_{n+1}}} &= \partial_{\widetilde{\mathcal{V}}_i}\widetilde{W}\left(\widetilde{\mathcal{V}}_{n+1/2}\right)\Big|_{\widetilde{\mathcal{V}}_{j_n},\widetilde{\mathcal{V}}_{k_{n+1}}} \\
&+ \frac{\widetilde{W}\left(\widetilde{\mathcal{V}}_{n+1}\right)\Big|_{\widetilde{\mathcal{V}}_{j_n},\widetilde{\mathcal{V}}_{k_{n+1}}} - \widetilde{W}\left(\widetilde{\mathcal{V}}_n\right)\Big|_{\widetilde{\mathcal{V}}_{j_n},\widetilde{\mathcal{V}}_{k_{n+1}}} - \partial_{\widetilde{\mathcal{V}}_i}\widetilde{W}\left(\widetilde{\mathcal{V}}_{n+1/2}\right)\Big|_{\widetilde{\mathcal{V}}_{j_n},\widetilde{\mathcal{V}}_{k_{n+1}}} : \Delta\widetilde{\mathcal{V}}_i}{\|\Delta\widetilde{\mathcal{V}}_i\|^2}\Delta\widetilde{\mathcal{V}}_i.
\end{aligned} \tag{A.2}
$$

From above equations (A.1) and (A.2), the directional derivative $D_{\boldsymbol{C}}\widetilde{W}$ can be computed as

$$
\begin{aligned}
D_{\boldsymbol{C}}\widetilde{W} &= \frac{1}{2}\left(\partial_{\boldsymbol{C}}\widetilde{W}\left(\boldsymbol{C}_{n+1/2}, \boldsymbol{G}_{n+1}, C_{n+1}, \boldsymbol{D}_{0_{n+1}}\right) + \partial_{\boldsymbol{C}}\widetilde{W}\left(\boldsymbol{C}_{n+1/2}, \boldsymbol{G}_n, C_n, \boldsymbol{D}_{0_n}\right) \right) \\
&+ \frac{1}{2}\frac{\widetilde{W}\left(\boldsymbol{C}_{n+1}, \boldsymbol{G}_{n+1}, C_{n+1}, \boldsymbol{D}_{0_{n+1}}\right) - \widetilde{W}\left(\boldsymbol{C}_n, \boldsymbol{G}_{n+1}, C_{n+1}, \boldsymbol{D}_{0_{n+1}}\right)}{\|\Delta\boldsymbol{C}\|^2}\Delta\boldsymbol{C} \\
&+ \frac{1}{2}\frac{\widetilde{W}\left(\boldsymbol{C}_{n+1}, \boldsymbol{G}_n, C_n, \boldsymbol{D}_{0_n}\right) - \widetilde{W}\left(\boldsymbol{C}_n, \boldsymbol{G}_n, C_n, \boldsymbol{D}_{0_n}\right)}{\|\Delta\boldsymbol{C}\|^2}\Delta\boldsymbol{C} \\
&- \frac{1}{2}\frac{\partial_{\boldsymbol{C}}\widetilde{W}\left(\boldsymbol{C}_{n+1/2}, \boldsymbol{G}_{n+1}, C_{n+1}, \boldsymbol{D}_{0_{n+1}}\right) : \Delta\boldsymbol{C}}{\|\Delta\boldsymbol{C}\|^2}\Delta\boldsymbol{C} \\
&- \frac{1}{2}\frac{\partial_{\boldsymbol{C}}\widetilde{W}\left(\boldsymbol{C}_{n+1/2}, \boldsymbol{G}_n, C_n, \boldsymbol{D}_{0_n}\right) : \Delta\boldsymbol{C}}{\|\Delta\boldsymbol{C}\|^2}\Delta\boldsymbol{C}.
\end{aligned} \tag{A.3}
$$

Similarly, the directional derivative $D_{\boldsymbol{G}}\widetilde{W}$ can be computed as

$$
\begin{aligned}
D_{\boldsymbol{G}}\widetilde{W} = {} & \frac{1}{2}\left(\partial_{\boldsymbol{G}}\widetilde{W}\left(\boldsymbol{C}_n, \boldsymbol{G}_{n+1/2}, C_{n+1}, \boldsymbol{D}_{0_{n+1}}\right) + \partial_{\boldsymbol{G}}\widetilde{W}\left(\boldsymbol{C}_{n+1}, \boldsymbol{G}_{n+1/2}, C_n, \boldsymbol{D}_{0_n}\right)\right) \\
& + \frac{1}{2}\frac{\widetilde{W}\left(\boldsymbol{C}_n, \boldsymbol{G}_{n+1}, C_{n+1}, \boldsymbol{D}_{0_{n+1}}\right) - \widetilde{W}\left(\boldsymbol{C}_n, \boldsymbol{G}_n, C_{n+1}, \boldsymbol{D}_{0_{n+1}}\right)}{||\Delta\boldsymbol{G}||^2}\Delta\boldsymbol{G} \\
& + \frac{1}{2}\frac{\widetilde{W}\left(\boldsymbol{C}_{n+1}, \boldsymbol{G}_{n+1}, C_n, \boldsymbol{D}_{0_n}\right) - \widetilde{W}\left(\boldsymbol{C}_{n+1}, \boldsymbol{G}_n, C_n, \boldsymbol{D}_{0_n}\right)}{||\Delta\boldsymbol{G}||^2}\Delta\boldsymbol{G} \\
& - \frac{1}{2}\frac{\partial_{\boldsymbol{G}}\widetilde{W}\left(\boldsymbol{C}_n, \boldsymbol{G}_{n+1/2}, C_{n+1}, \boldsymbol{D}_{0_{n+1}}\right) : \Delta\boldsymbol{G}}{||\Delta\boldsymbol{G}||^2}\Delta\boldsymbol{G} \\
& - \frac{1}{2}\frac{\partial_{\boldsymbol{G}}\widetilde{W}\left(\boldsymbol{C}_{n+1}, \boldsymbol{G}_{n+1/2}, C_n, \boldsymbol{D}_{0_n}\right) : \Delta\boldsymbol{G}}{||\Delta\boldsymbol{G}||^2}\Delta\boldsymbol{G}.
\end{aligned}
\tag{A.4}
$$

Furthermore, the directional derivative $D_C\widetilde{W}$ can be computed as

$$
\begin{aligned}
D_C\widetilde{W} = {} & \frac{1}{2}\frac{\widetilde{W}\left(\boldsymbol{C}_n, \boldsymbol{G}_n, C_{n+1}, \boldsymbol{D}_{0_{n+1}}\right) - \widetilde{W}\left(\boldsymbol{C}_n, \boldsymbol{G}_n, C_n, \boldsymbol{D}_{0_{n+1}}\right)}{||\Delta C||} \\
& + \frac{1}{2}\frac{\widetilde{W}\left(\boldsymbol{C}_{n+1}, \boldsymbol{G}_{n+1}, C_{n+1}, \boldsymbol{D}_{0_n}\right) - \widetilde{W}\left(\boldsymbol{C}_{n+1}, \boldsymbol{G}_{n+1}, C_n, \boldsymbol{D}_{0_n}\right)}{||\Delta C||}.
\end{aligned}
\tag{A.5}
$$

Finally, the directional derivative $D_{\boldsymbol{D}_0}\widetilde{W}$ can be computed as

$$
\begin{aligned}
D_{\boldsymbol{D}_0}\widetilde{W} = {} & \frac{1}{2}\left(\partial_{\boldsymbol{D}_0}\widetilde{W}\left(\boldsymbol{C}_n, \boldsymbol{G}_n, C_n, \boldsymbol{D}_{0_{n+1/2}}\right) + \partial_{\boldsymbol{D}_0}\widetilde{W}\left(\boldsymbol{C}_{n+1}, \boldsymbol{G}_{n+1}, C_{n+1}, \boldsymbol{D}_{0_{n+1/2}}\right)\right) \\
& \frac{1}{2}\frac{\widetilde{W}\left(\boldsymbol{C}_n, \boldsymbol{G}_n, C_n, \boldsymbol{D}_{0_{n+1}}\right) - \widetilde{W}\left(\boldsymbol{C}_n, \boldsymbol{G}_n, C_n, \boldsymbol{D}_{0_n}\right)}{||\Delta\boldsymbol{D}_0||^2}\Delta\boldsymbol{D}_0 \\
& + \frac{1}{2}\frac{\widetilde{W}\left(\boldsymbol{C}_{n+1}, \boldsymbol{G}_{n+1}, C_{n+1}, \boldsymbol{D}_{0_{n+1}}\right) - \widetilde{W}\left(\boldsymbol{C}_{n+1}, \boldsymbol{G}_{n+1}, C_{n+1}, \boldsymbol{D}_{0_n}\right)}{||\Delta\boldsymbol{D}_0||^2}\Delta\boldsymbol{D}_0 \\
& - \frac{1}{2}\frac{\partial_{\boldsymbol{D}_0}\widetilde{W}\left(\boldsymbol{C}_n, \boldsymbol{G}_n, C_n, \boldsymbol{D}_{0_{n+1/2}}\right) \cdot \Delta\boldsymbol{D}_0}{||\Delta\boldsymbol{D}_0||^2}\Delta\boldsymbol{D}_0 \\
& - \frac{1}{2}\frac{\partial_{\boldsymbol{D}_0}\widetilde{W}\left(\boldsymbol{C}_{n+1}, \boldsymbol{G}_{n+1}, C_{n+1}, \boldsymbol{D}_{0_{n+1/2}}\right) \cdot \Delta\boldsymbol{D}_0}{||\Delta\boldsymbol{D}_0||^2}\Delta\boldsymbol{D}_0.
\end{aligned}
\tag{A.6}
$$

[1] J. M. Ball. Energy-minimising configurations in nonlinear elasticity. *Archive for Rational Mechanics and Analysis*, 63(4):337–403, 1976.

[2] J. M. Ball. Some open problems in elasticity. In *Geometry, mechanics, and dynamics*, pages 3–59. Springer, 2002.

[3] J.M. Ball. Convexity conditions and existence theorems in nonlinear elasticity. *Archive for Rational Mechanics and Analysis*, 63(4):337–403, 1976.

[4] K. J. Bathe. *Finite Element Procedures*. Prentice Hall, 1996.

[5] K. Bertoldi and M. Gei. Instabilities in multilayered soft dielectrics. *Journal of the Mechanics and Physics of Solids*, 59(1):18–42, 2011.

[6] P. Betsch, editor. *Structure-preserving Integrators in Nonlinear Structural Dynamics and Flexible Multibody Dynamics*, volume 565 of *CISM Courses and Lectures*. Springer-Verlag, 2016.

[7] P. Betsch and A. Janz. An energy-momentum consistent method for transient simulations with mixed finite elements developed in the framework of geometrically exact shells. *Int. J. Numer. Meth. Engng*, 108(5):423–455, 2016.

[8] P. Betsch, A. Janz, and C. Hesch. A mixed variational framework for the design of energy–momentum schemes inspired by the structure of polyconvex stored energy functions. *Computer Methods in Applied Mechanics and Engineering*, 335:660–696, 2018.

[9] J. Bonet, A. J. Gil, and R. Ortigosa. A computational framework for polyconvex large strain elasticity. *Computer Methods in Applied Mechanics and Engineering*, 283:1061–1094, 2015.

[10] J. Bonet, A. J. Gil, and R. Ortigosa. On a tensor cross product based formulation of large strain solid mechanics. *International Journal of Solids and Structures*, 84:49–63, 2016.

[11] J. Bonet, A. J. Gil, and R. D. Wood. *Nonlinear Continuum Mechanics for Finite Element Analysis: Statics*. Cambridge University Press, 2016.

[12] S. Chiba, M. Waki, T. Wada, Y. Hirakawa, K. Masuda, and T. Ikoma. Consistent ocean wave energy harvesting using electroactive polymer (dielectric elastomer) artificial muscle generators. *Applied Energy*, 104(0):497–502, 2013.

[13] R. de Boer. *Vektor- und Tensorrechnung für Ingenieure*. Springer-Verlag, 1982.

[14] E.A. de Souza Neto, D. Períc, and D.R.J. Owen. *Computational Methods for Plasticity. Theory and Applications*. Johnn Wiley and Sons Ltd, 2008.

[15] A. Dorfmann and R. W. Ogden. Nonlinear electroelasticity. *Acta Mechanica*, 174(3-4):167–183, 2005.

[16] A. Dorfmann and R.W. Ogden. Nonlinear electroelastic deformations. *Journal of Elasticity*, 82(2):99–127, 2006.

[17] Luis Dorfmann and Ray W Ogden. *Nonlinear theory of electroelastic and magnetoelastic interactions*. Springer, 2014.

[18] M. Franke, A. Janz, M. Schiebl, and P. Betsch. An energy momentum consistent integration scheme using a polyconvexity-based framework for nonlinear thermo-elastodynamics. *International Journal for Numerical Methods in Engineering*, 115(5):549–577, 2018.

[19] A. J. Gil and R. Ortigosa. A new framework for large strain electromechanics based on convex multi-variable strain energies: variational formulation and material characterisation. *Computer Methods in Applied Mechanics and Engineering*, 302:293–328, 2016.

[20] O. Gonzalez. Exact energy and momentum conserving algorithms for general models in nonlinear elasticity. *Comput. Methods Appl. Mech. Engrg.*, 190:1763–1783, 2000.

[21] O. Gonzalez and A. M. Stuart. *A first course in Continuum Mechanics*. Cambridge University Press, 2008.

[22] M. Groß and P. Betsch. Energy-momentum consistent finite element discretization of dynamic finite viscoelasticity. *Int. J. Numer. Meth. Engng*, 81(11):1341–1386, 2010.

[23] M. Gross, P. Betsch, and P. Steinmann. Conservation properties of a time FE method. Part IV: Higher order energy and momentum conserving schemes. *Int. J. Numer. Methods Eng.*, 63:1849–1897, 2005.

[24] M. Groß and J. Dietzsch. Variational-based energy-momentum schemes of higher-order for elastic fiber-reinforced continua. *Comput. Methods Appl. Mech. Engrg.*, 283:1061–1094, 2015.

[25] C. Hesch and P. Betsch. Energy-momentum consistent algorithms for dynamic thermomechanical problems – application to mortar domain decomposition problems. *Int. J. Numer. Meth. Engng*, 86(11):1277–1302, 2011.

[26] Mahmood Jabareen. On the modeling of electromechanical coupling in electroactive polymers using the mixed finite element formulation. *Procedia IUTAM*, 12:105–115, 2015.

[27] G. Kofod, P. Sommer-Larsen, R. Kornbluh, and R. Pelrine. Actuation response of polyacrylate dielectric elastomers. *Journal of Intelligent Material Systems and Structures*, 14(12):787–793, 2003.

[28] T. Li, C. Keplinger, R. Baumgartner, S. Bauer, W. Yang, and Z. Suo. Giant voltage-induced deformation in dielectric elastomers near the verge of snap-through instability. *Journal of the Mechanics and Physics of Solids*, 61(2):611–628, 2013.

[29] R.H. MacNeal and R.L. Harder. A proposed standard set of problems to test finite element accuracy. *Finite Elements in Analysis and Design*, 1:3–20, 1985.

[30] Jerrold E Marsden and Thomas JR Hughes. *Mathematical foundations of elasticity*. Courier Corporation, 1994.

[31] R. M. McMeeking and C. M. Landis. Electrostatic forces and stored energy for deformable dielectric materials. *Journal of Applied Mechanics*, 72(4):581–590, 2008.

[32] C Miehe, D Vallicotti, and D Zäh. Computational structural and material stability analysis in finite electro-elasto-statics of electro-active materials. *International Journal for Numerical Methods in Engineering*, 102(10):1605–1637, 2015.

[33] A. O'Halloran, F. O'Malley, and P. McHugh. A review on dielectric elastomer actuators, technology, applications, and challenges. *Journal of Applied Physics*, 104(7), 2008.

[34] R. Ortigosa, M. Franke, A. Janz, A.J. Gil, and P. Betsch. An energy-momentum time integration scheme based on a convex multi-variable framework for non-linear electro-elastodynamics. *Computer Methods in Applied Mechanics and Engineering*, 339:1–35, 2018.

[35] R. Ortigosa and A. J. Gil. A new framework for large strain electromechanics based on convex multi-variable strain energies: Conservation laws, hyperbolicity and extension to electro-magneto-mechanics. *Computer Methods in Applied Mechanics and Engineering*, 309:202–242, 2016.

[36] R. Ortigosa and A. J. Gil. A new framework for large strain electromechanics based on convex multi-variable strain energies: Finite element discretisation and computational implementation. *Computer Methods in Applied Mechanics and Engineering*, 302:329–360, 2016.

[37] R. Ortigosa and A. J. Gil. A computational framework for incompressible electromechanics based on convex multi-variable strain energies for geometrically exact shell theory. *Computer Methods in Applied Mechanics and Engineering*, 317:792–816, 2017.

[38] R. Ortigosa, A. J. Gil, and C. H. Lee. A computational framework for large strain nearly and truly incompressible electromecahnics based on convex multi-variable strain energies. *Computer Methods in Applied Mechanics and Engineering*, 310:297–334, 2016.

[39] R. Pelrine, R. Kornbluh, Q. Pei, and J. Joseph. High-speed electrically actuated elastomers with strain greater than 100 %. *Science*, 287(5454):836–839, 2000.

[40] R. Pelrine, R.D. Kornbluh, Q. Pei, S. Stanford, S. Oh, J. Eckerle, R.J̃. Full, M.A. Rosenthal, and K. Meijer. Dielectric elastomer artificial muscle actuators: toward biomimetic motion. *Proc. SPIE*, 4695:126–137, 2002.

[41] R. E. Pelrine, R. D. Kornbluh, and J. P. Joseph. Electrostriction of polymer dielectrics with compliant electrodes as a means of actuation. *Sensors and Actuators A: Physical*, 64(1):77–85, 1998.

[42] R. Poya, A. J. Gil, R. Ortigosa, R. Sevilla, J. Bonet, and W. A. Wall. A curvilinear high order finite element framework for electromechanics: From linearised electro-elasticity to massively deformable dielectric elastomers. *Computer Methods in Applied Mechanics and Engineering*, 329:75–117, 2018.

[43] I. Romero. An analysis of the stress formula for energy-momentum methods in nonlinear elastodynamics. *Computational Mechanics*, 50(5):603–610, Nov 2012.

[44] Tristan Schlögl and S Leyendecker. Electrostatic-viscoelastic finite element model of dielectric actuators. *Computer Methods in Applied Mechanics and Engineering*, 299:421–439, 02 2016.

[45] J. Schröder, P. Wriggers, and D. Balzani. A new mixed finite element based on different approximations of the minors of deformation tensors. *Computer Methods in Applied Mechanics and Engineering*, 200(49-52):3583–3600, 2011.

[46] M. H. Siboni, R. Avazmohammadi, and P. P. Castañeda. Electromechanical instabilities in fiber-constrained, dielectric-elastomer composites subjected to all-around dead-loading. *Mathematics and Mechanics of Solids*, 2014.

[47] M. H. Siboni and P. P. Castañeda. Fiber-constrained, dielectric-elastomer composites: Finite-strain response and stability analysis. *Journal of the Mechanics and Physics of Solids*, 68(0):211–238, 2014.

[48] J. C. Simo and N. Tarnow. The discrete energy-momentum method. conserving algorithms for nonlinear elastodynamics. *Zeitschrift für angewandte Mathematik und Physik ZAMP*, 43(5):757–792, 1992.

[49] S. Skatulla, C. Sansour, and A. Arockiarajan. A multiplicative approach for nonlinear electro-elasticity. *Computer Methods in Applied Mechanics and Engineering*, 245-246(0):243–255, 2012.

[50] Z. Suo, X. Zhao, and W. H. Greene. A nonlinear field theory of deformable dielectrics. *Journal of the Mechanics and Physics of Solids*, 56(2):467–486, 2008.

[51] F. Vogel, R. Bustamante, and P. Steinmann. On some mixed variational principles in electro-elastostatics. *International Journal of Non-Linear Mechanics*, 47(2):341–354, 2012.

[52] D. K. Vu and P. Steinmann. A 2-D coupled BEM-FEM simulation of electro-elastostatics at large strain. *Computer Methods in Applied Mechanics and Engineering*, 199(17-20):1124–1133, 2010.

[53] D. K. Vu and P. Steinmann. On 3-D coupled BEM-FEM simulation of nonlinear electro-elastostatics. *Computer Methods in Applied Mechanics and Engineering*, 201-204(0):82–90, 2012.